Control of mixing and oscillations in plasmas and fluids

Lauret, M.

DOI:
10.6100/IR777890

Published: 01/01/2014

Document Version
Publisher's PDF, also known as Version of Record (includes final page, issue and volume numbers)

Control of Mixing and Oscillations in Plasmas and Fluids

This research, supported by FOM programme 120 and the European Communities under the contract of the Association EURATOM/FOM, was carried out within the framework of the European Fusion Programme. The work was carried out at the Control Systems Technology group at the Mechanical Engineering department of the Eindhoven University of Technology in collaboration with the Centre de Recherches en Physique des Plasmas, part of the École Polytechnique Fédérale de Lausanne. The views and opinions expressed herein do not necessarily reflect those of the European Commission.

Control of Mixing and Oscillations in Plasmas and Fluids
by Menno Lauret
Technische Universiteit Eindhoven, 2014 - Proefschrift

A catalogue record is available from the Eindhoven University of Technology Library
ISBN: 978-90-386-3675-7

Typeset by the author using LaTeX 2_ε
Cover design: Nick Bauer
Reproduction: Ipskamp Drukkers B.V., Enschede, The Netherlands

Control of Mixing and Oscillations in Plasmas and Fluids

PROEFSCHRIFT

ter verkrijging van de graad van doctor
aan de Technische Universiteit Eindhoven,
op gezag van de rector magnificus prof.dr.ir. C.J. van Duijn,
voor een commissie aangewezen door het College voor Promoties,
in het openbaar te verdedigen
op maandag 22 september 2014 om 16.00 uur

door

Menno Lauret

geboren te Hulst

Dit proefschrift is goedgekeurd door de promotoren en de samenstelling van de promotiecommissie is als volgt:

voorzitter:	prof.dr. L.P.H. de Goey
1e promotor:	prof.dr. M.R. de Baar
2e promotor:	prof.dr.ir. W.P.M.H. Heemels
leden:	prof.dr. R. Keppens (Katholieke Universiteit Leuven)
	prof.dr. I. Mezić (University of California, Santa Barbara)
	prof.dr.ir. G.J.F. van Heijst
	dr. E. Witrant (University Joseph Fourier, Grenoble)
	prof.dr. H. Nijmeijer

Contents

Chapter 1

Introduction

Abstract

This thesis is concerned with three specific problems in fluid and plasma dynamics: Stabilization of patterns in quasi-two-dimensional fluids, improvement of chaotic mixing in Stokes flows, and period control of sawtooth oscillations in nuclear fusion plasmas. By using the qualitative nonlinear properties of these dynamical phenomena, open-loop control schemes are developed. After successful implementation of these schemes, novel feedback-based strategies for controlling the mixing of fluids and the sawtooth period are derived and implemented, thereby providing more efficient and more reliable solutions.

1.1 Fluid and plasma dynamics

The four most common states of matter are solid, liquid, gas, and plasma. Already in 1757 Euler derived equations [1] for fluid (i.e. liquid and gas) and gas dynamics (in 1821 extended to the Navier-Stokes equations [2]) and in 1942 Alfvén derived the magnetohydrodynamic (MHD) equations [3] to describe plasmas [4, 5]. As these theories are systems of partial differential equations that become strongly nonlinear for most of the relevant experimental regimes, many plasma and fluid phenomena remain difficult to understand analytically. Therefore, fluid dynamics and plasma physics still form lively research fields studying a plethora of open scientific questions, being very relevant for many industrial applications and society in general. This is demonstrated by applications that are considered in this thesis.

1.1.1 Applications in fluid dynamics

Examples of applications in which fluid dynamics plays a crucial role include: aerodynamics of airplanes and vehicles, weather and climate prediction, and mixing of polymers or foods. Especially the understanding of turbulence (highly irregular and unpredictable flows) and the question whether solutions of the three-dimensional Navier-Stokes equations always exist are among the most difficult and long-standing open problems in classical physics and mathematics [6], respectively. Nevertheless, also simpler phenomena - such as laminar flows, quasi-two-dimensional flows, and mixing of particles in laminar flows - are still not completely understood and their study remains relevant.

More concretely, it was only recognized in the 1980s that even in very simple (laminar) flows, particles can still follow complex trajectories [7] thereby enhancing mixing, whereas laminar flows appear simple from an Eulerian perspective, the Lagrangian behavior of the particle trajectories can be chaotic in the proper dynamical sense [8, 9]. This can drastically improve mixing of material in laminar flows. As many mixing processes in industry occur in laminar flows, the application of this mechanism can be crucial for the design of efficient mixers.

Quasi-two-dimensional flows typically occur in a fluid layer with a depth that is (very) small compared to the length of the domain. Such flows behave very differently than ordinary three-dimensional flows [6, 10]. They typically self-organize into large domain-filling vortices (rotating fluid structures) because of the inverse energy cascade [11]. Also, long living coherent structures, e.g. dipoles and tripoles, can emerge [12].

Apart from the mentioned purely fluid-dynamical examples, it is noteworthy to realize that fluids and plasmas have more in common than the fact that the MHD equations describing plasma flows are an extension of the Navier-Stokes equations. Magnetically confined plasma flows show phenomena analogous to two-dimensional fluid phenomena, e.g. self-organization and relaxation [13], and attempts to theoretically explain these phenomena are often similar as well [2, 13].

1.1.2 A p.d.e. with a switching condition

In magnetic confinement nuclear fusion research, hot plasma is confined by magnetic fields [5, 15]. In a tokamak, a strong magnetic field $\vec{B}$ consisting of a strong toroidal component B_ϕ and a weaker poloidal component B_θ is set up. It can be shown that the plasma is organised in surfaces (referred to as flux-surfaces)

on which the pressure is constant, and in which the helical field lines are embedded. The flux surfaces can be labelled by the minor radius r. The number of toroidal orbits a field line carries out in order to carry out a single poloidal orbit is referred to as the safety factor q. This variable q is constant on a flux surface, and varies from surface to surface. The radial derivative of q is called the magnetic shear s. Both q and s are associated with the stability of the plasma [5, 17].

If in a tokamak plasma the safety factor is smaller than one ($q < 1$) and the magnetic shear exceeds a critical value, the so-called internal kink mode [5] is destabilised. This leads to a fast reorganisation of the core plasma, followed by a slow transient to the instability condition. Hence, the so-called 'sawtooth crash' leads to a periodic relaxation oscillation of several core plasma variables (e.g. the core temperature, pressure, and density) and is important because it can trigger other MHD instabilities (e.g. a neo-classical tearing mode (NTM) [5, 15]) which can cause a sudden disruption of the plasma. In general, a small sawtooth oscillation period τ_{ST} is needed. Because of its relevance for operating a tokamak, many studies to control this period have been carried out over the last two decades [18]. Sawtooth period control implies that control of the period of a stable limit cycle [16, 24] is needed, which from a dynamics and control systems perspective is very interesting.

1.2 Three specific topics

In this thesis we focus on three of the aforementioned topics:

1. Vortex patterns in quasi-two-dimensional flows
2. Mixing in laminar flows
3. Periodic sawtooth oscillations in tokamak plasmas

More precisely, we are not only concerned with the analysis of several of these problems but also by the question how to influence and manipulate these processes into creating behavior that is desired. From an engineering perspective, the most obvious approach to the latter problem is to apply feedback control [19] (given a suitable control input and measured output). With this approach, a control law is designed that computes real-time an input (or forcing) to the process as a function of the measured output variables, such that the process behaves as

desired. Typically, a control law is derived from a model of the process (often being an ordinary differential equation). For systems described by partial differential equations (p.d.e.) this methodology has only been constructed for relatively simple linear partial differential equations [20, 21], while only rather specific results exist for control of Navier-Stokes equations (fluid dynamics) and MHD equations (plasmas) [22]. Moreover, these methods critically depend on good and fast measurements of the process. These are often hard or impossible to acquire in the mentioned processes, especially in fusion reactor conditions, making feedback control not necessarily suited or implementable. Besides, much of the theoretical work on p.d.e. control has typically not been validated experimentally yet, leaving some uncertainty whether a control law based on this work is practically implementable and whether it can deal with experimental artefacts such as measurement noise, model uncertainty, and time-variance.

Because of these uncertainties, it is not trivial to come up with realistic control approaches for the three mentioned problems; not only are the models of these problems *nonlinear partial differential equations*, for which it is often very difficult to construct control laws, but some of the objectives (i.e. controlling a period and intentionally creating chaotic solutions) are nonstandard control objectives directly related to the nonlinear nature of the problems and have not been theoretically analyzed within the p.d.e. feedback control framework yet.

Therefore, before introducing the novel control solutions in more detail, we first make a detour into some typical phenomena in nonlinear dynamics. These phenomena are directly related to the three mentioned problems (vortex stabilization, improved mixing, and sawtooth period control) and the related examples will show that some paradigms for the dynamics and control of linear systems do not hold for nonlinear systems. The main observation is that although nonlinear systems are more difficult to analyse, their richer behavior can create opportunities for simple control. After exemplifying this, we continue with the implications of these observations for our three problems and pose the question whether the same nonlinear phenomena occur in our three problems and whether the phenomena can be used for controlling these problems.

1.3 Qualitative aspects of nonlinear dynamics

In this section we discuss some well-known nonlinear phenomena that are relevant for the discussed plasma and fluid problems and that are not observed

in linear dynamical systems. A general (re)formulation of an n-th order ordinary differential equation is the state-space (or phase-space) description [19], which is typically used in dynamics and control and given by

$$\dot{\vec{x}} = f(\vec{x}) + g(\vec{x})u, \tag{1.1}$$

where $\vec{x} = [x_1, x_2, \ldots, x_n]^T$ is the n-dimensional state vector, $\dot{\vec{x}} := \frac{d}{dt}\vec{x}$ the derivate of $\vec{x}$ with respect to time, f and g are functions of $\vec{x}$, and u is the control input that will vary over time. If feedback control is applied u depends on $\vec{x}$, otherwise it only depends on time $u(t)$. If the system is linear time-invariant, or if the nonlinear system (1.1) is linearized around an operating point [24] it can be described by

$$\dot{\vec{x}} = \underline{A}\vec{x} + \vec{B}u, \tag{1.2}$$

where $\underline{A}$ is an $n \times n$ matrix and $\vec{B}$ an $n \times 1$ vector, assuming that u is scalar-valued.

1.3.1 Autonomous systems

A system is autonomous if it has no explicitly time-dependent input[1], or if $u = 0$ in (1.1). The pendulum is a classical example of a nonlinear system in physics and its dynamics is given by

$$\frac{d}{dt}\begin{bmatrix} x_1 \\ x_2 \end{bmatrix} = \begin{bmatrix} x_2 \\ -\sin(x_1) - \lambda x_2 + u \end{bmatrix}, \tag{1.3}$$

where the angle of the pendulum is $x_1 \in \mathbb{R}$, the angular velocity $x_2 \in \mathbb{R}$, the input $u = 0$, and $\vec{x} = [x_1, x_2]^T$. The parameter λ denotes the damping coefficient. The (stationary) equilibria of this system are determined by setting $\dot{\vec{x}} = 0$ which implies $x_2 = 0$ and $\sin(x_1) = 0$, resulting in $x_1 = 0 \mod 2\pi$ (hanging) and $x_1 = \pi \mod 2\pi$ (upright). Observe that there are an infinite number of isolated equilibria and that this can never occur in a linear time-invariant system. A standard stability analysis [24] of the linearized dynamics around the equilibria reveals that the downward equilibrium $x_1 = 0 \mod 2\pi$ is stable and the upward position $x_1 = \pi \mod 2\pi$ is unstable. Therefore, almost all solutions (apart from $x_1 = \pi \mod 2\pi$ and $x_2 = 0$) will eventually converge towards the stable equilibrium $\vec{x} = \vec{0}$. Another system with an infinite number of stable and unstable equilibria is the first order system

[1] In the case of static state feedback control in which the input u is a function of the state x and not of time t, the closed-loop system can then be reformulated as an autonomous system $\dot{\vec{x}} = f(\vec{x}) + g(\vec{x})u(\vec{x})$ as in (1.1).

$\dot{x} = \sin(x)$, with $x \in \mathbb{R}$ and equilibria $x = 0 \bmod \pi$. This example shows that it can depend on the initial condition to which equilibrium a solution converges; there are several different 'regions of attraction' [24].

Apart from having several equilibria, solutions of nonlinear autonomous systems do not necessarily converge to a constant solution (i.e. a stationary equilibrium) but can also converge towards other 'attractors', such as an isolated periodic solution (i.e. a stable 'limit cycle') or to aperiodic and even 'chaotic' solutions [9]. A classical example of a system with a limit cycle is the second order van der Pol oscillator with vanishing input ($u = 0$) [23, 9, 24] given by

$$\begin{aligned} \dot{x}_1 &= x_2 \\ \dot{x}_2 &= -x_1 + \epsilon(1 - x_1^2)x_2 + u, \end{aligned} \tag{1.4}$$

with $\epsilon > 0$. The Poincaré-Bendixson theorem implies that, for continuous systems, limit cycles can only occur in nonlinear systems with at least two states [16, 9, 24]. For hybrid systems [25], however, periodic solutions can also occur for first order systems (e.g. the integrate-and-fire system in neuroscience [26, 27], as is discussed in Chapter 6). The most famous example of a chaotic system is the (third order) Lorenz equation [28, 9]. Depending on the initial conditions and parameter values, the solutions can be chaotic, which implies that they are aperiodic and that perturbations can cause exponential divergence of solutions [9].

What we learn from these examples is that multiple and different types of attractors can exist simultaneously in the same nonlinear system. In that case, the initial condition determines the steady-state behavior and the state space is demarcated into several regions with qualitatively different dynamics. In Hamiltonian systems there is no energy dissipation and they have a particular structure [29]. For example, the undamped pendulum (1.3) with $\lambda = 0$, is a particular instance of a Hamiltonian system. In the state space of these systems there are no real attractors, but the state space is typically still demarcated in regions with periodic and regions with chaotic behavior [29]. This is relevant for many physical applications including chaotic mixing and transport in fluids [7, 8], as considered in this thesis. The trajectories of particles in an incompressible 2D flow $\vec{v}(x, y, t)$ are governed by the second order differential equation $\dot{\vec{x}} = \vec{v}(x, y, t)$, with particle position $\vec{x} = [x, y]^T$. For 2D time-invariant flows only periodic or stationary behavior is possible. As incompressibility implies $\nabla \cdot \vec{v} = 0$, this is a Hamiltonian system with Hamiltonian $\psi(x, y, t)$ and the velocity field is defined as $\vec{v} = [-\partial\psi/\partial y, \partial\psi/\partial x]^T$.

If $\vec{v}(x,y,t)$ is time-dependent then there can be regions in the state space where solutions (i.e. particle trajectories) behave chaotically, which improves mixing, as we will see in Chapters 3 and 4.

Summarizing, contrary to linear systems, autonomous nonlinear systems can have multiple attractors of different types (stationary, periodic or chaotic), and even if there are no attractors, there still can be multiple regions in the state-space with qualitatively different dynamics.

1.3.2 Nonautonomous systems

Adding a time-varying input u to a nonlinear system (1.1) can change the behavior more dramatically than for a linear system (1.2) and can result in counter-intuitive phenomena. A classical example is the stabilization of the unstable (upright) equilibrium of the pendulum, given by $x_1 = \pi$, $x_2 = 0$, (1.3) by periodically vibrating the joint of the pendulum vertically with an input $u(t) = \epsilon \sin(\omega t)$ for a high frequency ω and small amplitude ϵ [30, 22, 24, 16][2]. If the initial condition is close to $x_1 = \pi$, $x_2 = 0$ then the vertical forcing results in a small periodic oscillation around that equilibrium [24]. This input can therefore be considered to practically stabilize the unstable upright equilibrium. The observation that periodic inputs can lead to practical stabilization, without the need for real-time measurements, inspired the development of vibrational control [22], an open-loop control strategy aimed at the stabilization of nonlinear systems. This stabilization phenomenon has also been observed in certain fluid and plasma problems [23, 33], but has not been rigorously explained for these settings.

Observe that, contrary to linear systems, the excitation of a nonlinear system with a sinusoidal input does not necessarily result in a sinusoidal response with the same frequency (in steady-state). For example, the period of a system with a stable limit cycle (e.g. the van der Pol oscillator (1.4)) can adapt and become similar to the period of an input $u(t) = \epsilon \sin(\omega t)$ if the input period $2\pi/\omega$ is close enough to the autonomous period T_p [16]. This phenomenon is called 'mode locking', 'period

[2]Note that the stability proof in [24] p. 409 is different from the proof in [22], as the order of averaging and linearizing is reversed. Strictly speaking, the founding article of vibrational control [22] only proves stabilization of the linearized system and not of the original nonlinear system. Although vibrational control has been successfully applied to a number of problems in different fields, there seems to be no general theory that completely explains all instances of this phenomenon. Especially for distributed-parameter systems (modeled by partial differential equations) there are no stability proofs in this context.

locking' or 'entrainment' and has been observed in a large number of technical, physical and biological oscillators [34]. Again, the phenomenon is not restricted to low-dimensional oscillators but can also occur in distributed-parameter systems [35, 34] (i.e. systems governed by partial differential equations, typically reaction-diffusion equations).

A periodic input can not only change the stability or the period of an attractor but can even lead to behavior normally associated with another attractor. If the pendulum (a system with two stationary equilibria) or the van der Pol equation (a system with a limit cycle) are driven periodically, then this can result in chaotic behavior [36, 37]. This implies that chaos can occur in (continuous) autonomous systems with at least three states but also in nonautonomous systems with at least two states. This fact is used in the example of chaotic mixing in the previous section, where chaos occurs in a 2D state space if the flow field $\vec{v}(x, y, t)$ is time-dependent.

To summarize the most important observations for this thesis, for certain nonlinear systems periodic (or more generally time-varying) inputs can lead to practical stabilization of an unstable equilibrium, can change the oscillation period, and can change the qualitative nonlinear dynamics. This implies that, contrary to stable linear systems where the steady-state behavior has the same frequency as the input, the qualitative behavior of nonlinear systems can change more drastically because of a periodic input. Not only can this observation be used for controlling complex nonlinear systems (as will be shown in this thesis), but it also implies that behavior of nonlinear systems can drastically change if it interacts with another system, as the interaction can be interpreted as an input. This is consistent with the observation that the behavior of open physical systems (with an input or interacting with other systems) can be very different from closed systems [38]. Although this perspective is not emphasized in this thesis, it can be relevant for physics and other applications, as can be seen in, for example, the Turing instability, where the coupling of two (stable) diffusion partial differential equations can cause the combined system to become unstable [39, 40, 41], a phenomenon also observed for linear and nonlinear ordinary differential equations [42, 43]. This emphasizes the necessity to study the influence of inputs on physical systems. Within the context of the work in this thesis, a relevant example of two interacting open systems is the interaction between the sawtooth and the ELM (edge-localized-mode) oscillation in a tokamak, where it has been observed in experiments that the ELM period can lock to (or synchronize with) the period of the sawtooth oscillation [44].

We stress that although the discussed phenomena are exemplified by low-order ordinary differential equations such as the pendulum dynamics, all these nonlinear phenomena have been observed and/or analyzed in distributed-parameter systems as well [34, 35, 33, 23]. This motivates the questions whether the discussed nonlinear phenomena, caused by a periodic input, can also appear in the main three nonlinear fluid and plasma problems studied in this thesis and whether these phenomena can be applied for control purposes. These questions are exactly the main points of departure for the exploration in this theisis.

1.4 Questions, models, and contributions

The central idea in this thesis is that the strongly nonlinear behavior of certain fluid and plasma processes, although leading to difficult analysis problems, can actually be highly beneficial for controlling these processes. The understanding of the qualitative nonlinear behavior of the processes at hand gives rise to nonstandard control objectives and can lead to the construction of effective open-loop control by applying a time-periodic input. Moreover, successful (periodic) open-loop control can inspire more efficient and robust *feedback* control approaches. This might lead to an aperiodic input signal.

To introduce the open-loop and feedback control strategies, we first introduce the basic relevant models (mostly p.d.e.'s) that describe two-dimensional flows, chaotic mixing, and the sawtooth oscillation and then pose the questions that we will deal with in this thesis.

Flows in a shallow-fluid-layer can often be described by the Navier-Stokes equations for incompressible fluids. These equations describe the evolution of the velocity field $\vec{v}(x,y,z,t)$ as follows [6]

$$\begin{aligned} \frac{\partial \vec{v}}{\partial t} &= -\vec{v}\cdot\nabla\vec{v} - \frac{1}{\rho}\nabla p + \nu\nabla^2\vec{v} - \kappa\vec{v} + \frac{1}{\rho}\vec{J}\times\vec{B} \\ \nabla\cdot\vec{v} &= 0, \end{aligned} \tag{1.5}$$

where p is the pressure, ν the viscosity, ρ the density, and the term $\vec{J}\times\vec{B}/\rho$ is the Lorentz force created by the interaction of an electrical current $\vec{J}$ and a magnetic field $\vec{B}$. Under certain conditions a shallow-fluid-layer flow can be described by the 2D version of Navier-Stokes and then (and only then) the term $\kappa\vec{v}$ in (1.5) is added to model 3D bottom effects (Rayleigh friction) [10]. It is known that the 2D Navier-Stokes equations have infinitely many unstable equilibria.

This leads to the following question: *Are there unstable equilibria in quasi-two-dimensional flows that, analogously to vibrational control, can be stabilized by a time-periodic forcing?* In Chapter 2, it is shown that one can indeed experimentally stabilize a certain unstable equilibrium of the 2D Navier-Stokes equations by applying a time-periodic Lorentz force.

As is discussed in the previous section, it is well-known - within the mixing community - that particles in time-periodic two-dimensional laminar flows can follow chaotic trajectories and that this mechanism - known as chaotic advection - leads to more efficient mixing. Given is a scalar field $c(x,y,t)$ (e.g. a concentration distribution) that is redistributed by a velocity field $\vec{v}(x,y,t)$ (governed by the Navier-Stokes equations, with small Reynolds number). The transport and mixing of $c(x,y,t)$ is described by the advection-diffusion partial differential equation

$$\frac{\partial c}{\partial t} = -\vec{v}\cdot\nabla c + \frac{1}{Pe}\nabla^2 c. \tag{1.6}$$

The Péclet number Pe is typically assumed to be very high and therefore advection is dominant. The partial differential equation (1.6) describes the transport of material from an Eulerian perspective. However, from a Lagrangian perspective, mixing is related to the particle trajectories $\vec{x}(t) = [x,y]^T(t)$ (in 2D). The given velocity vector field $\vec{v}(x,y,t)$ defines the dynamics of these particles in the two-dimensional state space with coordinates x and y

$$\dot{\vec{x}} = \vec{v}(\vec{x},t). \tag{1.7}$$

As stated in the previous section, in a two-dimensional domain particle trajectories can only become chaotic when the vector field is time-dependent. For mixing studies the (divergence-free) vector field is typically taken to be periodic, i.e. $\vec{v}(x,y,t) = \vec{v}(x,y,t+T)$ for some period $T > 0$. This Hamiltonian system has solutions that are stationary, periodic or chaotic, where the character of each solution depends on the initial position at time $t = 0$. For this reason, the entire state space at $t = 0$ can be partitioned in regions with all the particles trajectories starting in the same region have the same character. If the particles in such a region have periodic trajectories, then the region is called a 'periodic island' while if the trajectories starting in a region are chaotic then such a region is called a 'chaotic sea' [45]. For good mixing it is important that the periodic islands are small, as material in such an island does not mix. The size of the periodic islands and the quantitative properties of the chaotic sea do not only depend on the form of $\vec{v}(x,y,t)$ but also depend on the value of the period T. It is already very well-known that the time

variance of the field $\vec{v}(x,y,t)$ influences mixing [8]. As is explained in Chapter 3, the mixing properties of a given periodic flow can be analysed by discretizing both time and space, leading to the mapping matrix description [46, 45]

$$\vec{c}(t+T) = \underline{\Phi}\vec{c}(t). \tag{1.8}$$

In (1.8), the concentration vector $\vec{c} = [c_1, c_2, \ldots c_n]^T$ is based on a discretization of the space into n cells, with c_i describing the concentration in the i-th cell. The matrix Φ is therefore $n \times n$ and typically has a (very) large size but is sparse.

A general question is: *Given a certain time-periodic flow, does this flow lead to effective mixing or does it have large periodic islands?* One possible approach to study this question, is to do simulations with the mapping matrices that describe the mixing in a given flow for a number of different time periods. Previous numerical work by Singh et al. [45] lead to five conjectures about the relation between the mapping matrix and mixing. In Chapter 3, an analysis of the general structure of the mapping matrix shows that these conjectures are correct. Besides this, general structural properties of the matrix $\underline{\Phi}$ are derived that determine whether a given mapping matrix (and its associated flow) leads to efficient mixing. Moreover, in Chapter 4 it is shown that the mapping matrix formalism is suited to model a given mixing problem as a switching system. This facilitates the design of efficient, not necessarily periodic, flows for mixing and the design of feedback control for mixing based on switching control theory [47]. As the method employs a finite state vector (approximating the spatial concentration distribution), it is relatively straightforward to implement this control law in experiments by using a digital camera to measure the concentration state. These experiments have been performed and compared with simulations and analytical results.

The third main problem considered in this thesis concerns the control of the sawtooth period in fusion plasmas. As introduced in Section 1.1.2, the sawtooth oscillation is a relaxation oscillation (limit cycle) in the core magnetic field of a tokamak plasma [48] that is caused by an MHD instability in the magnetic field. The MHD equations [4, 5] describing the evolution of the magnetic field are a combination of the Navier-Stokes equations (1.5), the Maxwell equations [3, 13] and additional equations for the evolution of density and pressure, leading to

$$\begin{aligned} \frac{\partial \vec{B}}{\partial t} &= \nabla \times (\vec{v} \times \vec{B}) - \nabla \times (\frac{\eta}{\mu_0} \nabla \times \vec{B} + \eta J_{ni}) \\ \nabla \cdot \vec{B} &= 0 \\ \mu_0 \vec{J} &= \nabla \times \vec{B} \end{aligned} \tag{1.9}$$

where η is the resistivity, $\mu_0 = 4\pi \cdot 10^{-7}\ NA^{-2}$ the vacuum magnetic permeability, and J_{ni} is a non-inductive current that can be used as an input to influence the magnetic field. Observe that the magnetic field $\vec{B}$ influences the plasma flow in (1.5) by the Lorentz force and the flow $\vec{v}$ influences the magnetic field through the term $\nabla \times (\vec{v} \times \vec{B})$, but whether these coupling terms are significant or not depends on the specific regime. For example, in the experiments in Chapter 2, the flow is assumed to be driven by the Lorentz force $\vec{J} \times \vec{B}$ in (1.5) and it is implicitly assumed that the flow $\vec{v}$ does not influence $\vec{B}$. In fusion plasmas, however, this partial decoupling assumption is often not correct.

Although the sawtooth crash is believed to be caused by an MHD instability of the magnetic field (the internal kink mode [5, 13]) the MHD equations are too complex to be used for analyzing the oscillation. However, the work of a number of authors, e.g. [4, 50], has resulted in a simpler model which is based on a combination of first principles and heuristics. This model, as has been synthesized in [50], is a combination of a partial differential equation describing the diffusion of the poloidal magnetic field B_θ on the slow time scale given by

$$\frac{\partial B_\theta}{\partial t} = \frac{\partial}{\partial r}\left(\frac{\eta}{\mu_0 r}(B_\theta + r\frac{\partial}{\partial r}B_\theta) - \eta J_{ni}\right), \tag{1.10}$$

and a reset to model the sawtooth crash (the fast time scale). The poloidal magnetic field is instantaneously changed at the moment that the reset condition

$$1 - \frac{r dB_\theta}{B_\theta dr} = s_c \tag{1.11}$$

is met, where s_c is a parameter that depends on the experimental regime.

Simulations with this model show periodic behavior similar to the sawtooth oscillation (i.e. it shows limit cycle-like behavior). This leads to the following main question: *Can the period of this oscillation lock to the period of the input J_{ni}?* Simulations by Witvoet et al. [51] confirm that periodic power modulation of J_{ni} can result in period locking of the sawtooth period. In Chapter 5, experiments are presented that confirm that period locking really appears in sawtooth oscillations in tokamak plasmas. Moreover, a method ('pacing') in which the input J_{ni} is controlled by a feedback law has been tested successfully in experiments by Goodman et al. [52]. In Chapter 6 this pacing method has been analysed using a reduced model of the sawtooth period. Conditions are given for which this method indeed can be proven to be stable and robust.

1.5 Outline of this thesis

The remainder of this thesis is organized as follows. Chapter 2, 3, and 4 are concerned with fluid flows (both two-dimensional flows and mixing), and Chapter 5 and 6 deal with the sawtooth oscillation in fusion plasmas. More precisely, in Chapter 2 it is experimentally shown that a periodic input can cause stabilization of an equilibrium of the 2D Navier-Stokes equations and that aperiodic time-varying inputs can cause an unknown form of self-organized vortex patterns [54]. These experimental results are consistent with theory [53]. Next, in Chapter 3 analytical results on chaotic mixing are presented, which rely on using the mapping matrix formalism [55]. This same formalism is used in Chapter 4 to show that mixing problems can be efficiently modeled as switching systems [56]. This novel perspective can be used to study and create aperiodic protocols that mix faster than periodic protocols applied in open loop. In addition, this perspective can also be used to derive aperiodic feedback-based protocols to increase the robustness for model uncertainties. Experiments confirm these theoretical claims. In Chapter 5, we show experimental evidence that the period of the sawtooth oscillation locks to a periodically modulated input signal [57]. In Chapter 6 an analysis of a reduced model of the sawtooth period is carried out yielding the conditions for which pacing is guaranteed to work [58]. Hereafter, the conclusions, summary, and the acknowledgements are presented.

1.6 List of publications

Chapters 2, 3 and 5 have been published in peer reviewed journals [54, 55, 57]. Chapter 4 [56] and Chapter 6 [58] are to be submitted. A complete list consisting of journal articles by the author can be found below

M. Lauret, V.S. Dolk, D.J. Antunes, P.D. Anderson, W.P.M.H. Heemels
Chaotic aperiodic mixing from a switching dynamics perspective
(2014) To be submitted for journal publication.

M. Lauret, M. Lennholm, M.R. de Baar, W.P.M.H. Heemels
Pacing control of sawtooth oscillations in fusion plasmas
(2014) To be submitted for journal publication.

D.P. Borgers, M. Lauret, M.R. de Baar
Kalman filters for real-time magnetic island phase tracking
(2013) Fusion Engineering and Design 88 (11) pp. 2922 - 2932.

M. Lauret, L.P.J. Kamp, G.J.F. van Heijst, M.R. de Baar, H. Nijmeijer
Experimental stabilisation of 2D vortex patterns using time-dependent forcing
(2013) Europhysics Letters 104 (2) 24003.

M.F.M. Speetjens, M. Lauret, H. Nijmeijer, P.D. Anderson
Footprints of Lagrangian flow structures in Eulerian concentration distributions in periodic mixing flows
(2013) Physica D: Nonlinear Phenomena 250, pp. 20 - 33

B.A. Hennen, M. Lauret, G. Hommen, W.P.M.H. Heemels, M.R. de Baar, E. Westerhof
Nonlinear control for stabilization of small neoclassical tearing modes in ITER
(2012) Nuclear Fusion 52 (6) 063007.

M. Lauret, F. Felici, G. Witvoet, T.P. Goodman, G. Vandersteen, O. Sauter, M.R. de Baar, the TCV team
Demonstration of sawtooth period locking with power modulation in TCV plasmas
(2012) Nuclear Fusion 52 (6) 062002.

G. Witvoet, M. Lauret, M.R. de Baar, E. Westerhof, M. Steinbuch
Numerical demonstration of injection locking of the sawtooth period by means of modulated EC current drive
(2011) Nuclear Fusion 51 (10) 103043.

I. Belykh, M. Hasler, M. Lauret, H. Nijmeijer
Synchronization and graph topology
(2005) International Journal of Bifurcation and Chaos in Applied Sciences and Engineering 15 (11) pp. 3423 - 3433.

Bibliography

[1] U. Frisch, translation of Leonhard Euler's: General principles of the motion of fluids, published online arXiv:0802.2383v1.

[2] M. Cannone, S. Friedlander, Navier: Blow-up and Collapse, Notices of the AMS, January, 2003, pp. 7-13.

[3] H. Alfvén, Nature 150, 1942, pp. 405-406.

[4] H. Goedbloed, S. Poedts, Principles of magnetohydrodynamics; with applications to laboratory and astrophysical plasmas, Cambridge University Press, 2004.

[5] J.P. Freidberg , Plasma physics and fusion energy, Cambridge University Press, 2008.

[6] C.R. Doering and J.D. Gibbon, Applied analysis of the Navier-Stokes equations, Cambridge University Press, 1995.

[7] H. Aref, Stirring by chaotic advection, Journal of Fluid Mechanics 143, 1984, pp. 1-21.

[8] J.M. Ottino, The kinematics of mixing: stretching, chaos, and transport, Cambridge University Press, 1989.

[9] S.H. Strogatz, Nonlinear dynamics and chaos, Westview Press, 2001.

[10] H.J.H. Clercx and G.J.F. van Heijst, Two-dimensional Navier-Stokes turbulence in bounded domains, Applied Mechanics Reviews 62, 2009, 020802.

[11] H. Kraichnan, Inertial ranges in two-dimensional turbulence, Physics of Fluids 10, 1967, pp. 1417-1423.

[12] G.J.F. van Heijst, R.C. Kloosterziel, Tripolar vortices in a rotating fluid, Nature 338, 1989, pp. 569-571.

[13] D. Biskamp, Nonlinear magnetohydrodynamics, Cambridge University Press, 1997.

[14] A. Hasegawa, Self-organization processes in continuous media, Advances in Physics 34, 1985, pp. l-42.

[15] G. McCracken, P. Stott, Fusion: the energy of the universe, Elsevier Academic Press, 2005.

[16] M. Farkas, Periodic motions, Springer-Verlag, New-York, 1994.

[17] J.P. Freidberg, Ideal magnetoyhydrodynamics, Plenum Press, New York, 1987.

[18] I.T. Chapman, Controlling sawtooth oscillations in tokamak plasmas, Plasma Physics and Controlled Fusion 53, 2011, 013001.

[19] K.J. Åström and R.M. Murray, Feedback systems: An introduction for scientists and engineers, Princeton University Press, 2008.

[20] M. Krstic and A. Smyshlyaev, Boundary control of PDEs : a course on backstepping designs, Philadelphia : SIAM, 2008.

[21] R.F. Curtain and H.J. Zwart, An introduction to infinite-dimensional linear systems theory, Springer-Berlin, 1995.

[22] R. Vazquez and M. Krstic, Control of turbulent and magnetohydrodynamic channel flows : boundary stabilization and state estimation, Boston MA : Birkhäuser Boston, 2008.

[23] B. Van der Pol, On relaxation-oscillations, London, Edinburgh and Dublin Philosophical Magazine and Journal of Science 2(7), 1926, pp. 978-992.

[24] H.K Khalil, Nonlinear systems, Prentice Hall, 2001.

[25] R. Goebel, R.G. Sanfelice, A.R. Teel, Hybrid dynamical systems, Princeton University Press, 2012.

[26] L. Lapicque, Recherches quantitatives sur l'excitation électrique des nerfs traiteé comme une polarization, Journal de physiologie et de pathologie générale 9, 1907, pp. 620-635.

[27] E.M. Izhikevich, Dynamical systems in neuroscience, MIT Press, Cambridge, 2006.

[28] E.N. Lorenz and Edward Norton, Deterministic nonperiodic flow, Journal of the Atmospheric Sciences 20, 1963, pp. 130-141.

[29] G.M. Zaslavsky, Hamiltonian chaos and fractional dynamics, Oxford, 2008.

[30] A. Stephenson, On an induced stability, Philosophical Magazine 15, 1908, pp. 233-236.

[31] S.M. Meerkov, Principle of vibrational control: theory and applications, IEEE Transactions on Automatic Control 25, 1980, pp. 755-762.

[32] S.M. Meerkov, Vibrational stabilizability of distributed parameter systems, Journal of mathematical analysis and applications 98, 1984, pp. 408-418.

[33] G. Berge, Equilibrium and stability of MHD-fluids by dynamic techniques, Nuclear Fusion 12, 1972, pp. 99-118.

[34] A. Pikovsky, M. Rosenblum, and J. Kurths, Synchronization: A universal concept in nonlinear sciences, Cambridge University Press, 2003.

[35] Y. Kuramoto, Chemical oscillations, waves, and turbulence, Dover Publications, 2003.

[36] B. van der Pol and J. van der Mark, Frequency demultiplication, Nature 120, 1927, pp. 363-364.

[37] C. Grebogi, E. Ott, J.A. Yorke, Chaos, strange attractors, and fractal basin boundaries in nonlinear dynamics, Science 30, 1987, pp. 632-638.

[38] H. Haken, Synergetics, an introduction: Nonequilibrium phase transitions and self-organization in physics, chemistry, and biology, Springer-Verlag, 1983.

[39] A. M. Turing, The chemical basis of morphogenesis, Philosophical Transactions of the Royal Society B 237, 1952, 37.

[40] N.F. Britton, Reaction-Diffusion equations and their applications to biology, Academic Press, 1986.

[41] P. Grindrod, The theory and applications of reaction-diffusion equations: patterns and waves, Oxford University Press, 1996.

[42] S. Smale, A mathematical model of two cells via Turing's equation, in the Hopf bifurcation and its applications, J. E. Marsden and M. Mc- Cracken, Eds. New York, NY: Springer-Verlag, 1976, pp. 354-367.

[43] A.Y. Pogromsky, H. Nijmeijer, Cooperative oscillatory behavior of mutually coupled dynamical systems. IEEE Transactions on Circuits and Systems. I, Fundamental Theory and Applications, 48(2), 2001, 152-162.

[44] Y.R. Martin, A.W. Degeling, and J.B. Lister, Search for determinism in ELM time series in TCV, Plasma Physics and Controlled Fusion 44, 2002, pp. 373-382.

[45] M.K. Singh, M.F.M. Speetjens, and P.D. Anderson, Eigenmode analysis of scalar transport in distributive mixing, Physics of Fluids 21(9), 2009, 093601.

[46] P. D. Anderson, O. S. Galaktionov, G. W. M. Peters, H. E. H. Meijer, and C. L. Tucker, Material stretching in laminar mixing flows: Extended mapping technique applied to the journal bearing flow, International Journal for Numerical Methods in Fluids 40, 2002, pp. 189-196.

[47] D. Liberzon, Switching in Systems and Control, Birkhäuser, Boston, 2003.

[48] S. von Goeler, W. Stodiek, and N. Sauthoff Studies of Internal Disruptions and $m = 1$ Oscillations in Tokamak Discharges with Soft-X-Ray Techniques, Physical Review Letters 33, 1974, pp. 1201-1203

[49] F. Porcelli, D. Boucher, and M.N. Rosenbluth, Model for the sawtooth period and amplitude, Plasma Physics and Controlled Fusion 38, 1996, pp. 2163-2186.

[50] G. Witvoet, M.R. de Baar, E. Westerhof, M. Steinbuch, and N.J. Doelman, Systematic design of a sawtooth period feedback controller using a Kadomtsev-Porcelli sawtooth model, Nuclear Fusion 51 (7), 2001, 073024.

[51] G. Witvoet, M. Lauret, M.R. de Baar, M.R., E. Westerhof, M. Steinbuch, Numerical demonstration of injection locking of the sawtooth period by means of modulated EC current drive, Nuclear Fusion 51(10), 2011, 103043.

[52] T.P. Goodman, F. Felici, O. Sauter, J.P. Graves, and the TCV Team, Sawtooth pacing by real-time auxiliary power control in a tokamak plasma, Physical Review Letters 106, 2011, 245002.

[53] E. van Groesen, Time-asymptotics and the self-organization hypothesis for 2D Navier-Stokes equations, Physica A 148, 1988, pp. 312-330.

[54] M. Lauret, L.P.J. Kamp, G.J.F. van Heijst, M.R. de Baar, and H. Nijmeijer, Experimental stabilisation of 2D vortex patterns using time-dependent forcing, Europhysics Letters 104, 2013, 24003.

[55] M.F.M. Speetjens, M. Lauret, H. Nijmeijer, and P.D. Anderson, Footprints of Lagrangian flow structures in Eulerian concentration distributions in periodic mixing flows, Physica D: Nonlinear Phenomena 250, 2013, pp. 20-33.

[56] M. Lauret, V.S. Dolk, D.J. Antunes, P.D. Anderson, and W.P.M.H. Heemels, Chaotic aperiodic mixing from a switching dynamics perspective, to be submitted, 2014.

[57] M. Lauret, F. Felici, G. Witvoet, T.P. Goodman, G. Vandersteen, O. Sauter, M.R. de Baar, and the TCV team, Demonstration of sawtooth period locking with power modulation in TCV plasmas, Nuclear Fusion 52 (6), 2012, 062002.

[58] M. Lauret, M. Lennholm, M.R. de Baar, and W.P.M.H. Heemels, Pacing control of sawtooth and ELM oscillations in fusion plasmas, submitted, 2014.

Chapter 2

Stabilisation of 2D vortex patterns

M. Lauret, L.P.J. Kamp, G.J.F. van Heijst, M.R. de Baar, H. Nijmeijer[1]

2.1 Abstract

Experimental results of the effect of time-periodic and 'chirped' (electro-magnetic) forcing on vortex patterns in shallow-water-layer flows are presented. Analogous to vibrational control, the use of a time-periodic forcing results in stabilisation of otherwise unstable vortex patterns. Chirped frequency forcing yields self-organising patterns that are different from those in stationary and periodically forced experiments. The results are shown to be consistent with theoretical analysis of 2D Taylor-Green vortices, *i.e.* unstable analytical solutions of the 2D Navier-Stokes equation. These results imply that, compared to the more often analysed stationary forced flows, time-varying forcing can stabilise different vortex patterns in shallow-water-layer flows.

[1]This chapter is based on 'Experimental stabilisation of 2D vortex patterns using time-dependent forcing', as has been published in EPL 104 (2), 24003, 2013.

2.2 Introduction

Shallow fluid flows behave quite differently from fully three-dimensional (3D) flows. Contrary to the small length scales observed in 3D turbulence, these quasi-two-dimensional (Q2D) flows typically self-organise into large vortices [1, 3, 2, 4]. Self-organisation is, for example, seen in geophysical flows (both in the atmosphere and in the oceans), in soap films, and in electromagnetically forced shallow-water-layer experimental setups. If 3D effects are completely negligible, these flows can be modelled by the two-dimensional (2D) Navier-Stokes equation.

The Q2D behaviour of cellular flows (square arrays of vortices in a bounded domain) has been studied extensively. These flows are experimentally realised in conductive shallow fluid layers using electromagnetic forcing [5, 6, 7]. Contrary to the self-organisation in decaying Q2D flows, stationary forced flows attain a stationary state that is organised for moderate forcing amplitudes [8]. However, if the forcing amplitude is increased, the flow typically undergoes a bifurcation, consistent with theoretical analysis [9], and becomes time-periodic and eventually chaotic in time and spatially disorganised.

For certain cases, Q2D cellular flows can be described analytically as 2D Taylor-Green vortices [10]. These square vortex arrays are a family of exact solutions of the 2D Navier-Stokes equation. Their stability depends on several factors like boundary conditions, the value of the Reynolds number and magnitude and type of the forcing. Stability analysis for decaying and stationary forced 2D Taylor-Green vortices have revealed that the vortices remain stable for small Reynolds numbers [11, 12, 13, 14]. For decaying Taylor-Green vortex arrays at a higher Reynolds number, the self-organisation into a domain filling vortex can be explained using variational techniques [15, 16].

In the present paper, we report on an experimental study of the influence of different types of forcing on the stability and self-organisation of Q2D cellular flows. In particular the effect of time-varying forcing is discussed. We show that time-periodic forcing can stabilise a cellular flow that is similar to a 2D Taylor-Green vortex pattern, but different from the Taylor-Green vortex resulting from a stationary forcing with the same spatial length scale as the time-periodic one.

The remainder of this paper is organised as follows. After describing the experimental setup, experiments in which the flow is forced constantly in time are presented. Then, experimental results for time-periodic forcing are discussed. To

study the effect of aperiodic-in-time forcing, the flow resulting from 'chirp' forcing (*i.e.* with the temporal frequency of the forcing changing during the experiment) is studied. Next, the experimental results are modelled with analytical solutions of the 2D vorticity equation. In the discussion, the comparison between the theoretical analysis and the experiments, and also the role of the forcing in vortex stabilisation is discussed. Finally, some conclusions will be drawn.

2.3 Experimental setup

The experimental setup (described in more detail in [8]) consists of a square tank with length $L_0 = 0.52$ m, filled with a $NaCl$-water solution with depth $H = 8.5$ mm. The water has a density $\rho = 1142$ kg/m^3 and a kinematic viscosity $\nu = 1 \cdot 10^{-6}$ m^2/s. The surface flow is described in a Cartesian right-handed coordinate system (x, y) and the $z-$axis is perpendicular to the fluid surface.

Beneath the bottom, 100 permanent magnets of 1.1 T are arranged in a square 10×10 configuration with alternating polarity, resulting in a magnetic field $\mathbf{B}(x, y, z)$. The distance between two neighbouring magnets is $l = 5$ cm.

On opposite sides of the tank, two electrodes create a voltage difference that drives an electric current $I(t)$, which magnitude can be varied between ± 1 mA and ± 7 A. The flow is forced by a Lorentz force $\mathbf{F}_L$, resulting from the combination of the magnetic field $\mathbf{B}(x, y, z)$ and the uniform electric current density $\mathbf{J}(t) = J(t)\mathbf{e_x}$, where $\mathbf{e_x}$ is the unit vector in the $x-$direction. The magnetic field is assumed to be predominantly perpendicular to the fluid surface and z-independent, implying $\mathbf{B}(x, y) = B(x, y)\mathbf{e_z}$ (where $\mathbf{e_z}$ is the unit vector in the $z-$direction). The Lorentz force is then given by

$$\mathbf{F}_L(x, y, t) = \frac{1}{\rho}\mathbf{J} \times \mathbf{B} = -\frac{1}{\rho}J(t)B(x, y)\mathbf{e_y}, \tag{2.1}$$

where $\mathbf{e_y}$ is the unit vector in the $y-$direction. It should be noticed that this Lorentz force is strongly localised around the magnets.

To visualize the flow, small tracer particles (diameter 250 μm) float on the free fluid surface. These moving particles are recorded by a camera mounted above the setup. This camera has a sample rate of 15 frames/s and the camera records the flow in a $L \times L$ square area in the middle of the tank, with $L = 17.5$ cm. The flow can then be visualised with streak-line figures. By applying particle image velocimetry (PIV) [17], the 2D velocity fields $\mathbf{v}(x, y, t) = [u, v]^T$ can be determined.

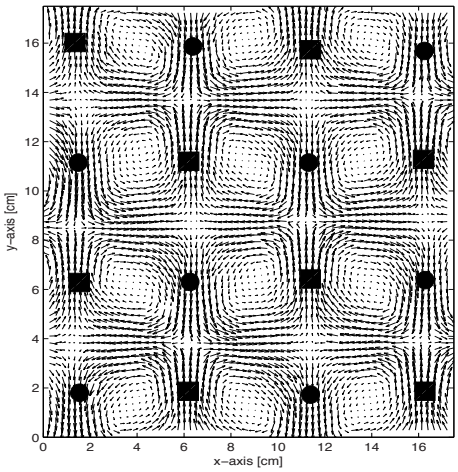

Figure 2.1: Experimentally obtained flow field (vectors denote the instantaneous velocity) with 100 magnets and a direct current $I = 20$ mA. The array of alternating, permanent magnets is indicated by the black circles (magnetic field pointing upwards) and squares (magnetic field pointing downwards). For a direct current this gives rise to an alternating Lorentz force resulting in a square array of vortices each having alternating vorticity.

From these velocity fields the vorticity $\omega = (\nabla \times \mathbf{v}) \cdot \mathbf{e_z} = \partial v/\partial x - \partial u/\partial y$, the kinetic energy $E(t) = \frac{1}{2}\int_{\mathcal{D}} |\mathbf{v}|^2 dA$, and the enstrophy $\Omega(t) = \frac{1}{2}\int_{\mathcal{D}} \omega^2 dA$ can be determined, with $\mathcal{D}$ denoting the $L \times L$ area at the fluid surface.

2.4 Experimental observations

To study the influence of the forcing on the phenomenology of emerging vortex patterns, experiments with different types of Lorentz forcing have been carried out. The first experiment studies the effect of a direct current (DC) of 20 mA. This forcing results in a square array of vortices each having a size of $l = 5$ cm, as shown in fig. 2.1. This is similar to observations by Cieślik *et al.* [8]. The vortex pattern, with approximately 3×4 vortices in the viewing area, remains stable for currents up to $I = 40$ mA.

A distinctly different vortex pattern is observed when the flow is forced with a time-periodic Lorentz force. Applying an alternating current (AC) given by

$I(t) = I_0 \sin(2\pi f t)$ (with amplitude I_0[A] and frequency f[Hz]) results in the vortex pattern shown in fig. 2.2. In this figure, snapshots of the velocity field for $f = 1$ Hz and $I_0 = 5$ A are shown at three different time instances. Vortex arrays emerge that have not been observed using a stationary forcing. It has been experimentally verified that for $0.5 < f < 5$ Hz and $1 < I_0 < 7$ A, the observed vortex array is always similar to the ones shown in fig. 2.2. From fig. 2.2 we conclude that most of the time the flow field is represented by a spatially periodic pattern of vortices, each having a size that is half the size of the vortices produced with a direct current, *i.e.* 2.5 cm, as depicted in fig. 2.2(b) and fig. 2.3. Moreover, this vortex array remains intact for amplitudes of the alternating current up to $I_0 = 7$ A, which is far above the maximum direct current (together with a suitable array of magnets) that can be used to produce such a vortex pattern that is stable.

To also investigate vortex pattern formation for more general forcing protocols, an aperiodic electric current has been applied. More specifically, experiments have been carried out in which the current is given by $I_{chirp}(t) = I_0(t)\sin(2\pi \cdot 10^{-5} t^3)$, where $I_0(t) = 9 \cdot 10^{-5} t^2$ and an additional saturation bound $|I_0(t)| \leq 7$ A holds. This so-called 'chirp' current has a slowly varying amplitude and frequency. The current specified above is used for a 500 s long experiment and after 279 s the amplitude sometimes saturates at ± 7 A. The resulting maximum chirp frequency is approximately 7.5 Hz. Two experiments which such chirp forcings have been carried out: one with a chirp current with increasing frequency, and another one where the instantaneous frequency decreases in time (inverse chirp current given by $I_{chirp}(t - 500)$). Both experiments show comparable phenomena.

In both the chirp experiments and the inverse chirp experiment, a vortex pattern appeared, as shown in fig. 2.4, with a different symmetry than in the former experiments. It is observed that the large $l = 5$ cm vortices are now aligning diagonally and, contrary to the pattern in fig. 2.1, only half of the domain is filled by these counter-clockwise rotating large vortices. Between the large vortices, small and weak clock-wise rotating vortices emerge. This new vortex pattern remains clearly visible for more than 10 s, during which time the large vortices keep rotating in the same direction.

The flow regime of the experiments can be characterised by two dimensionless parameters. The Reynolds number $Re = Ul/\nu$, characterising the ratio between advective and viscose forces, is typically of order $Re = 100$ for all experiments, as the mean velocity U is typically $U \approx 2 \cdot 10^{-3}$ m/s. This means that the nonlinear

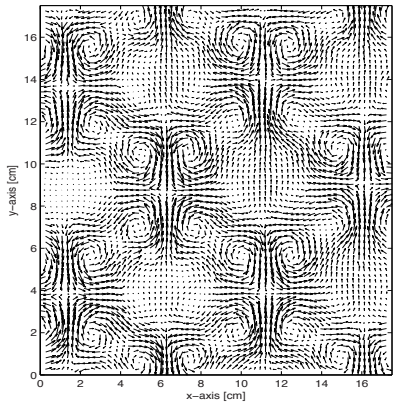

(a)

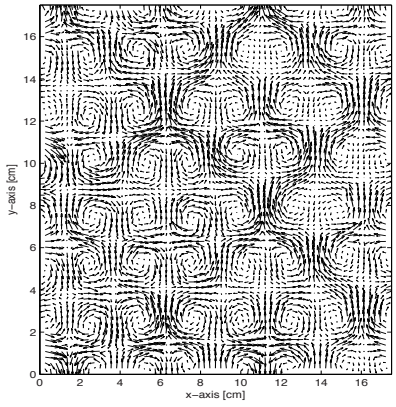

(b)

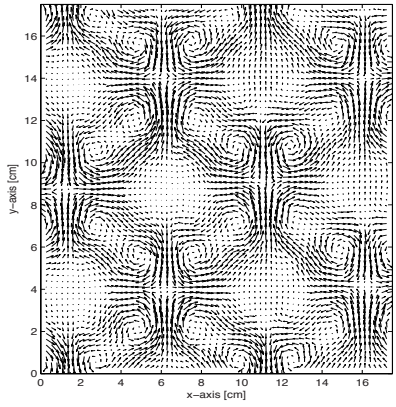

(c)

Figure 2.2: Velocity fields of an experiment with an alternating current according to $I = 5\sin(2\pi t)$ A. During one period (1 s) the velocity field evolves between the shown vortex patterns, *i.e.* according to the sequence a-b-c-b-a.

Figure 2.3: Snapshot of the streak line pattern corresponding to fig. 2.2(b).

effect of advection can not be neglected, but also that the flow is not turbulent. The relative importance of the forcing can be characterised by the Chandrasekhar number [18] $Ch = IBH/\rho\nu^2$, which varies for the different experiments. The experiment with $I = 20$ mA has $Ch = 1.5 \cdot 10^5$. But in both the periodic experiment, with $|I| = 5$ A, and the chirping experiment, with $\max(I) = 7$ A the forcing is significantly more dominant, as the Chandrasekhar number is higher, respectively $Ch = 3.0 \cdot 10^7$ and $Ch = 5.2 \cdot 10^7$.

2.5 Discussion

Flows in shallow fluid layers are often assumed to be quasi-two-dimensional and therefore governed by the 2D Navier Stokes equations. Recent work, however, shows that 3D effects can play a significant role in this type of flows [19]. Nevertheless, in the present study we assume vertical velocities inside the fluid layer as well as free surface deformations to be negligible and therefore consider the observed surface flow to be governed by the 2D Navier-Stokes equation for an incompressible fluid. Alternatively, we consider the vorticity-stream function formulation of the Navier-Stokes equation, which is given by

$$\frac{\partial \omega}{\partial t} + (\mathbf{v} \cdot \nabla)\,\omega = \nu \nabla^2 \omega - \kappa\omega + F_\omega, \tag{2.2a}$$

$$-\nabla^2 \psi = \omega, \tag{2.2b}$$

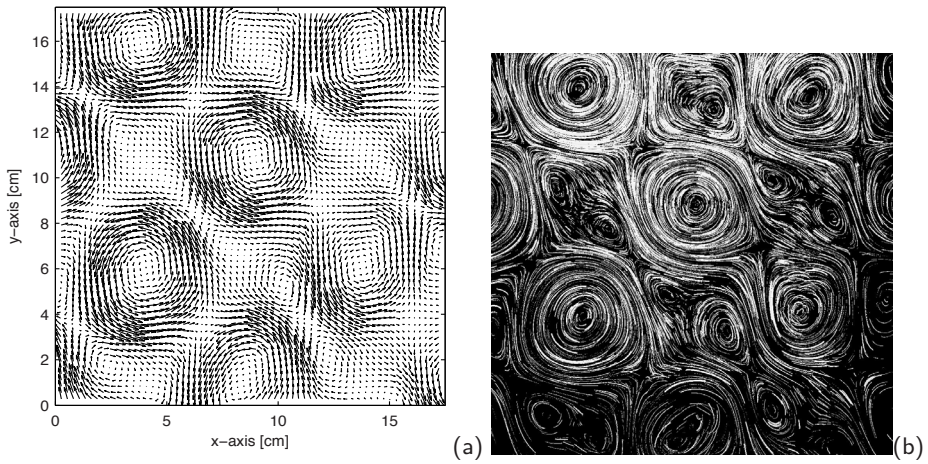

Figure 2.4: Velocity field (a) and streak-lines (b) of an experiment with an inverse chirp forcing. The vortex pattern contains both large (counter-clock wise rotating) and small vortices.

where ν is the kinematic viscosity and F_ω denotes the $z-$component of the curl of the body force acting upon the fluid. ψ is the stream function that is defined through $\mathbf{v} = \nabla\psi \times \nabla z$. Viscous dissipation due to bottom friction, which is the dominant dissipation mechanism for shallow flows above a no-slip bottom, can be modelled assuming a Poiseuille-like vertical profile for the horizontal flow field, resulting in the Rayleigh bottom friction term $\kappa\omega$, where $\kappa = \nu\pi^2/4H^2 = 0.038\,\mathrm{s}^{-1}$.

The recorded surface flows, depicted in figs. 2.1, 2.2 and 2.3, are now modelled as 2D Taylor-Green vortices [10] (extensive numerical simulations have been published in [20]), which are solutions of the eigenvalue problem $-\nabla^2\psi_{m,n} = \omega_{m,n} = \lambda_{m,n}\psi_{m,n}$ and $\psi_{m,n}$ (and consequently $\omega_{m,n}$ too) is assumed to vanish at the boundary of $L \times L$ domain. Due to the linear relationship between ω and ψ, the nonlinear advection term in (2.2a) cancels, thus rendering this equation linear and exactly solvable for an unforced flow with initial condition $\omega(x,y,t=0) = c\omega_{m,n}(x,y)$ by

$$\omega(x,y,t) = c\omega_{m,n}(x,y)e^{-(\nu\lambda_{m,n}+\kappa)t}, \tag{2.3}$$

where $\omega_{m,n}$ is given by

$$\omega_{m,n} = \sin(m\pi x/L)\sin(n\pi y/L) \tag{2.4}$$

and c is a constant.

For sufficiently small initial amplitudes c of these Taylor-Green vortices (*i.e.* for a small Reynolds number) this exponentially decaying solution (2.4) is stable for finite disturbances [12]. For larger initial amplitudes, the vorticity tends to evolve towards a big domain filling vortex, described by the first Taylor-Green vortex $\omega_{1,1}$ [15, 16].

In order to compare the experimentally observed vortex patterns with the Taylor-Green vortices, we consider the ratio between enstrophy and energy Ω/E, which plays an important role in the subsequent analysis. This ratio is minimised by the smallest eigenvalue of the eigenvalue problem mentioned before, *i.e.* $\lambda_{1,1} \leq \Omega/E$, and this minimum is achieved when $\omega = \omega_{1,1}$ [15, 16]. Moreover, by using Green's first identity one can prove that $\Omega/E = \lambda_{m,n}$ for every Taylor-Green vortex $\omega_{m,n}$ [15]. According to (2.4) this implies that patterns with smaller vortices dissipate faster.

In order to evaluate the adequacy of the Taylor-Green vortex patterns for describing the experimentally observed vortex patterns, we consider the 2D parameter space spanned by energy and enstrophy. In this parameter space a Taylor-Green vortex pattern given by $\omega_{m,n}$ is represented by a straight line with slope $\lambda_{m,n}$ through the origin (see fig. 2.5). The vortex pattern shown in fig. 2.1 and resulting from stationary (DC) forcing strongly resembles the Taylor-Green vortex pattern described by $\omega_{3,4}$, which also is a stationary solution to (2.2b) provided $F_\omega = F^{3,4} = c\sin(3\pi x/L)\sin(4\pi y/L)$ with an appropriate value of the constant c. This solution is stable for small forcing amplitude c and small Reynolds number [11], whereas bottom friction tends to increase the stability range [14]. The temporal evolution of the experimentally obtained ratio Ω/E has also been plotted in fig. 2.5 at discrete time instances. Obviously, for this experiment Ω/E is approximately constant in time and close to the theoretical value, which is given by $\lambda_{3,4} \approx 0.81$. Therefore it can be concluded that the applied stationary forcing stabilises the stationary Taylor-Green vortex $\omega_{3,4}$. Note however, that the forcing used in the experiments, as defined in (2.1), is strongly localised around the magnets and is really different from the type of forcing that is commonly used or assumed in studies [13, 21] and also different from the theoretical forcing $F^{3,4}$ mentioned before. Consequently, the formation of the vortex pattern is a more complex process [5, 8, 21] in which the advection term does play an essential role

and for which no analytical solution is known. However, in a steady state the vorticity advection term appears to be negligible, in view of the strong resemblance between the Taylor-Green solution $\omega_{3,4}$ and the experimentally observed vortex pattern.

The experiments with a periodic (AC) forcing resulted in vortex patterns that most of the time are akin to another Taylor-Green vortex $\omega_{7,7}$, see fig. 2.2 and fig. 2.3. Reasoning as in the previous paragraph suggests the periodic forcing $F_\omega = F^{7,7} = c\sin(2\pi ft)\sin(7\pi x/L)\sin(7\pi y/L)$, with $f = 1$ as a candidate forcing protocol for creating this pattern. However, there is one caveat: the periodic forcing $F^{7,7}$ leads to a solution of Eq. 2.2a that has the form $c_2\sin(2\pi ft-\phi)\omega_{7,7}$, with constants c_2 and ϕ. In this solution individual vortices periodically change their rotation direction, as opposed to the experimentally observed vortices in fig. 2.2 and fig. 2.3. Therefore the observed vortex pattern is essentially different from the one created by $F^{7,7}$ and there appears to be no obvious analytical solution similar to the observed vortex pattern. This is due to the strong localisation of the Lorentz force around the magnets, as this forcing does not resemble a pure Taylor-Green mode. Nevertheless, the relevance of $\omega_{7,7}$ for mimicking the experimentally observed vortex pattern for the AC forcing case becomes even more convincing when considering the temporal evolution of the experimentally obtained enstrophy and energy. As time progresses, the ratio of these two quantities commutes between two points in the parameter space shown in fig. 2.5 and in more detail in the zoom box. The states represented by figs. 2.2(a) and 2.2(c) both correspond to a point in the parameter space that is approximately given by $(E,\Omega) = (160, 280)$ whereas the vortex pattern shown in fig. 2.2(b) corresponds approximately to $(E,\Omega) = (55, 165)$, which is close to the theoretical eigenvalue $\lambda_{7,7} \approx 3.15$ associated with the Taylor-Green vortex pattern $\omega_{7,7}$. Since the time-averaged vortex pattern as defined by $\bar{\omega} = 1/T\int_0^T \omega dt$, where ω is the experimentally obtained vorticity, is approximately equal to $\omega_{7,7}$, see also fig. 2.2, we conclude that periodic (AC) forcing of the flow stabilises a Taylor-Green vortex pattern represented by $\omega_{7,7}$. This is a remarkable result in view of the fact that experimental realisation of such a pattern using stationary forcing (and adequate spacing of the magnets inside the domain $\mathcal{D}$) will only result in stable configurations for relatively weak forcing amplitudes, whereas in the periodic forcing case the pattern remains stable for much stronger forcing amplitudes.

The observed time-averaged stabilisation as a consequence of periodic forcing appears similar to results in the field of vibrational control. This field is based

on the observation that unstable nonlinear equilibria can under certain conditions be approximately stabilised (time-averaged) by using a high-frequency oscillatory forcing, with a small amplitude. A well-known example is the inverted pendulum, which can be stabilised in upwards position by vertically exciting the bearing of the pendulum at a high frequency [22]. Vibrational control can also stabilise flows, *e.g.* Rayleigh-Taylor and Bénard instabilities, see [23] and references therein. However, in our experiments stabilisation occurred for a certain moderate frequency range of the forcing and it is unlikely to work for high frequencies with small amplitudes. Therefore it is not clear yet whether the observed stabilisation is caused by the same mechanism seen in vibrational control.

In the last set of experiments, a chirp forcing was applied. Figure 2.4 shows that this results temporally in a flow with the same length scale as in the stationary forced experiment. There is, however, an important difference: the counter-clockwise rotating vortices are larger and stronger than the clockwise rotating ones. An explanation for this phenomenon is not available yet, but this experiment shows that time-varying forcing can cause particular self-organisation in shallow-water-layer flows. In fig. 2.5 we have plotted the temporal evolution of the enstrophy and energy for the (inverse) chirp experiment. As time progresses we observe that these two quantities evolve along a straight line. The slope of this line is 0.85, which is close to the slope of the line corresponding to the Taylor-Green vortex pattern $\omega_{3,4}$.

2.6 Conclusions and recommendations

Forced Q2D free-surface flows in a shallow fluid layer have been studied experimentally for three different forcing protocols. These forcing protocols are all spatially periodic but each of them has a different time dependence. The temporal evolution of the energy and enstrophy of the free-surface flows has been evaluated in order to compare the resulting flow topology with the so-called Taylor-Green vortex patterns, which constitute a family of unstable exact solutions of the 2D Navier-Stokes equation.

For stationary forcing we observe a regular and stationary vortex pattern that is very similar to a 2D Taylor-Green vortex pattern. Time-periodic forcing results in stable but oscillating vortex patterns with vortices having a smaller size than the length scale of the forcing. Averaged in time, these patterns are also similar to a Taylor-Green vortex, yet different from the one observed for stationary

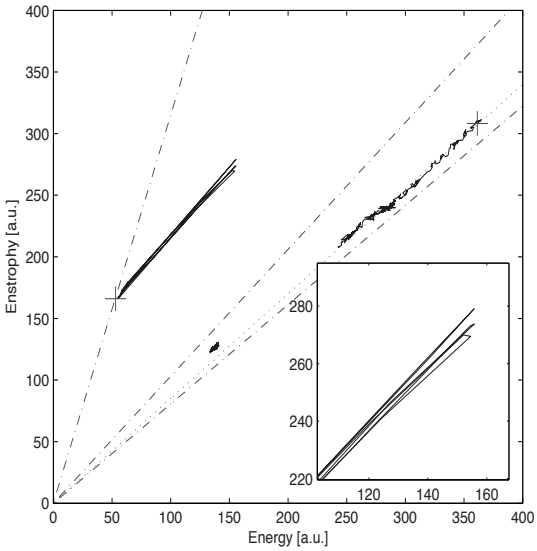

Figure 2.5: The experimental E, Ω evolution. The slope of the three dashdotted lines equals the eigenvalues $\lambda_{3,4} = 0.81$, $\lambda_{4,4} = 1.03$ and $\lambda_{7,7} = 3.15$, in increasing order. The dashed line has a slope of 0.85 and the inverse chirp experiment (starts at the plus symbol) evolves on this diagonal. The point cloud, around $E = 140, \Omega = 120$, corresponds to the stationary $20\ \mathrm{mA}$ experiment. The solid line at $E = 150, \Omega = 250$ corresponds to several periods of the periodically forced experiment. The zoom box indicates that, for a time-periodic forcing, E and Ω are not monotonously decreasing but oscillating between $(E, \Omega) \approx (160, 280)$ and $(E, \Omega) \approx (55, 165)$. All experimental data is plotted blue in online version.

forcing. This vortex pattern is remarkably stable, even for relatively strong forcing amplitudes, suggesting that this intrinsically unstable vortex pattern is stabilised when using time-periodic forcing. Finally, forcing the flow in an aperiodic way (chirp forcing) also shows the emergence of regular vortex patterns with length scales comparable to the ones observed for stationary forcing. However, contrary to the time-periodically forced case, this pattern appeared to be quasi-stationary instead of periodic. Moreover, as the symmetry of this pattern is different from the other patterns and different from the forcing, the chirp forcing appears to induce temporary self-organisation of the vortices. All experimentally observed flow patterns were analysed in the enstrophy-energy parameter space. It was found that the framework of Taylor-Green vortices is very well suited for analysing these forced vortex patterns at relatively low Reynolds numbers.

Forcing of Q2D flows with spatially periodic but time dependent body forces seems not to have been studied before, neither analytically nor experimentally. The observations presented here show for the first time that time-varying (spatially periodic) forcing can produce approximately stable (time-averaged) vortex patterns that are intrinsically unstable when unforced, analogous to vibrational control [22].

It should be noted that the experiments reported are exploratory and suggest further studies. Although the stabilisation of otherwise unstable vortex patterns by time dependent forcing and their relation to Taylor-Green vortices has been demonstrated in principle, the mechanisms at work here are far from being understood. As a first step towards understanding, their relation to Taylor-Green vortices has been shown here. Any future work therefore needs to address in more detail the relationship between the stability of such vortex patterns and their energy and enstrophy evolution to the time-varying forcing. An up-to-date framework for studying this relationship is currently missing.

We also observe that the 3D Taylor-Green vortices [24] are often used to study blow-up of the Navier-Stokes and Euler equations [25] and to study dynamo action [26]. It is an open problem whether phenomena similar to the ones observed in this work can appear in the fully 3D situation. But if they do, this might be relevant for the study of the mentioned problems.

Bibliography

[1] McWilliams J.C. *J. Fluid Mech.,* **146** (1984) 21.

[2] Clercx H.J.H. and van Heijst G.J.F., *Appl. Mech. Rev.,* **62** (2009) 1.

[3] Tabeling P., *Phys. Rep.,* **362** (2002) 1.

[4] Boffetta G. and Ecke R.E., *Annu. Rev. Fluid Mech.,* **44** (2011) 427.

[5] Sommeria J., *J. Fluid Mech.,* **170** (1986) 139.

[6] Cardoso O., Marteau D., Tabeling P., *Phys. Rev. E,* **49** (1994) 454.

[7] Marteau D., Cardoso O., Tabeling P., *Phys. Rev. E,* **51** (1995) 5124.

[8] Cieślik A.R., Kamp L.P.J., Clercx H.J.H., van Heijst G.J.F., *Europhys. Lett.,* **85** (2009) 54001.

[9] Chen Z.-M. and Price W.G., *Commun. Math. Phys.,* **179** (1996) 577.

[10] Taylor G.I., *Philos. Mag.* **46** (1923) 671.

[11] Gotoh K. and Yamada M., *J. Phys. Soc. Jpn.,* **53** (1984) 3395.

[12] Lin S.P. and Tobak M., *Phys. Fluids,* **30** (1987) 605.

[13] Thess A., *Phys. Fluids A,* **4** (1992) 1396.

[14] Murakami Y., Fukuta H., Gotoh K., in *Nonlinear instability of nonparallel flows,* edited by Lin S.P., Phillips W.R.C., and Valentine D.T. (Springer, Berlin) 1994, pp. 320-329.

[15] van Groesen E., *Physica A,* **148** (1988) 312.

[16] van Groesen E., in *Structure, coherence and chaos in dynamical systems,* edited by Parmentier R.D. and Christiansen P.L. (Manchester University Press, Manchester) 1989, pp. 481-484.

[17] Raffel M., Willert C.E., Wereley S.T., Kompenhans J., *Particle image velocimetry : a practical guide* (Springer, Berlin) 2007.

[18] Duran-Matute M., Trieling R.R., van Heijst G.J.F., *Phys. Rev. E,* **83** (2011) 016306.

[19] Akkermans R.A.D., Kamp L.P.J., Clercx H.J.H., van Heijst G.J.F., *Europhys. Lett.,* **83** (2008) 1.

[20] Valentine D.T, *Int. J. Numer. Meth. Fl.,* **21** (1995) 155.

[21] Sommeria J. and Verron J., *Physics of Fluids,* **27** (1984) 1918.

[22] Meerkov S.M., *IEEE T. Automat. Contr.,* **25** (1980) 755.

[23] Meerkov S.M., *J. Math. Anal. Appl.,* **98** (1984) 408.

[24] Taylor G. I. and Green A. E., *Proc. R. Soc. Lond. A,* **158** (1937) 499.

[25] Brachet M.E., Meiron D.I., Orszag S.A., Nickel G.G., Morf R.H., Frisch U., *J. Fluid Mech.,* **130** (1983) 411.

[26] Nore C., Brachet M.E., Politano H., Pouquet A., *Phys. Plasma,* **4** (1997) 1.

Chapter 3

Mapping matrix structure and mixing

M.F.M. Speetjens, M. Lauret, H. Nijmeijer, P.D. Anderson[1]

3.1 Abstract

Transport of passive tracers may be described through the spatio-temporal evolution of Eulerian concentration distributions or via the geometrical composition of the Lagrangian flow structure. The present study seeks to deepen insight into the connection between the Eulerian and Lagrangian perspectives by investigating the role of Lagrangian coherent structures (LCSs) in the Eulerian concentration distributions in time-periodic and spatially-periodic mixing flows. Representation of the Eulerian transport by the mapping method, describing realistic transport problems by distribution matrices, admits a generic analysis based on matrix and graph theory. This reveals that LCSs – and the transport barriers that separate them – leave a distinct "footprint" in the eigenmode spectrum of the distribution matrix and, by proxy, of the underlying Eulerian transport operator.

Transport barriers impart a block-diagonal structure upon the mapping matrix, where each block matrix A corresponds with a given LCS. Its kind is reflected in the spectrum of A; higher-order periodicity yields a distinct permutation within A.

The composition of the distribution matrix versus the Lagrangian flow structure thus predicted is demonstrated by way of examples. These findings increase

[1]This chapter is based on 'Footprints of Lagrangian flow structures in Eulerian concentration distributions in periodic mixing flows', as has been published in Physica D 250, 2013, pp. 20-33.

fundamental understanding of transport phenomena and have great practical potential for e.g. flow and mixing control.

3.2 Introduction

Understanding the relation between flow and effective mixing of scalars (chemical species, heat, nutrients) is important for many processes in industry and Nature [1, 2, 3, 4, 5]. Accomplishment of efficient mixing in low-Reynolds number flows by way of chaotic advection has been a research topic since the early 1980s [6, 7, 8] and attracted renewed interest over the last decade or so with the emergence of compact and micro-scale fluid-processing devices for a wide range of applications [9, 10, 11, 12, 13, 14, 15, 16]. Great fundamental insight into the workings of chaotic advection has been attained by analysis of the advection of passive tracers ("distributive mixing")[2] adopting Lagrangian concepts from dynamical-systems theory (critical points, transport barriers, manifolds *etc*) [8, 7, 17, 4]. Key to this ansatz is the fundamental property that continuity organizes the trajectories of passive tracers into coherent structures – termed "Lagrangian coherent structures" (LCSs) hereafter – that geometrically determine the advection characteristics.[3] The set of finest LCSs that constitute the Lagrangian flow structure is the so-called ergodic partition [19, 20]. Well-known examples of LCSs are elliptic islands and chaotic seas in two-dimensional (2D) time-periodic flows and cross-sections of three-dimensional (3D) steady spatially-periodic flows. The present study is restricted to these important flow classes.

An alternative approach towards transport and mixing consists of an Eulerian representation based on the spatio-temporal evolution of the scalar field, which is determined by the eigenmodes of the transport operator. Eigenmode analyses on transport operators have to date been performed primarily in the scope of advective-diffusive scalar transport and advanced insightful concepts as dominant

[2] Diffusive and distributive mixing refer to scalar transport with and without diffusion, respectively, within the scope of this study. This is common yet not exclusive terminology. Absence of diffusion means that an initial state is merely redistributed by the fluid motion while initial quantities are conserved by each fluid parcel. Fluid parcels thus carrying a scalar quantity are denoted "passive tracers" here.

[3] Important to note is that the term "Lagrangian coherent structures" (LCSs) in the present context refers to invariant material structures in the fluid trajectories; LCSs in literature typically denote surfaces that are demarcated on the basis of (finite-time) Lyapunov exponents. The relation between both kinds of LCSs is non-trivial and remains unsettled [18].

(or "strange") eigenmodes that govern the scalar evolution [21, 22, 23]. An important issue is the role of (chaotic) advection in the spectral properties of the advection-diffusion operator. Insight into this connection is imperative for control strategies employing the flow forcing, which is typically the only degree of freedom in a given system, for regulation of the transport process. This has particular potential for micro-fluidic applications, where promising flow-forcing methods as e.g. artificial cilia, magnetic forcing and AC electro-osmosis afford many ways to manipulate the flow [24, 25, 26, 27]. Better control of flows and associated LCSs may, besides mixing enhancement, enable systematic creation of distinct concentration distributions or Lagrangian flow structures for e.g. (local) catalysation of chemical reactions in labs-on-a-chip or manufacturing of anisotropic micro-fibres.

In its advective limit, the eigenmodes of the advection-diffusion operator are intimately related to the Lagrangian flow structure [28, 29]. This implies that LCSs, at least in said limit, leave distinct footprints in the Eulerian transport by determining the eigenmodes of the transport operator [19, 20]. Scope of the current investigation is formation of such footprints in the aforementioned classes of periodic flows. To this end the advection operator is represented by a distribution matrix according to the mapping method so as to attain a universal description that is amenable to efficient numerical treatment [30, 31, 32, 33]. This facilitates rigorous analyses using graph and matrix theory and, with flow control a potential application of knowledge gathered, already sets the stage for future links with control theory. Singh *et al.* [34] first embarked on this course and exposed a number of fundamental connections between the eigenmode decomposition of the mapping matrix and LCSs. The present study expands on this by further unravelling the connections between Eulerian and Lagrangian transport properties using the mapping method. This reveals that transport barriers separating LCSs impose a (hidden) block-diagonal structure upon the mapping matrix. Each LCS corresponds with a block matrix A and manifests its character in the spectral properties. Higher-order periodicity within an LCS (e.g. island chains) yields a distinct permutation within A.

The paper is organized as follows. Section 3.3 introduces the mapping method for distributive mixing and recapitulates first connections between its distribution matrix and LCSs found in previous work. Section 3.4 expands on this by establishing a rigorous link between the composition of said matrix and two key LCSs, viz. elliptic islands and chaotic seas, by way of an in-depth analysis hinging on graph

and matrix theory. The impact of numerical effects on this link is investigated in Section 3.5. Conclusions are in Section 3.7.

3.3 Distributive mixing in periodic flows

3.3.1 Introduction

The present study concerns 2D time-periodic flows and 3D steady spatially-periodic flows. Both flow types essentially have the same structure and admit a representation by 2D time-periodic flows without loss of generality [34]. Advective-diffusive transport of a passive scalar quantity $c(x,t)$ by a time-periodic flow $u(x,t) = u(x,t+T)$, with period time T and subject to solenoidality $\nabla \cdot u = 0$, in the generic 2D domain $\mathcal{D}$ is governed by

$$\frac{\partial c}{\partial t} = -u \cdot \nabla c + \frac{1}{\mathrm{Pe}} \nabla^2 c \quad c(x,0) = c_0(x), \tag{3.1}$$

completed by boundary conditions defined on boundary $\partial\mathcal{D}$. Here $\mathrm{Pe} = UL/\kappa$ is the Péclet number, with U and L the characteristic velocity and length scale respectively and where κ is the mass-diffusion coefficient [35]. Distributive mixing (i.e. advective transport by fluid motion only) occurs in case diffusion is absent and corresponds with the limit $\mathrm{Pe} \to \infty$.

Periodic scalar transport can be described by the Floquet operator $\mathcal{F}$, which maps the scalar distribution between discrete time levels $t = nT$, where $n \in \mathbb{N}$ a positive integer, via

$$c(x,T) = \mathcal{F}\left(c(x,0)\right) \quad c(x,(n+1)T) = \mathcal{F}\left(c(x,nT)\right) \quad c(x,nT) = \mathcal{F}^n\left(c_0(x)\right) \tag{3.2}$$

and thus incorporates the integral effect of the advection-diffusion operator within one period.[4] The Floquet operator permits the eigenmode decomposition

$$c(x,nT) = \sum_{k=0}^{\infty} \gamma_k \mathcal{H}_k^{(n)}(x) \quad \mathcal{H}_k^{(n)}(x) = \nu_k^n \Theta_k(x), \tag{3.3}$$

with $\mathcal{H}_k^{(n)}$ the eigenmodes and $\{\Theta_k, \nu_k\}$ the corresponding eigenfunction-eigenvalue pairs governed by the eigenvalue problem $\mathcal{F}(\Theta_k) - \nu_k \Theta_k = 0$ and coefficients γ_k determined by the initial state [36, 34]. For distributive mixing ($\mathrm{Pe} \to \infty$) the scalar

[4] Term "Floquet operator" refers specifically to time-periodic systems; the transport operator is for generic time-dependence commonly denoted "Frobenius-Perron operator" [23].

c becomes a passive tracer (i.e. a "label" for fluid parcels due to $\partial c/\partial t + u \cdot \nabla c = dc/dt = 0$) and the Floquet operator in essence describes the period-wise mapping of tracer positions following

$$\mathcal{F} : x_n \to x_{n+1} \quad x_n = x(nT), \tag{3.4}$$

and thus effectively coincides with the flow $x_{n+1} = F(x_n)$ governed by the Lagrangian equations of motion $dx/dt = u$. This has the fundamental ramification that in the limit $\mathrm{Pe} \to \infty$ the scalar transport properties become inextricably linked with Lagrangian coherent structures (LCSs) that form in the web of fluid trajectories by virtue of continuity. Important to note is that the mapping representation of the transport operator introduced hereafter, though strictly concerning purely advective transport, introduces diffusion-like behavior to the dynamics that closely resembles molecular diffusion at very high Pe [37]. The present study demonstrates that this is inconsequential in the sense that the abovementioned link with LCSs remains sufficiently intact, however. Moreover, this slight diffusion, though of numerical origin, is in fact physically meaningful in the sense that at some length scale molecular diffusion invariably comes into play in a real flow.

An illustrative example of transport in 2D time-periodic flows is found in the time-periodic sine flow (TPSF) on the 2-torus $(x,y) \in [0,1] \times [0,1]$ [36, 34]. The TPSF consists of periodic reorientation of steady velocity fields: $u = (\sin(2\pi y), 0)$ for $0 < t < T/2$ and $u = (0, \sin(2\pi x))$ for $T/2 < t < T$. The TPSF admits an analytical solution to the Lagrangian equations of motion and thus enables highly-accurate visualisation of its Lagrangian flow structure by Poincaré sections. Figure 3.1 gives the latter for $T = 0.56, T = 0.8$ and $T = 1.6$, exposing the characteristic flow structure of 2D mixing flows: islands and chaotic seas. The progression with growing T reveals a gradual diminution of islands in favor of a chaotic sea until a state of global chaos sets in beyond a certain T.

Islands consist of concentric closed invariant curves, that is, the well-known KAM tori [7, 38]. They act as as transport barriers to scalar redistribution and the outermost KAM torus of an island physically separates its interior from the surrounding chaotic sea. Perturbation typically causes disintegration of islands into smaller islands and encircling "island chains" embedded in chaotic "bands" following the KAM and Poincaré-Birkhoff theorems [7, 38]. However, the outermost KAM torus of each island remains a strict transport barrier. KAM tori on the brink of disintegration typically develop leaks, a state referred to as "cantorus,"

and thus form an intricate local Lagrangian flow structure that partially acts as a transport barrier and partially facilitates weak dispersion of material across the (originally complete) KAM torus [39, 40]. Islands and chaotic seas are two key features of the Lagrangian flow structure (or ergodic partition) of periodic flows and the primary subjects of investigation hereafter.

The organization into islands and seas in fact stems from periodic points, i.e. material points that systematically return to their initial position after a given number of periods p, defined by $x^{(0)} = F^p(x^{(0)})$. Incompressible 2D time-periodic flows admit two non-degenerate types: elliptic and hyperbolic periodic points. Former and latter locally organize the tracer paths into islands and chaotic seas, respectively. LCSs within chaotic seas are the stable and unstable manifolds associated with each hyperbolic point; these manifolds accomplish the characteristic exponential stretching and folding of fluid parcels that underlies chaotic advection [7, 38]. Periodic points – and accompanying LCSs – may emerge isolated (periodicity $p=1$) or in clusters (periodicity $p>1$) of p points $\mathcal{X} = \left\{x^{(0)}, x^{(1)}, \ldots, x^{(m)}, \ldots, x^{(p-1)}\right\}$, with $x^{(0)} = F^p(x^{(0)})$ and $x^{(n)} = F^n(x^{(0)})$ [41, 42]. Essential is that material wanders progressively through the consecutive elements yet clusters as a whole are invariant. Island chains e.g. encompass p islands that each are centered on one of the points belonging to a cluster of p elliptic period-p points; chaotic seas may originate from manifolds of clusters of higher-order periodic points. Here islands for $T = 0.56$ and $T = 0.8$ correspond with two isolated period-1 and two clusters of period-2 points, respectively. The pair-wise emergence is in both cases a manifestation of the time-reversal symmetry $F = SF^{-1}S$, with $S : (x, y) \to (y, 1-x)$, by which LCSs $\mathcal{C}$ emerge in symmetry groups $(\mathcal{C}, S(\mathcal{C}))$ [42].

Shown Lagrangian flow structure is intimately related to the eigenmodes $\mathcal{H}_k^{(n)}$ of the underlying transport operator [28, 29]. Hence, an eigenmode analyses of this operator is expected to provide fundamental insight into the transport properties of distributive mixing. An efficient and flexible way to carry out eigenmode analyses is by way of the mapping method, which enables a discrete approximation of the Floquet operator in a wide range of flow situations by so-called mapping matrices. The composition of these matrices, notwithstanding weak diffusion-like effects inherent in the discretisation, relates directly to the LCSs and thus reflects the link between Eulerian and Lagrangian transport properties of a given flow. First connections between this matrix composition and LCSs have been established in Singh *et al.* [34]. The study hereafter further elaborates this.

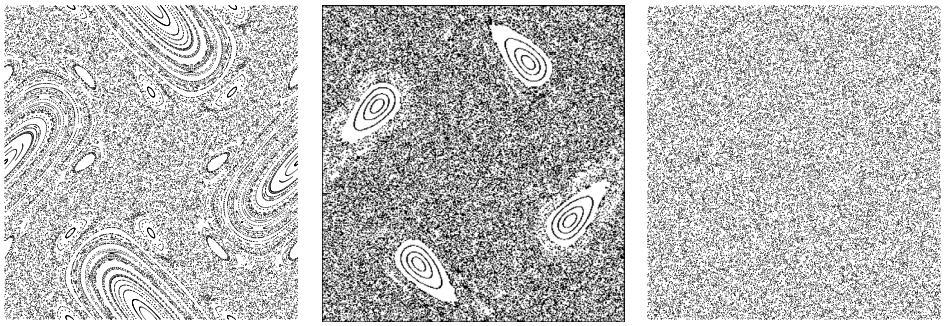

Figure 3.1: Typical 2D Lagrangian flow structure illustrated by way of the Poincaré section of the TPSF for various T: (a) $T = 0.56$; (b) $T = 0.8$; (c) $T = 1.6$.

3.3.2 Distributive mixing and the cell-mapping method

The cell-mapping method, originally proposed by Spencer and Wiley [43], describes mixing within each period by the redistribution of scalar quantities $c(x,t)$ over a discrete grid of N cells. This redistribution is area-preserving for solenoidal flow fields $\nabla \cdot u = 0$, meaning that in the present limit of distributive mixing a given amount of material is proportional to the area of the material fluid element it occupies. This renders the scalar redistribution equivalent to the redistribution of initial areas A_j of each cell Ω_j over all cells of the mapping mesh. The entries of the mapping matrix Ξ describing this redistribution are then given by

$$\Xi_{ij} = \frac{A_{ij}}{A_j}, \tag{3.5}$$

and represent the portion A_{ij} of the area of cell Ω_j (with area A_j) received by cell Ω_i. Normalization by donor cell size and uniform cell sizes (typical situation) implies real entries $\Xi_{ij} \in [0,1]$. This area-based mapping method is illustrated schematically in Figure 3.2(a).

Principal drawback of the above ansatz is that it entails tracking of continuous interfaces of material elements and determination of intersections of advected areas and cells, which is computationally expensive on account of the strong deformation of material elements in the course of the mixing process. A computationally more efficient way to evaluate the mapping matrix is by representation of the continuous material within cells by K discrete particles, as illustrated in Figure 3.2(b) [44]. The entries of the mapping matrix Φ describing the period-wise particle

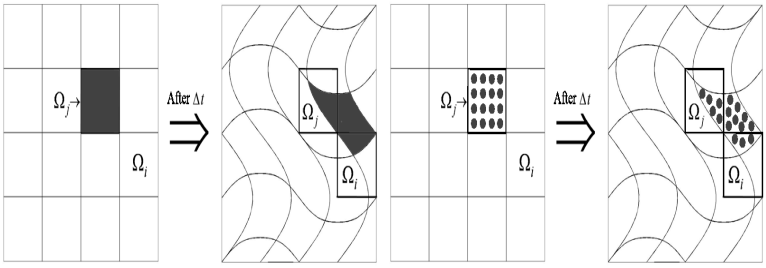

Figure 3.2: Computation of the mapping matrix from redistribution of material over a grid of finite mapping cells: (a) continuous (area-based) approach; (b) discrete (particle-based) approach.

redistribution over the cells are given by

$$\Phi_{ij} = \frac{M_{ij}}{M_j}, \tag{3.6}$$

with M_{ij} the number of the total amount of particles released in cell Ω_j and received by cell Ω_i. Here normalization takes place by the total number of particles M_j released in the donor cell Ω_j. Thus particle amount M in (3.6) is entirely analogous to area A in the approach following (3.5). Entries are rational and, as before, restricted to the interval $\Phi_{ij} \in [0,1]$.

The mapping matrices Ξ and Φ admit computation of the transport of arbitrary initial distributions $c_0 \in R^{N\times 1}$ (or its discrete-particle representation) during each period via $c_1 = \Xi c_0$ (or $c_1 = \Phi c_0$), with $c_1 \in R^{N\times 1}$ the state after one period. This, in turn, facilitates efficient period-wise progression of initial states c_0 by repetitive mapping following

$$c_n = (\underbrace{\Xi(\Xi(...(\Xi}_{\text{n times}} c_0)...) = \Xi^n c_0 \qquad \Leftrightarrow \qquad c_n = \Phi^n c_0, \tag{3.7}$$

with c_n the resulting distribution after n periods.

The above mapping approaches introduce departures from the continuous transport form (3.1). The finite cell size leaves sub-cell flow features unresolved. This manifests itself in "smearing-out" of distributions c_n over length scales comparable to the cell size in a diffusion-like manner. This "numerical diffusion" occurs for both Ξ and Φ and diminishes with decreasing cell sizes, meaning it becomes insignificant for sufficiently large N. A further issue concerns mass conservation. Mapping matrix Ξ has column sums ($\sigma_j^c = \sum_i \Xi_{ij}$) as well as row

sums ($\sigma_i^r = \sum_j \Xi_{ij}$) equal to unity (i.e. $\sigma_j^c = 1$ and $\sigma_i^r = 1$ for all $i, j \in [1, N]$). This signifies compliance with mass conservation by individual cells. Moreover, $\sum_{i=1}^{N} \sigma_i^r = \sum_{j=1}^{N} \sigma_j^c = N$ implies global mass conservation. Mapping matrix Φ, on the other hand, only has column sums equal to unity ($\sigma_j^c = 1$); row sums typically yield $\sigma_i^r \neq 1$ yet nonetheless meet $\sum_{i=1}^{N} \sigma_i^r = \sum_{j=1}^{N} \sigma_j^c = N$. Thus Φ preserves mass only on a global level in that the *total* mass within the system remains constant while cell-wise mass contents may vary over time. (Physically, this is comparable to the presence of local sources and sinks that leave the total mass content unaffected.) Satisfaction of local mass conservation improves with growing K and becomes identical in the limit $K \to \infty$.

Two relevant cases must be distinguished concerning numerical diffusion and local violation of mass conservation: conformal and non-conformal mapping grids. Conformal mapping grids consist of cells that align with the transport barriers separating elliptic islands and chaotic seas (i.e. the outermost KAM tori of islands). Corresponding mapping matrices preserve the physical separation of these LCSs and, in consequence, numerical effects are confined to internal transport within individual islands or chaotic seas. Non-conformal mapping grids, on the other hand, include cells that may cross the transport barriers and thus effectively "smear" the latter out into "fuzzy" boundaries, admitting manifestation of numerical diffusion on a global level.[5]

Finite departures from local mass conservation, inherent in the particle-based representation (Section 3.3.2), manifest themselves in local non-conservative behaviour in a source-sink like manner and thus eradicate the Hamiltonian mechanisms that underly formation of LCSs in solenoidal flows [7, 38]. This has *grosso modo* the same impact on the correlation between true LCSs and their representation by the mapping matrix as numerical diffusion.

[5] Realistic transport barriers are typically continuous and, in exceptional cases, may even be incomplete (e.g. cantori). These properties can not be exactly represented by finite cells. This rules out truly conformal mapping grids and implies that a certain degree of non-conformity is *always* present. This is considered negligible here for conceptual purposes, however. Note that mapping grids typically are non-conformal.

3.3.3 Eigenmode decomposition of the mapping matrix

The mapping matrices Ξ and Φ constitute discrete approximations of the continuous Floquet operator $\mathcal{F}$ following (3.2) and admit representation as

$$\Phi = \sum_{k=1}^{N} \lambda_k v_k v_k, \qquad \Xi = \sum_{k=1}^{N} \lambda'_k v'_k v'_k \tag{3.8}$$

with $\{v_k, \lambda_k\}$ and $\{v'_k, \lambda'_k\}$ the corresponding eigenvector-eigenvalue pairs. Substitution of this form in mapping (3.7) yields

$$c_n = \Phi^n c_0 = \sum_{k=1}^{N} \widetilde{c}_k^0 h_k^{(n)} \quad h_k^{(n)} = \lambda_k^n v_k \quad c_0 = \sum_{k=1}^{N} \widetilde{c}_k^0 v_k, \tag{3.9}$$

as discrete approximation of the continuous eigenmode decomposition (3.3) by the particle-based matrix Φ. Here eigenvector-eigenvalue pairs $\{v_k, \lambda_k\}$ and eigenmodes $h_k^{(n)}$ are discrete counterparts to the eigenfunction-eigenvalue pairs $\{\Theta_k, \nu_k\}$ of the Floquet operator and the eigenmodes $\mathcal{H}_k^{(n)}$ in (3.3), respectively. The expansion coefficients $\widetilde{c}_k^0$, similar to coefficients γ_k in (3.3), are determined by the initial state c_0. The corresponding eigenmode representation for Ξ is analogous and not shown for brevity.

Purely advective transport strictly confines the eigenvalue spectrum to the unit circle, i.e. $|\lambda_k| = 1$ for all k, implying a unitary mapping matrix [28, 29]. However, this condition is fulfilled only in the hypothetical case of infinite spatial resolution, or equivalently, a conformal mapping grid perfectly coinciding with the ergodic partition of the Lagrangian flow structure. Actual mapping matrices suffer from numerical diffusion due to finite cell sizes, resulting in local smearing-out of spatial features (Section 3.3.2). This, in turn, causes the spectrum to (partially) fall within the unit circle in a similar manner as for Floquet operators with finite Pe [44]. The eigenmodes of the actual mapping matrix nonetheless are physically meaningful in that they constitute slightly "fuzzied" representations of the eigenmodes of the ideal unitary mapping matrix. Moreover, the diffusion-like behavour in fact adequately represents the weak yet inevitable molecular diffusion in any real flow (Section 3.3.1)

The study by Singh *et al.* [34] revealed that the properties of the eigenmodes of Φ correlate with the LCSs formed by fluid trajectories and has been exemplified in Section 3.3.1 by way of the TPSF. The key findings have been condensed in the following conjectures:

Conjecture 1 *Elliptic islands relate to eigenmodes with* $|\lambda_k| = 1$.

Conjecture 2 *Chaotic seas have eigenmodes with* $|\lambda_k| < 1$.

Conjecture 3 *Eigenmodes of elliptic islands and chaotic seas are spatially disconnected.*

Conjecture 4 *Period-p structures of equal kind correspond with clusters of eigenvalues* $\left\{\lambda^{(0)}, \lambda^{(1)}, \ldots, \lambda^{(m)}, \ldots, \lambda^{(p-1)}\right\}$, *with* $\lambda^{(m)} = |\lambda|\omega^m$ *and* $\omega = e^{\frac{2\pi i}{p}}$.

Conjecture 5 *The eigenvectors corresponding with eigenvalues as per Conjecture 4 combined demarcate the invariant region occupied by the entire period-p group.*

Note that the original statement of Conjecture 5 following [34] has been reformulated here yet with retention of its meaning. These conjectures imply that eigenmodes, apart from the trivial eigenmode, always group into the following three categories:

1. persistent eigenmodes ($|\lambda_k| = 1$) associated with elliptic islands;
2. decaying eigenmodes ($|\lambda_k| < 1$) associated with elliptic islands;
3. decaying eigenmodes ($|\lambda_k| < 1$) associated with chaotic seas.

Eigenvalues $|\lambda_k| \leq 1$ invariably cause progression of any initial state to an asymptotic state determined by the persistent eigenmodes. The decaying eigenmodes dictate the transient towards that state; their exponential decay in magnitude means that (local) transients rapidly become dominated by the slowest-decaying eigenmode in a given region, that is, the decaying eigenmode with the highest $|\lambda_k| < 1$ ("dominant eigenmode") [34]. Figure 3.3 shows typical examples of the above kinds of eigenmodes for the TPSF at $T = 0.8$. The eigenmodes associated with elliptic islands and chaotic sea (panels (a)-(c)) are evidently non-zero only within these LCSs (compare with the Poincaré section in Figure 3.1(b)).

The above categorisation of eigenmodes – and the underlying Conjectures 1-5 – pertains specifically to conformal mapping grids. The stringent separation between LCSs means that inhomogeneous concentration distributions due to entrapment of material within elliptic islands are maintained indefinitely. This implies the above persistent eigenmodes. The accompanying decaying eigenmodes emanate from

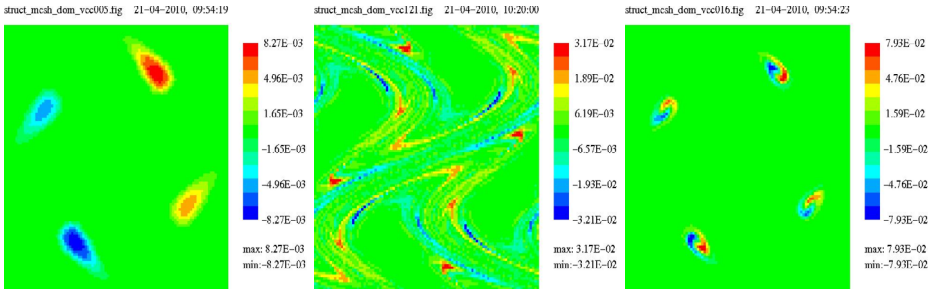

Figure 3.3: Three kinds of eigenmodes in the mapping matrix Φ demonstrated for the TPSF ($T = 0.8$): (a) persistent eigenmode of elliptic islands; (b) decaying eigenmode of chaotic sea; (c) decaying eigenmode of elliptic islands.

localized smearing-out due to non-conformity of the mapping grid with internal KAM tori. Emergence of only decaying eigenmodes in the chaotic seas stems from the fact that here spatial features are infinitely small and of great geometrical complexity, leading to non-conformity – and smearing-out – throughout the *entire* region. Non-conformal grids introduce small departures from this scenario in that *all* eigenvalues, save the trivial eigenmode associated with total mass conservation, move inside the unit circle. However, this effect is marginal for sufficient (yet feasible) spatial resolutions, meaning that the above properties are retained to a high degree of accuracy [44]. The close agreement between the eigenmodes in Figure 3.3, obtained by a non-conformal mapping grid, and the corresponding Poincaré sections is testament to this. Furthermore, recall from the previous that the numerical diffusion underlying this localized smearing-out in fact represents a physically-meaningful phenomenon.

The particular association between LCSs and eigenmodes for conformal grids fundamentally determines its composition. This is explored in Section 3.4. Changes in this composition brought on by employing non-conformal mapping grids are discussed in Section 3.5.

3.4 Composition of the mapping matrix for conformal grids

3.4.1 Introduction

The distinction of three fundamental kinds of eigenmodes for mapping matrices built with conformal grids implies a generic decomposition into three invariant eigenspaces following

$$\Phi = \sum_{k\in\mathcal{K}_1} \lambda_k^{(1)} v_k^{(1)} v_k^{(1)} + \sum_{k\in\mathcal{K}_2} \lambda_k^{(2)} v_k^{(2)} v_k^{(2)} + \sum_{k\in\mathcal{K}_3} \lambda_k^{(3)} v_k^{(3)} v_k^{(3)}, \tag{3.10}$$

with superscripts referring to the categories introduced before and $\mathcal{K}_i$ the corresponding subspectrum, where $\mathcal{K}_1 \cup \mathcal{K}_2 \cup \mathcal{K}_3 \in [1, N]$. Mapping matrices Ξ and Φ both have non-negative entries ($\Xi_{ij} \geq 0$ and $\Phi_{ij} \geq 0$) and column sums equal to unity (Section 3.3.2); this renders them so-called *stochastic matrices* [45]. Furthermore, redistribution of material by the mapping matrix over the cells is essentially the same as generic flows in networks and thus admits representation by graphs. These properties have essential consequences for their structures and the associated transport characteristics.

3.4.2 Graph representation of the mapping matrix

The mapping matrix can be thought of as an adjacency matrix of a graph with weighted and directed edges. This means that every cell $i = 1, 2, ..., N$ in the mapping grid corresponds with a vertex of graph $G(\Phi)$. Every nonzero entry Φ_{ij} indicates that there is a directed edge from vertex j to vertex i. This edge has weight Φ_{ij} and, because Φ may be asymmetric, the edge from i to j can have a different weight than the edge from j to i. The graph $G(\Phi)$ visualizes the redistribution of material over the entire domain within the course of one period. Figure 3.4 illustrates this graph representation of mapping matrices by way of a mapping mesh consisting of four cells and

$$\Phi = \begin{bmatrix} \Phi_{11} & \Phi_{12} & 0 & 0 \\ \Phi_{21} & \Phi_{22} & \Phi_{23} & \Phi_{24} \\ \Phi_{31} & 0 & 0 & \Phi_{34} \\ 0 & 0 & \Phi_{43} & 0 \end{bmatrix} \tag{3.11}$$

as the corresponding mapping matrix. Non-zero diagonal elements Φ_{ii} indicate retention of material within cell i and emerge as a self-loop in the graph (here e.g. for cells $i = 1,2$). Isolated zero entries Φ_{ij} imply absence of direct material transfer from cell j to cell i yet not necessarily *vice versa* (e.g. $i = 1$ and $j = 3$); diagonally-opposite zero entries ($\Phi_{ij} = \Phi_{ji} = 0$) reflect total absence of material exchange between cells i and j (e.g. $i = 1$ and $j = 4$). Material in cell i is after p periods distributed over cells (vertices) that are maximally p steps away in the graph. This means that full redistribution over all cells is either achieved in at most $p = N$ periods, manifesting itself in absence of zero entries in $\Phi' \equiv \Phi^N$, or never at all. Note Φ' for Φ following (3.11) is indeed devoid of such entries, signifying full redistribution. This also follows from the graph.

3.4.3 Block-diagonal structure of the mapping matrix

The above has the important implication that occurrence of any $\Phi'_{ij} = \Phi'_{ji} = 0$ implies disconnected subgraphs, which, in turn, signifies the presence of transport barriers in the underlying physical domain. In that case the mapping matrix admits transformation in a block-diagonal structure, where each block corresponds to a subregion in the graph (and physical domain) that is physically-separated from the rest. Consider to this end

$$\Phi = \begin{bmatrix} \Phi_{11} & 0 & \Phi_{13} & 0 \\ 0 & \Phi_{22} & 0 & \Phi_{24} \\ \Phi_{31} & 0 & \Phi_{33} & 0 \\ 0 & \Phi_{42} & 0 & \Phi_{44} \end{bmatrix} \quad \Rightarrow \quad \Phi'' \equiv \begin{bmatrix} \Phi_{11} & \Phi_{13} & 0 & 0 \\ \Phi_{31} & \Phi_{33} & 0 & 0 \\ 0 & 0 & \Phi_{22} & \Phi_{24} \\ 0 & 0 & \Phi_{42} & \Phi_{44} \end{bmatrix} \tag{3.12}$$

as alternative to (3.11). Here only material transfer takes place *within* yet not *between* the cell groups $\{1,3\}$ and $\{2,4\}$. This exposes a physical separation between both groups and, in consequence, admits transformation of Φ in given block-diagonal structure Φ'' via straightforward row/column permutations.

The presence of KAM tori in generic transport systems implies physical separation of flow regions and, inherently, of groups of cells (Conjecture 3). This means that the (conformal-grid) mapping matrix in general admits transformation in a

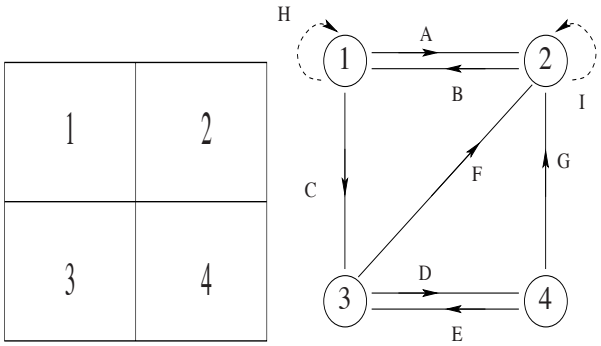

Figure 3.4: Graph representation of the mapping method: (a) mapping grid; (b) graph representing mapping matrix (3.11).

block-diagonal structure via

$$\Phi \quad \Rightarrow \quad \Phi'' = P\Phi P^T = \begin{bmatrix} A_1 & 0 & \dots & 0 \\ 0 & A_2 & \dots & 0 \\ \vdots & \vdots & \ddots & \vdots \\ 0 & 0 & \dots & A_k \end{bmatrix} \tag{3.13}$$

by way of a permutation P. Here each block A_k, which is completely decoupled from all other blocks, corresponds with the groups of cells covering a distinct LCS, defined by (clusters of) elliptic islands or chaotic seas. The eigenvalue-eigenvector pairs of the blocks combined span the eigenspace of Φ. Block-diagonal structure (3.13) is intimately related to the modal structure (3.10) and the underlying Conjecture 3 in that eigenmode sets $\mathcal{K}_{1,2}$ (islands) and $\mathcal{K}_3$ (chaotic seas), if present, belong to different blocks. Both sets admit further subdivision into blocks in case of multiple LCSs of the same type. This is demonstrated for the multiple islands in the TPSF at $T = 0.56$ in Section 3.6.

The underlying block-diagonal structure (3.13) imparts itself on the structure of the mapping matrix. Introduce to this end the matrix functional $Z(M)$, with $Z_{ij} = 0$ and $Z_{ij} = 1$ if $|M_{ij}| = 0$ and $|M_{ij}| > 0$, respectively. Its application to the mapping matrix Φ yields

$$Z(\Phi) = Z(\Phi^T) = Z(\Phi'), \tag{3.14}$$

implying that Φ identically adopts the beforementioned symmetric arrangement of zero and non-zero entries of Φ' that, in turn, signifies the presence of transport

barriers.[6] Hence, such barriers, if existent, leave a distinct footprint directly in the mapping matrix Φ. Conversely, this means that their existence *perse* can be readily inferred from the mapping matrix in that *any* diagonally-opposite zero entries signify transport barriers. (Note that this includes KAM tori within islands upon sufficient local conformity of the grid.) Their actual demarcation in the flow domain directly from Φ is non-trivial, however.

It must be stressed that the block-diagonal structure according to (3.13) is essentially different from a diagonalisation (or its generalisation, the Jordan canonical form [46]) by a similarity transform based on eigenvectors. The latter typically overlap (partially) in the physical domain and thus violate Conjecture 3. Transformation (3.13), on the other hand, leans on decomposition into spatially-separated groups of eigenvectors by reordering of cells.

The generic mapping matrix of a given flow is assembled from matrices A_k that each represent (clusters of) elliptic islands and chaotic seas. Each A_k in fact constitutes a mapping matrix in its own right for a specific flow region. The composition of the blocks depends on the associated Lagrangian flow structure. This is elaborated in the following section.

3.4.4 Block composition: elementary matrices

Mapping matrices Ξ and Φ both constitute stochastic matrices on grounds on non-negative entries and column sums equal to unity (Section 3.4.1). Matrix Ξ furthermore has row sums equal to unity and thus defines a *doubly-stochastic matrix* [45]. This has the important consequence that each vertex (cell) of the corresponding graph must have both incoming edges and outgoing edges. (This is in fact the generalisation of Kirchhoff's circuit laws for current flows in electrical circuits [47].) Note that this does not entail full connectivity of all cells; disconnected subgraphs, or equivalently, physical division of the flow domain in subregions is still possible. Moreover, since $\lim_{K\to\infty}\Phi = \Xi$, this property (to good approximation) carries over to Φ for sufficient seeding density K (Section 3.3.2).

The connection with (doubly-)stochastic matrices enables further exploration of the composition of the mapping matrix using general matrix theory. To this end properties relevant in the current context are recapitulated below [45, 48, 46].

[6] These conditions readily follow from $Z(\Phi^T) = [P^T Z(\Phi'')P]^T = P^T Z(\Phi''^T)P = P^T Z(\Phi'')P = Z(\Phi)$ and $Z(\Phi') = P^T Z(\Phi''^N)P = P^T Z(\Phi'')P = Z(\Phi)$ due to properties $Z(\Phi'') = Z(\Phi''^T) = Z(\Phi''^N)$, $PP^T = I$ and $Z(P) = P$.

Property 1 *Any stochastic matrix has conjugate complex eigenvalues* $|\lambda_k| \leq 1$ *and at least one eigenvalue* $\lambda_k = 1$ *(Perron-Frobenius theorem).*

This implies a multiplicity of eigenvalue $\lambda_k = 1$ that is at least equal to the number of blocks. Hence, such multiplicity may indicate – yet not conclusively establish – the existence of disconnected flow regions. Property 1 is consistent with the fact that the mapping matrix only admits persistent ($|\lambda_k| = 1$) and decaying ($|\lambda_k| < 1$) eigenmodes (Section 3.3.3). This advances permutation matrices $\underline{\Pi}$ and regular (doubly-)stochastic matrices D as elementary building blocks of mapping matrices, which is elaborated below.

Permutation matrices $\underline{\Pi}$ consist of entries equal to either zero or unity such that each column and row has only one non-zero element. Hence, each $\underline{\Pi}$ is in fact a permutation of the unit matrix I and thus defines a doubly-stochastic matrix. Thus a permutation matrix $\underline{\Pi}$ effectuates either complete or no transport of material from cell j to cell i: $\Phi_{ij} = 1$ or $\Phi_{ij} = 0$. Furthermore, this transport is such that *each* cell i transfers its material entirely to one companion cell j; division over multiple cells does not occur. This implies:

Property 2 *Permutation matrices* $\underline{\Pi}$ *have determinant* $\det(\underline{\Pi}) = \pm 1$ *and eigenvalues* $|\lambda_k| = 1$. *The associated graph admits at least one directed cycle without self-loops.*

Property 3 *Permutation matrices* $\underline{\Pi}$ *are periodic:* $\underline{\Pi}^{p+k} = \underline{\Pi}^p$ *and* $\underline{\Pi}^k = I$ *for all* $p \geq 1$ *and some periodicity* $k \geq 1$.

Property 4 *The (possibly repeated) eigenvalues of a permutation matrix with periodicity* k *are restricted to the* k *complex roots of unity:* $\lambda_k \in [1, \omega, \omega^2, \ldots, \omega^{k-1}]$.

Here $\omega = e^{2\pi i/k}$ and $i = \sqrt{-1}$. Note that the eigenvalue spectrum must not include all elements in this set; only $\lambda = 1$ is invariably present by virtue of Property (1).

Properties 2-4 imply two kinds of transport: (i) indefinite redistribution of material within cell groups; (ii) cyclic redistribution of material between cell groups. Former and latter scenarios respectively correspond to the action of persistent eigenmodes and the progression of material through coherent structures associated with clusters of periodic points (e.g. island chains). Thus persistent eigenmodes,

and by virtue of Conjecture 1, islands as well as generic higher-order periodic structures imply permutation matrices or permutation-like organization within the mapping matrix. This is worked out in Sections 3.4.5 and 3.4.6. Moreover, Property 4 cements Conjecture 4 and, given that (clusters of) coherent structures correspond with block matrices A and thus non-overlapping eigenvectors (Section 3.4.3), indirectly also Conjecture 5.

Regular (doubly-)stochastic matrices D are characterized by the property that $D' = D^k$, with k a given (finite) number of periods, consists entirely of non-zero elements: $D'_{i,j} > 0$ for all $i, j \in [1, N]$. This means that after k periods *each* cell has exchanged material with *all* cells (including itself) within the mapping mesh. The corresponding graph G connects any two cells i and j with a directed walk of at most length k. Hence, material from cell i reaches any cell j within at most k periods. Relevant properties are:

Property 5 *A regular stochastic matrix D has conjugate complex eigenvalues $|\lambda_k| < 1$ and one isolated eigenvalue $\lambda_k = 1$.*

Property 6 *A regular stochastic matrix D has a unique limit $\lim_{n\to\infty} D^n = L$. Each column of L is identical to the (normalized) eigenvector e of the isolated eigenvalue $\lambda_k = 1$.*

Property 7 *Eigenvector e is proportional to the unit vector ($e = N^{-1}1$) for $N \times N$ doubly-stochastic regular matrices.*

These properties imply that the progression of any given initial state c_0 converges on an asymptotic state proportional to e: $\lim_{n\to\infty} D^n c_0 \propto e$. Said state is homogeneous in case of doubly-stochastic regular matrices (as e.g. Ξ). This corresponds to the action of decaying eigenmodes. Chaotic seas are dictated entirely by such modes, meaning that corresponding block matrices in (3.13) are composed exclusively of regular (doubly-)stochastic matrices D. Hence, Property 5 substantiates Conjecture 2. Transport within islands, on the other hand, is governed by an interplay of both persistent and decaying eigenmodes; here block matrices thus are composed of permutation and regular stochastic matrices. The ramifications for the composition of actual mapping matrices are addressed in Sections 3.4.5 and 3.4.6.

Figure 3.5 gives a simple illustration of both matrix types for a 4-cell mesh with matrices

$$\underline{\Pi} = \begin{bmatrix} 1 & 0 & 0 & 0 \\ 0 & 0 & 1 & 0 \\ 0 & 1 & 0 & 0 \\ 0 & 0 & 0 & 1 \end{bmatrix}, \qquad D = \begin{bmatrix} \frac{1}{2} & 0 & \frac{1}{2} & 0 \\ 0 & 0 & \frac{1}{2} & \frac{1}{2} \\ \frac{1}{4} & \frac{3}{4} & 0 & 0 \\ \frac{1}{4} & \frac{1}{4} & 0 & \frac{1}{2} \end{bmatrix}. \tag{3.15}$$

Matrix $\underline{\Pi}$ has periodicity $k = 2$ and the initial state is restored identically after two periods: $\underline{\Pi}^2 = I$. Matrix D^3 has only nonzero entries, meaning that each cell has exchanged material with every other cell (including itself) after $k = 3$ periods. Furthermore, matrix D has a limit following Property 6 and corresponding columns $e = [1/4\ 1/4\ 1/4\ 1/4]$) as per Property 7. This ensures that redistribution by matrix D results in homogenisation of any initial state.

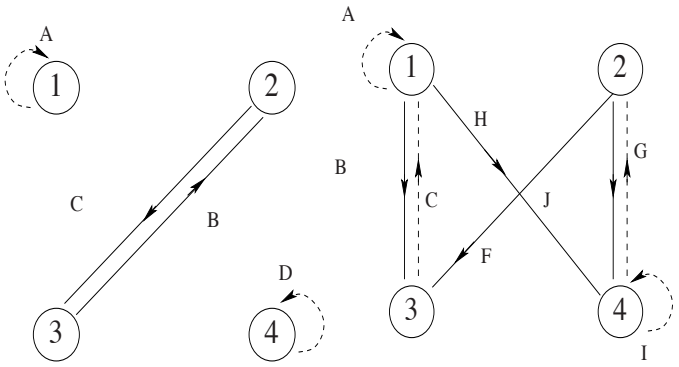

Figure 3.5: Transport by the elementary matrices: (a) permutation matrix $\underline{\Pi}$; (b) regular stochastic matrices D. Shown graphs correspond to examples (3.15).

3.4.5 Block composition: period-1 chaotic seas and islands

Periodic points are the organizing entities of the Lagrangian flow structure: period-1 points yield isolated LCSs; higher-order periodic points (periodicity $p > 1$) result in clusters of LCSs (Section 3.3.1). The above reconciled LCSs with two elementary matrices, i.e. permutation matrices and regular stochastic matrices, which fundamentally determines the composition of the block matrices A in (3.13). The remainder of this section treats this composition for the period-1 case; Section 3.4.6 continues with higher-order cases.

The evolution within chaotic seas is dictated solely by decaying eigenmodes and in Section 3.4.4 has been tied to regular stochastic matrices D. Hence, blocks A_k in (3.13) emanating from period-1 chaotic seas simply adopt the structure of said matrix type, viz.

$$A_k = D_k \quad A_{k,\infty} = \lim_{n\to\infty} A_k^n = L, \tag{3.16}$$

and directly inherit Properties 5-7. Note that Property 5 implies one unit eigenvalue – and thus one persistent eigenmode – for A_k. However, this merely, similar to the global trivial eigenmode, concerns total mass conservation within the chaotic sea and has no further effect upon the internal transport.

The case of period-1 islands is more involved in that transport ensues from an interplay of decaying and persistent eigenmodes. Performance of a local similarity transform yields

$$V_k^{-1} A_k V_k = \Lambda_k = \begin{bmatrix} \Lambda_\Pi & 0 \\ 0 & \Lambda_D \end{bmatrix}, \tag{3.17}$$

with matrices V_k and Λ_k containing the eigenvectors and eigenvalues, respectively, of A_k. Ordering is such that the eigenvalue spectrum is separated into persistent modes $|\lambda_i| = 1$ (held in Λ_Π) and decaying modes $|\lambda_i| < 1$ (held in Λ_D). Note that, due to non-conformity of the mapping grid with internal KAM tori and the inherent numerical diffusion, persistent eigenmodes (other than the mode representing total mass conservation) strictly are absent. However, the relatively simple geometry of said tori (i.e. concentric closed orbits) admits close conformity, causing persistent modes to emerge as modes "very close" to the unit circle. Relaxing the notion of persistence to remaining sufficiently invariant for relevant time spans enables distinction of (approximately) persistent modes by criterion $1 - |\lambda_k| \leq \epsilon$, with $0 < \epsilon \ll 1$ some tolerance set on a case-specific basis. (For chaotic seas such modes are absent due to the complex Lagrangian flow structure.)

Matrices Λ_Π and Λ_D are basically diagonalized representations of permutation and regular stochastic matrices $\underline{\Pi}$ and D, respectively. Primary difference is that the latter has the trivial limit $\lim_{n\to\infty} \Lambda_D^n = 0$ due to the absence of an eigenvalue equal to unity. This has the important consequence that matrix A_k asymptotes toward the "pseudo-permutation" matrix

$$\Pi_k = \lim_{n\to\infty} A_k^n \quad \Pi_k = V_k \Lambda_{k,\infty} V_k^{-1} = \Pi_k^p \quad \Lambda_{k,\infty} = \begin{bmatrix} \Lambda_\Pi & 0 \\ 0 & 0 \end{bmatrix}, \tag{3.18}$$

with p some periodicity.[7] The gradual diminution of contribution Λ_D^n paves the way to indefinite periodic redistribution of material within the cell group by $\Lambda_\Pi = \Lambda_\Pi^p$; this physically corresponds with the progression towards cyclically recurring persistent patterns within islands [34]. Note that typically $p > 1$; periodicity p namely concerns permutation of the individual cells within the period-1 island and not the island as a whole.

3.4.6 Block composition: higher-order periodicity

Clusters of elliptic islands

Transport within clusters of elliptic islands can be exemplified by way of the asymptotic state, described by pseudo-permutation matrices (3.18), without loss of generality. Moreover, their action is in essence equivalent to that of true permutation matrices. The latter acts on individual cells; the former acts on groups of cells corresponding with persistent eigenmodes of A_k. Consider to this end e.g. the asymptotic state within a cluster of period-2 islands. The cluster as a whole consists of 8 cells, 4 cells for island A and 4 cells for island B (Figure 3.6(a)). The corresponding graph in case $\underline{\Pi}_A = \underline{\Pi}_B = \underline{\Pi}$ following (3.15) is in Figure 3.6(b). Here the two kinds of transport associated with permutations, identified in Section 3.4.4, occur simultaneously: (i) redistribution within each island by 4×4 permutation matrices $\underline{\Pi}_A$ and $\underline{\Pi}_B$; (ii) periodic exchange of material between the islands by a permutation that fully exchanges the 4 cells covering islands A and B. This implies that transport and mixing is described by an 8×8 mapping matrix

$$A = \begin{bmatrix} 0 & \underline{\Pi}_A \\ \underline{\Pi}_B & 0 \end{bmatrix}, \tag{3.19}$$

with $\underline{\Pi}_A$ and $\underline{\Pi}_B$ two 4×4 permutation matrices. Important to note is that (3.19) has a permutation structure, say it that non-zero regions comprise elementary submatrices instead of individual entries. Hence, "nested permutations" exist here in that permutation happens concurrently on both intra-island and inter-island level. The period-2 behaviour manifests itself in the block-diagonal structure

$$A^{2p} = \begin{bmatrix} (\underline{\Pi}_A \underline{\Pi}_B)^p & 0 \\ 0 & (\underline{\Pi}_B \underline{\Pi}_A)^p \end{bmatrix} \qquad \forall p \geq 1, \tag{3.20}$$

[7] Note that Π_k, strictly, is not a true permutation matrix, since it accommodates null modes. However, these modes yield no contribution to the scalar field in the asymptotic limit, as these have diminished on account of the decaying modes. Hence, in this reduced eigenspace, Π_k acts as a true permutation matrix.

reflecting the invariance of the island cluster *as a whole* every two cycles yet with continuous *internal* redistribution by action of $\underline{\Pi}_A\underline{\Pi}_B$ and $\underline{\Pi}_B\underline{\Pi}_A$. This is fully consistent with the behaviour in clusters of elliptic islands in actual mixing flows (Section 3.3.1).

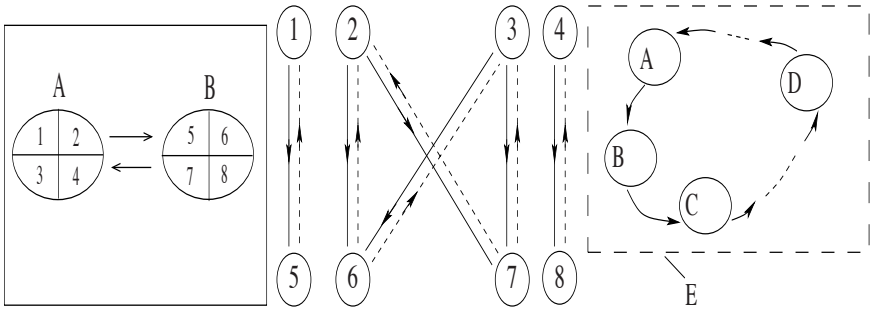

Figure 3.6: Transport within/between period-2 islands: (a) mapping grid; (b) graph for $\underline{\Pi}_A = \underline{\Pi}_B = \underline{\Pi}$ following (3.15); (c) inter-island permutation $\mathcal{I}_k \to \cdots \to \mathcal{I}_i \to \cdots \to \mathcal{I}_2 \to \mathcal{I}_1 \to \mathcal{I}_k$.

The above admits generalisation to clusters of period-k islands $\mathcal{I}_1 \cup \mathcal{I}_2 \cup \cdots \cup \mathcal{I}_k$. Essential to such clusters is that material contained in a given island $\mathcal{I}_p$ is always fully mapped to a companion island during each mapping. Ordering islands (and its corresponding groups of cells) such that material progresses through the cluster via $\mathcal{I}_k \to \mathcal{I}_{k-1} \to \cdots \to \mathcal{I}_2 \to \mathcal{I}_1 \to \mathcal{I}_k$ yields a corresponding graph on the inter-island level that forms a directed cycle (Property 2) following the schematic in Figure 3.6(c). Thus the associated inter-island mapping matrix collapses on the generic form

$$A \;=\; \begin{bmatrix} 0 & \underline{\Pi}_1 & & & \\ \vdots & 0 & \underline{\Pi}_2 & & \\ \vdots & & \ddots & \ddots & \\ 0 & & & 0 & \underline{\Pi}_{k-1} \\ \underline{\Pi}_k & 0 & \cdots & \cdots & 0 \end{bmatrix}, \tag{3.21}$$

with $\underline{\Pi}_p$ the intra-island permutation matrices. The period-k behaviour emanates

from Property 3 and manifests itself in a block-diagonal structure

$$A^k = \begin{bmatrix} \prod_{p=1}^{k} \underline{\Pi}_p & & & \\ & \prod_{p=1}^{k} \underline{\Pi}_{p+1} & & \\ & & \ddots & \\ & & & \prod_{p=1}^{k} \underline{\Pi}_{p+k-1} \end{bmatrix}, \quad (3.22)$$

where $\underline{\Pi}_{k+i} = \underline{\Pi}_i$ on grounds of the closed loop formed by the islands, reflecting the invariance of the island cluster as a whole. The matrix product in each block represents the continuous intra-island redistribution. The clusters of period-k islands thus, similar to the previous example, possess the same two levels of permutation: intra-island and inter-island permutations.

The inter-island permutation manifests itself in a particular "spectral footprint." Factorise A to this end in

$$A = \Pi_* A_*, \quad \Pi_* = \begin{bmatrix} 0 & I_* & \dots & 0 \\ \vdots & \ddots & \ddots & \\ 0 & \dots & 0 & I_* \\ I_* & 0 & \dots & 0 \end{bmatrix}, \quad A_* = \begin{bmatrix} \underline{\Pi}_1 & & & \\ & \ddots & & \\ & & & \underline{\Pi}_k \end{bmatrix}, \quad (3.23)$$

with I_* the block-size unit matrix.[8] Thus A consists of the product of the block-permutation matrix Π_*, with periodicity k (i.e. $\Pi_*^k = I$), and the block-diagonal matrix A_*, with permutation matrices as diagonal elements. Consider for simplicity all blocks of size $K \times K$. Eigenvalues of Π_* can for this particular permutation be shown to identify with the *full* set $\mathcal{P}(k) = [1, \omega, \omega^2, \dots, \omega^{k-1}]$, where $\omega = e^{2\pi i/k}$ (Property 4), with multiplicity K. Periodicities – and thus the corresponding eigenvalue spectra – of the individual matrices Π_i may vary yet two conditions are always met. First, $|\lambda_k| = 1$ (Property 2) for each Π_i, meaning all eigenvalues of A sit on the unit circle $|\lambda| = 1$ in the complex plane spanned by $(Re(\lambda), Im(\lambda))$. Second, at least one eigenvalue $\lambda_k = 1$ exists for each Π_i (Property 1). This implies k eigenvectors v_i of A_* that are invariant under its action: $A_* v_i = v_i$. These eigenvectors span a subspace $\mathcal{V} = [v_1, \dots, v_k]$ of the column space of A within which the latter acts as a permutation matrix, i.e. $Aw = \Pi_* w$ for $w \in \mathcal{V}$, due to

[8] Permutation matrix Π_* can be defined only for blocks of equal size; otherwise factorisation (3.23) adopts a tensor structure. (This is beyond the present scope). Block structures (3.21) and (3.22) are always valid.

$Av_i = \Pi_* v_i$. (Note that v_i are not eigenvectors of A or Π_*.) Thus the spectrum of A includes the k eigenvalues $\mathcal{P}(k)$ associated with the permutation matrix Π_*. Set $\mathcal{P}(k)$ constitutes the "signature" of the permutation and is denoted "permutation set" hereafter. Its presence in the eigenvalue spectrum of A further consolidates Conjecture 4 (Section 3.3.3).

A special case exists in repeated block matrices $\Pi_1 = \Pi_2 = \cdots = \Pi_k = \Pi$, which causes k-fold repetition of $\mathcal{Q} = eig(\Pi)$ ("parent spectrum") in the spectrum of A_*. This, on similar grounds as before, subdivides the column space of A into k subspaces $\mathcal{V}_i$, each spanned by eigenvectors belonging to identical eigenvalues λ_i, within which A acts as $Aw = \lambda_i \Pi_* w$. The generic matrix property $eig(\alpha B) = \alpha\, eig(B)$ then leads to

$$eig(A) = \mathcal{P}(k) \times \mathcal{Q}, \tag{3.24}$$

defined by the product of the spectra of its factors Π_* and A_*. The spectral footprint of A thus results from k-fold permutation of parent spectrum $\mathcal{Q}$ by the permutation set $\mathcal{P}(k)$, or equivalently, K-fold mapping of $\mathcal{P}(k)$. This is exemplified for Π following (3.15) and $k = 3$ as periodicity of Π_*. Here $\mathcal{P}(k) = [1, \omega, \omega^2]$, with $\omega = e^{2\pi i/3}$, and $\mathcal{Q} = [1,1,1,-1]$, yielding $eig(A) = [1, \omega, \omega^2, 1, \omega, \omega^2, 1, \omega, \omega^2, -1, -\omega, -\omega^2]$. Figure 3.7(a) gives the corresponding representation in the complex plane. Here stars indicate the parent spectrum $\mathcal{Q}$; circles and crosses indicate permutations by ω and ω^2, respectively. The star-circle-cross sequence starting from $\lambda = 1$ coincides with the permutation spectrum $\mathcal{P}(k)$. The spectrum for transient states is equivalent in the sense that form (3.24) is retained yet with parent spectrum also including $|\lambda| < 1$ associated with decaying modes. The spectral footprint is essentially as shown in Figure 3.7(a), expanded by modes within the unit circle.

The existence of distinct spectral footprints in principle facilitates isolation of clusters of islands in the total eigenvalue spectrum of the mapping matrix and this approach has found first applications in Singh *et al.* [34] However, multiplicity and restriction of persistent modes to the unit circle hamper this identification; this already happens in the above simple example, where the spectral footprint of the persistent modes erroneously suggests a six-fold permutation. Numerical effects enhance this identification in actual mapping matrices, though, by distorting the spectrum such that the permutation spectrum $\mathcal{P}(k)$ emerges closest to the unit circle (Section 3.5). This beneficial side effect of numerical errors has in fact already been exploited in Singh *et al.* [34].

Clusters of structures formed within/by chaotic seas

Clusters of structures associated with chaotic seas may emerge in two ways. First, in connection with multiple chaotic seas that are spatially-separated by e.g. symmetry planes. Second, in connection with clusters of higher-order hyperbolic points within one chaotic sea (Section 3.3.1). The block structure for the former kind identifies with that of island clusters, given by (3.21) and (3.23), upon substitution of Π_i by D_i. The spectrum retains the form (3.24) in the simplified case of identical block matrices D and its typical footprint is demonstrated in Figure 3.7(b) for equal block matrices D following (3.15) and $k = 3$. Important difference with the island case is that here only the permutation spectrum $\mathcal{P}(k)$ emerges on the unit circle on account of but one eigenvalue $\lambda = 1$ for each D_i (Property 5).

The case of clusters of structures within one chaotic sea is fundamentally different in that stringent spatial separation of individual elements of the cluster in disconnected groups of cells (as in an island chain) is absent. Manifold pairs of the periodic points each demarcate spatial areas $\mathcal{M}_i$ that, reminiscent of a jigsaw puzzle, interconnect and combined cover the chaotic sea by clustering following $\mathcal{M}_1 \cup \mathcal{M}_2 \cup \cdots \cup \mathcal{M}_k$. The highly-complex spatial structure of these conjugate regions and their intricate connections prohibit direct transformation into a block-diagonal structure similar to (3.21). Material nonetheless wanders cyclically through the chaotic sea via a directed cycle $\mathcal{M}_1 \to \mathcal{M}_2 \to \cdots \to \mathcal{M}_k$ in a manner akin to island chains (Section 3.4.6). This implies a similar permutation structure as (3.21) yet here "hidden" in the eigenmode decomposition of the block matrix A following

$$V^{-1}AV = \begin{bmatrix} 1 & 0 \\ 0 & \Lambda \end{bmatrix}, \quad \Lambda = \Pi_* \Lambda_*, \quad \Lambda_* = \begin{bmatrix} \Lambda_1 & & \\ & \ddots & \\ & & \Lambda_k \end{bmatrix}, \tag{3.25}$$

where factorisation into permutation and block-diagonal matrices occurs in eigenspace instead of in physical space. It must be stressed that the permutation acts only on the decaying modes, since only these modes contribute to the redistribution of material. The sole persistent mode, represented by the isolated unit entry in (3.25), corresponds to the trivial mode $\lambda = 1$ with homogeneous eigenvector covering the entire chaotic sea. Presuming, similar as before, identical $\Lambda_1 = \Lambda_2 = \cdots = \bar{\Lambda}$ yields $eig(A) = [1, \mathcal{P}(k) \times \mathcal{Q}]$, with here $\mathcal{Q} = eig(\bar{\Lambda})$, as corresponding eigenvalue

spectrum for A. The typical spectral footprint of this kind of LCS is illustrated in Figure 3.7(c) for $\bar{\Lambda} = diag(3/4, 1/2, -1/2)$; it deviates slightly from (3.24) by the presence of only eigenvalue $\lambda = 1$ on the unit circle. Compare this with the period-4 cluster of hyperbolic points for the TPSF at $T = 1.6$ in Singh *et al.* [34].

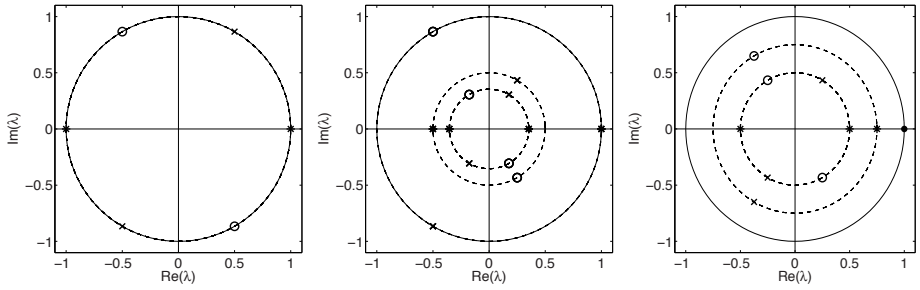

Figure 3.7: Spectral footprints of different types of Lagrangian coherent structures exemplified for periodicity $k = 3$: (a) a cluster of islands; (b) a cluster of chaotic seas; (c) clusters within one chaotic sea. Stars indicate the parent spectrum $\mathcal{Q}$; circles and crosses indicate permutations by ω and ω^2, respectively. The star-circle-cross sequence starting from $\lambda = 1$ coincides with the permutation spectrum $\mathcal{P}(k)$. The isolated eigenvalue $\lambda = 1$ (heavy dot) in panel (c) represents the trivial homogeneous eigenvector emanating from mass conservation.

3.4.7 Implications for transport properties

The specific composition of the mapping matrix manifests itself in the transport properties. Presence of a block-diagonal structure implies disconnected flow regions, each corresponding with one block matrix, separated by KAM tori. Conversely, absence of such a structure thus implies a system devoid of transport barriers. The most direct way to investigate this is via transformation (3.13). However, a generic algorithm is unavailable (Section 3.4.3). An indirect way exists in an eigenvalue decomposition. Eigenvalue $\lambda_{\max} \equiv \max_k |\lambda_k|$ of the non-trivial eigenmodes significantly smaller than unity implies one regular stochastic matrix (Property 5) and, in consequence, absence of a block-diagonal structure. Though efficient algorithms are available, this approach nonetheless is computationally intensive. A pragmatic alternative is to exploit the modal structure (3.10), which may be recast as

$$\Phi = \Phi_\infty + \Delta\Phi, \quad \Phi_\infty = \sum_{k \in \mathcal{K}_1} \lambda_k^{(1)} v_k^{(1)} v_k^{(1)}, \quad \Delta\Phi = \sum_{k \in \mathcal{K}_2 \cup \mathcal{K}_3} \lambda_k^{(2,3)} v_k^{(2,3)} v_k^{(2,3)} \quad (3.26)$$

with $\Phi_\infty = \lim_{p\to\infty} \Phi^p$ and $\Delta\Phi$ the asymptotic and transient contributions encompassing the persistent ($|\lambda_k^{(1)}| = 1$) and decaying ($|\lambda_k^{(2,3)}| < 1$) modes, respectively. (Hence $\lim_{p\to\infty} \Delta\Phi^p = 0$.) The structure of the asymptotic contribution Φ_∞ depends essentially on the presence/absence of transport barriers and may thus serve as a first indicator for a block-diagonal structure. Three kinds of asymptotic states Φ_∞ may occur (Section 3.4.4): (i) inhomogeneous $\Phi_\infty = L$ (identical columns) in case Φ is a regular stochastic matrix; (ii) homogeneous matrix $\Phi_\infty = H$ in case Φ is a regular doubly-stochastic matrix; (iii) inhomogeneous periodic $\Phi_\infty = \Phi_\infty^k$ (non-identical columns) in case Φ admits transformation into block-diagonal structure (3.13). The latter structure signifies disconnected flow regions and, inherently, presence of transport barriers. Important to note is that this affords a generic way to determine the global qualitative transport properties that, in contrast with e.g. Poincaré sectioning, is independent of the initial state.

The generic matrix properties also yield quantitative information on the transport properties. For the typical case of equidistant mapping grids, the block size in block-diagonal mapping matrices is a direct measure for the extent of the individual flow regions. This enables, once the nature of individual blocks (i.e. island or chaotic sea), has been established, evaluation of the relative area occupied by islands via $A_I = (N - S)/N$, where $0 \leq A_I \leq 1$. Here N and S correspond with total number of cells and cells covering islands, respectively, which follow readily from the row/column-wise extents of the full matrix and the blocks. The homogenisation rate within both global and local chaotic seas directly relates to the corresponding $\lambda_{\max}$ through the characteristic time $\tau = -T/\ln|\lambda_{\max}|$ for the decay of inhomogeneous states [34].

3.5 The mapping matrix for non-conformal grids

Premise for attainment of the mapping composition examined in Section 3.4 is that the mapping grid is perfectly conformal with the transport barriers separating islands from chaotic seas (Section 3.3.2). However, intricate entities as island chains and cantori emanating from KAM tori (Section 3.3.1) render a fully conformal mapping grid impossible. Moreover, its creation, even if possible, is highly impractical, as it requires *a priori* detailed knowledge of the LCSs. Hence, typical mapping matrices rely on non-conformal grids.

The principal consequence of non-conformal mapping grids is that the modal structure (3.10) breaks down in favour of

$$\widetilde{\Phi} = \sum_{k=1}^{N} \widetilde{\lambda}_k \widetilde{v}_k \widetilde{v}_k, \tag{3.27}$$

with $\widetilde{\Phi}$ possessing the properties of a regular stochastic matrix (column sums still amount to unity). This means that the eigenmodes consist of one trivial eigenvalue $\widetilde{\lambda}_1 = 1$ and eigenvalues $|\widetilde{\lambda}_k| < 1$ for $k > 1$ (Property 5). Hence, the eigenvalue spectrum, save the trivial one, resides entirely within the unit circle under non-conformal conditions. Eigenvector $\widetilde{v}_1$ is homogeneous only in case $\widetilde{\Phi}$ is doubly-stochastic (i.e. $\widetilde{\Phi} = \widetilde{\Xi}$) (Property 1). In the particle-based approach this eigenvector may be inhomogeneous (Section 3.4.4). Other eigenvectors are always inhomogeneous and include those associated with either islands or seas, as illustrated in Figure 3.3, augmented by global eigenmodes covering both islands and seas. Figure 3.8(a) gives a typical global eigenmode for the TPSF at $T = 0.8$.

The diffusion-induced global eigenmodes represent material exchange between elliptic islands and chaotic seas and have significant non-zero contributions throughout the entire flow domain. Their spatial structure nonetheless correlates well with said Lagrangian entities, as is evident upon comparing Figure 3.8(a) with the corresponding Poincaré section in Figure 3.1(b). This can be understood by realizing that these global eigenmodes are basically eigenmodes of adjacent LCSs "glued together" by the localized numerical diffusion near transport barriers induced by non-conformity of the mapping grid.

Mapping matrices for conformal and non-conformal grids formally relate via

$$\widetilde{\Phi} = \Phi + E = \begin{bmatrix} \widetilde{\Phi}_1 & E_{1,2} & & \cdots & & E_{1,k} \\ E_{2,1} & \ddots & & & & \\ & & \widetilde{\Phi}_i & \ddots & & \vdots \\ \vdots & & \ddots & \widetilde{\Phi}_{i+1} & & \\ & & & & \ddots & E_{k-1,k} \\ E_{k,1} & & \cdots & & E_{k,k-1} & \widetilde{\Phi}_k \end{bmatrix}, \tag{3.28}$$

with $E \equiv \widetilde{\Phi} - \Phi$ the difference matrix. Presence of the global eigenmodes in E prevents its transformation to a true block-diagonal structure (3.13). However, the

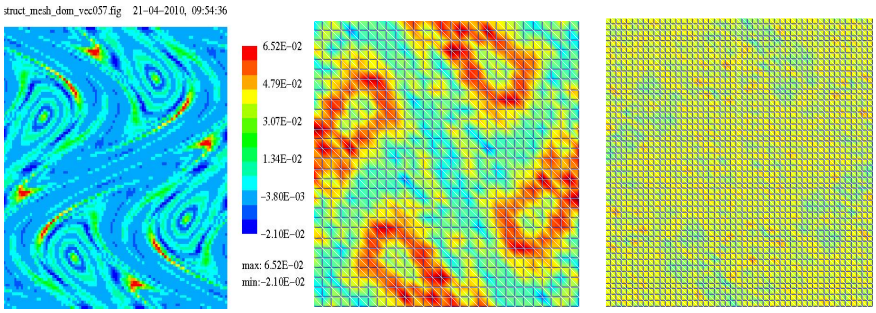

Figure 3.8: Effect of non-conformity of the mapping grid demonstrated for the TPSF at $T = 0.8$: (a) typical global eigenmode; (b) inhomogeneity of eigenmode $\widetilde{v}_1$ for $N = 900$; (c) inhomogeneity of eigenmode $\widetilde{v}_1$ for $N = 2500$. These inhomogeneities serve as indicator for numerical diffusion due to non-conformity. Red/blue indicate maximum/minimum magnitudes about zero level (green).

"contaminated" mapping matrix $\widetilde{\Phi}$ still is diagonally-dominant (i.e. $|E| \ll |\widetilde{\Phi}_i|$) yet with weak coupling between blocks. Inhomogeneity of $\widetilde{v}_1$ reflects departures from solenoidality and has a comparable impact upon the mapping matrix as numerical diffusion (Section 3.3.2). Hence, it may serve as indicator for the typical departure $\epsilon = |E|/|\Phi|$, with $|.|$ some matrix norm, from conformal-grid conditions. Figures 3.8(b) and (c) give this mode for $N = 900$ and $N = 2500$, respectively, where the inhomogeneity $\Delta v = \max(v_1) - \min(v_1)$ in former and latter case amounts to $\Delta v \sim \mathcal{O}(10^{-2})$ and $\Delta v \sim \mathcal{O}(10^{-3})$. Through $|E| \sim \mathcal{O}(\Delta v)$ and $|\Phi| \sim \mathcal{O}(1)$ this yields $\epsilon \sim \mathcal{O}(10^{-2})$ and $\epsilon \sim \mathcal{O}(10^{-3})$ for $N = 900$ and $N = 2500$, respectively. This exposes rapid diminution of numerical diffusion due to non-conformity with increasing N. Note that the spatial correlation between $\widetilde{v}_1$ and the associated transport barriers (Figure 3.1) substantiates the above assumption that this eigenmode is indicative of numerical diffusion.

An advantageous side effect of numerical diffusion is that it enhances discernibility of the spectral footprint of island clusters. Numerical diffusion means that the island-wise permutation matrices Π_i in (3.21) deform into island-wise matrices that approximately define regular stochastic matrices D_i in the sense that column sums are close yet not identical to unity. (This property is retained only by the total matrix $\widetilde{\Phi}$.) Spectrum $\mathrm{eig}(\widetilde{\Phi})$, save the trivial mode, residing within the unit circle implies $|\lambda| < 1$ for $\lambda \in \mathrm{eig}(D_i)$. Presuming again island-wise identical matrices within a period-k island chain leads to an equivalent spectrum (3.24) of the

associated block matrix yet with parent spectrum $\mathcal{Q}$ comprising eigenvalues with decreasing magnitude, i.e. $1 > |\lambda_1| > |\lambda_2| > \cdots > |\lambda_K|$. This causes contraction of the spectral footprint of the persistent eigenmodes (Figure 3.7(a)) onto concentric circles in a similar way as illustrated in Figure 3.7(b) for clusters of separated chaotic seas ($k = 3$), albeit with outer circle inside the unit circle. Here each concentric circle accommodates a rescaled version of the permutation spectrum $\mathcal{P}$, thus considerably enhancing its detection compared to the ideal case in Figure 3.7(a). This effect greatly benefits isolation of island clusters and has already been exploited by Singh *et al.* [34].

3.6 A representative example

The composition of the mapping matrix is demonstrated by way of the TPSF for $T = 0.56$. To this end the permutation matrix P in (3.13) is manually constructed by subdivision of the cells of the 50×50-cell mapping grid into groups covering different LCSs (Figure 3.1(a)). Here three (clusters of) LCSs can be discerned: two period-1 islands; encircling island chains; one chaotic sea. Further spatial features are of sub-cell scale and thus beyond the adopted mapping grid. The original mapping matrix Φ is ordered according to cell position in the regular grid; numbering starts in the upper left corner (cell 1) and row-wise progresses downwards to the lower right corner (cell 2500). The permutation is visualized in Figure 3.9 by an overlay of the mapping grid and the Poincaré section, with cell groups corresponding with said Lagrangian entities highlighted in colour.

Figure 3.10 gives the original mapping matrix Φ (panel (a)) and its permuted counterpart Φ'' according to (3.13) (panel (b)) in a 2D representation with vertical/horizontal coordinates identifying with rows/columns. Markers and blank regions indicate non-zero and zero entries, respectively. Colour coding in Φ'' coincides with that of the cell groups in Figure 3.9; vertical and horizontal lines separate the cell groups. This discloses a symmetric matrix with a distinct band structure in Φ comprising a diagonal band and two off-diagonal regions in upper-right and lower-left corners. The latter emanate from the periodic boundary conditions; the symmetry results from the time-reversal symmetry of the flow F (Section 3.3.1).

The permuted matrix Φ'' closely resembles a block diagonal structure, where block matrices correlate with the LCSs. The individual blocks exhibit weak coupling through the non-zero entries in the off-diagonal blocks due to numerical effects. This essentially confirms the composition of the mapping matrix predicted

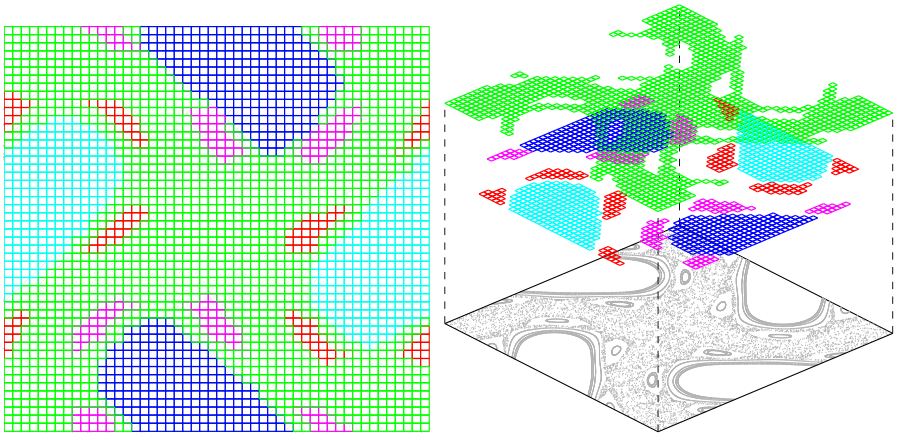

Figure 3.9: Subdivision of the mapping grid according to transport barriers separating LCSs for the TPSF at $T = 0.56$: (a) planar view; (b) exploded view including Poincaré section. Colours distinguish different (clusters of) islands and chaotic regions.

in Sections 3.4 and 3.5. Important to note is that the weak coupling primarily concerns the chaotic sea (green) and the period-1 islands (blue and cyan); the off-diagonal blocks adjacent to the diagonal blocks of the period-1 islands are completely devoid of non-zero entries, signifying complete decoupling. This is consistent with the fact that numerical effects are most prominent in the transition region between surviving (portions of) islands and the chaotic sea (Section 3.5). The blocks corresponding to period-1 islands and encircling island chains are, similar to these Lagrangian entities, of equal shape, which is a further manifestation of the beforementioned time-reversal symmetry of F.

Reordering the block matrix A in Φ'' corresponding with the island chain highlighted in Figure 3.11(a) (indicated in red in Figures 3.9 and 3.10(b)) island-wise by their position within the chain (blue-cyan-black-red-green-magenta) exposes the intra-cluster structure of the mapping matrix. (The previous permutation orders cells within groups according to their row position in the original matrix.) Block matrix A thus reordered is given in Figure 3.11(b) and adopts the generic permutation form (3.21) for a period-6 cluster. Important to note here is that the individual blocks are of unequal size, disabling a matrix decomposition (3.23) and necessitating a tensor-based decomposition instead (Section 3.4.6). The invariance of the cluster as a whole dictates that A^k, with here $k = 6$, collapses on

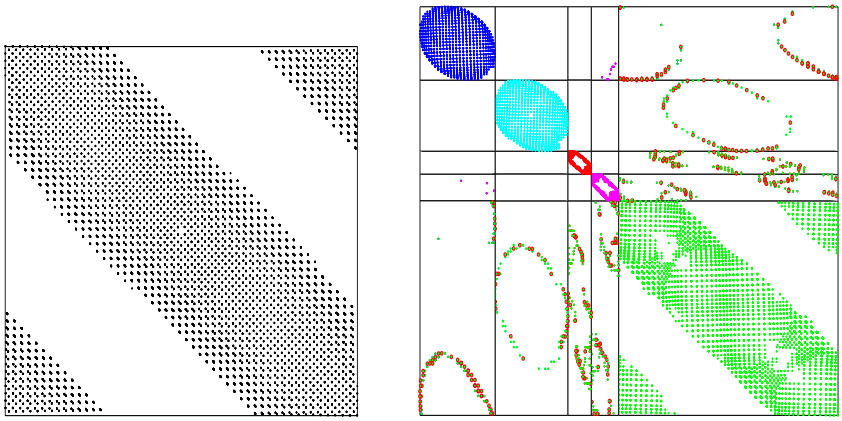

Figure 3.10: Block-diagonal structure associated with disconnected LCSs for the TPSF at $T = 0.56$: (a) original matrix Φ based on standard sequential cell numbering; (b) permuted matrix Φ'' using the subdivision of following Figure 3.9. Colours correspond with the LCSs in Figure 3.9.

the generic block-diagonal structure following (3.22), where the sequence of blocks corresponds with the position of the islands in the cluster. Figure 3.11(c) shows the structure of A^k, with colour coding as before, and visually verifies compliance with this essential condition.

The eigenvalue spectrum of A is given in Figure 3.12(a) and coincides well with the generic spectral footprint of island chains predicted in Section 3.4.6 in that it exhibits a distinct six-fold rotationally-symmetric pattern closely resembling the ideal form (3.24) for $k = 6$. Its confinement within a circle $\lambda_{\max} \equiv \max_k |\lambda_k|$ (dashed), with $\lambda_k \in \mathcal{Q}$ and $\lambda_{\max} = 0.9218$, is caused by the contraction of the spectrum of the persistent eigenmodes onto (approximately) concentric circles $|\lambda| < 1$ due to numerical effects (Section 3.5). This exposes a cluster of six eigenvalues, equidistantly distributed over the outer circle $\lambda_{\max}$ (indicated by circles in Figure 3.12(a)), as the permutation spectrum $\mathcal{P}(k)$. Hence, the actual spectral footprint is in excellent agreement with its predicted emergence. The significant departure from the unit circle signifies a relatively strong effect of numerical diffusion, which is a direct consequence of the comparably high cell-size to feature-size ratio in the island chain. Typical eigenvectors are given in Figures 3.12(b) $\lambda = \lambda_{\max}$ and (c) $\lambda = -\lambda_{\max}$ and, consistent with Conjecture 5, indeed reveal spatial distributions

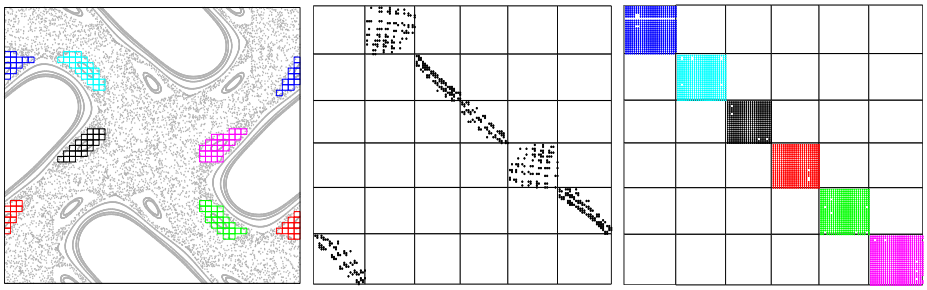

Figure 3.11: Composition of the block matrix A associated with a period-6 island chain of the TPSF at $T = 0.56$: (a) island chain with its 6 individual islands highlighted; (b) structure of A; (c) diagonal structure of A^k ($k = 6$) reflecting the permutation along the individual islands.

that combined cover the entire island chain.

Transformation into a block-diagonal structure has in the above been accomplished by way of a manually-constructed permutation matrix P. For generic mapping matrices this can formally be achieved through transformation (3.13), which is far from trivial, however. Determination of whether a block-diagonal structure is present may adopt the approach based on the asymptotic mapping matrix $\Phi_\infty = \lim_{p\to\infty} \Phi^p$ proposed in Section 3.4.7. Here it must be taken into account that numerical effects cause block matrices of islands to (approximately) become regular stochastic matrices yet with eigenvalues significantly closer to the unit circle than for chaotic seas (Section 3.5). Hence, block matrices corresponding with islands strictly spoken no longer converge on inhomogeneous periodic matrices $\Phi_\infty = \Phi_\infty^k$ yet nonetheless closely follow that scenario in that their progression towards a homogeneous asymptotic state is considerably slower than that of block matrices associated with chaotic seas. This implies relatively long-lived inhomogeneities in the mapping matrix in cell groups coinciding with islands during its evolution towards $\Phi_\infty = L$ (regular stochastic matrix) or $\Phi_\infty = H$ (regular doubly-stochastic matrix) in a manner reminiscent of strange eigenmodes in evolving scalar fields [34]. Numerical investigation confirms this behaviour and reveals that the mapping matrix within 10-15 periods converges on an asymptotic state with columns coinciding within $\mathcal{O}(10^{-14})$. Figure 3.13 gives the spatial distribution of those columns for T as indicated and exposes an evident dependence on the Lagrangian flow structure (Figure 3.1). Case $T = 0.56$ adopts a pattern that closely correlates with the period-1 islands; case $T = 1.6$, in contrast, assumes

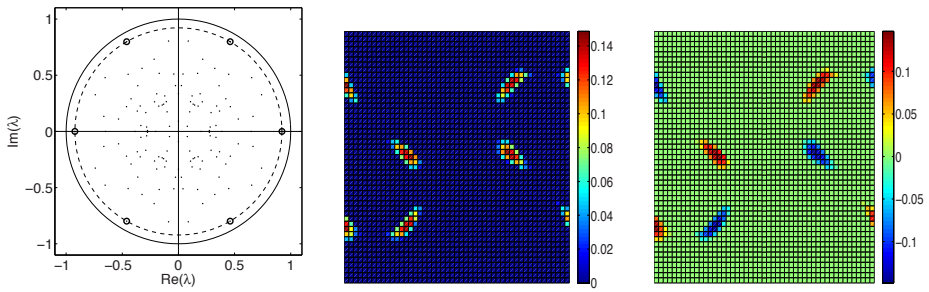

Figure 3.12: Footprint of the period-6 island chain for the TPSF at $T = 0.56$: (a) eigenvalue spectrum with the island chain located on the circle $|\lambda| = \lambda_{\mathsf{max}} = 0.9218$ (dashed) indicated by small circles; (b) eigenvector corresponding with $\lambda = \lambda_{\mathsf{max}}$; (c) eigenvector corresponding with $\lambda = -\lambda_{\mathsf{max}}$. Red/blue indicate maximum/minimum magnitudes about zero level (green).

a random distribution, consistent with its globally-chaotic state. Important to note is that both states correspond with the inhomogeneous asymptotic matrix $\Phi_\infty = L$, with fluctuations of $\mathcal{O}(10^{-4})$, on account of the fact that Φ is a regular stochastic matrix. Thus the departure from a true doubly-stochastic mapping matrix Ξ (Section 3.3.2) in fact is beneficial here in that it facilitates robust detection of inhomogeneities that, in turn, imply transport barriers and, inherently, an approximate block-diagonal structure of the mapping matrix according to (3.28).

3.7 Conclusions

The present study investigates the composition of the mapping matrix in relation to the Lagrangian flow structure and expands on earlier work by Singh *et al.* [34]. This is motivated by finding ways to systematically manipulate the properties of the mapping matrix for various transport purposes. Primary objective is achievement of efficient mixing, but other aims as accomplishment of distinct concentration distributions or Lagrangian flow structures for e.g. (local) catalysation of chemical reactions in labs-on-a-chip or manufacturing of anisotropic micro-fibres, become increasingly relevant with the growing role of micro-fluidics. Redistribution of material by the mapping matrix is essentially the same as flows in networks and thus admits representation by graphs and associated distribution matrices. This facilitates a robust analysis on the generic composition of the mapping matrix – and its underlying continuous transport operator – that combines concepts and results from operator, graph and matrix theory.

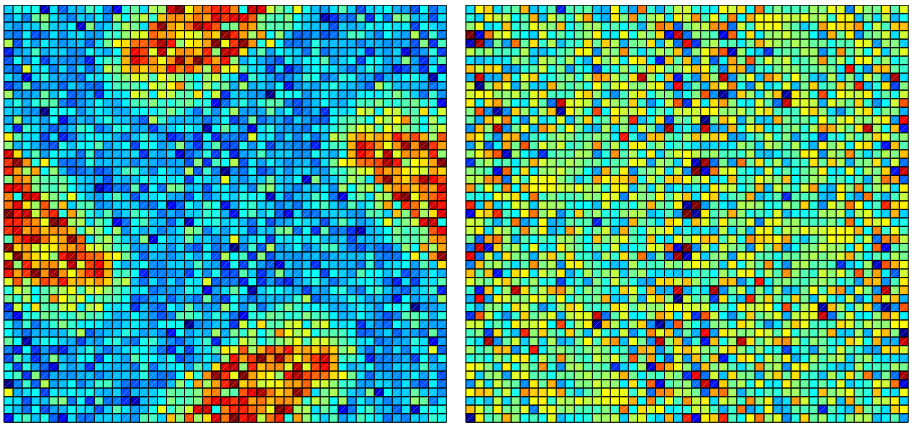

Figure 3.13: Spatial pattern of the asymptotic mapping matrix Φ_∞ for the TPSF and its correlation with the Poincaré map: (a) $T = 0.56$; (b) $T = 1.6$.

The mapping matrix possesses a block-diagonal structure that reflects the formation of distinct – and spatially disconnected – Lagrangian coherent structures (LCSs) in the flow field: elliptic islands and chaotic seas. Each block matrix represents one such LCS and defines a mapping matrix in its own right. The latter, in turn, identify with stochastic matrices, which implies a composition based on two elementary matrices, i.e. permutation matrices and regular stochastic matrices, that directly relate to the dynamics. Permutation matrices represent purely advective redistribution of material; regular stochastic matrices represent the (local) homogenisation of concentration distributions due to the interplay of advection and weak, yet physically inevitable, molecular diffusion. Hence, permutation matrices are inextricably linked with asymptotic (inhomogeneous) concentration distributions – and thus persistent eigenmodes – as well as with periodic events (e.g. cyclic redistribution of material in island chains). Regular stochastic matrices correspond with transient states and, inherently, with decaying eigenmodes. Each LCS leaves a particular spectral footprint in the eigenvalue spectrum of the mapping matrix that betrays its kind and its periodicity. The present study thus exposed the fundamental connection between the Lagrangian flow structure and the spectral properties of the (discrete) transport operator.

The matrix structure has been investigated for a representative example accommodating a typical Lagrangian flow structure comprising islands of various pe-

riodicity embedded in a chaotic sea. This yields a mapping matrix that is entirely consistent with the predicted composition on the basis of the corresponding LCSs. A block-diagonal structure, implying transport barriers and disconnected LCSs, is found with block matrices according to the spectral footprints of the associated LCSs. Non-conformity of the mapping grid with transport barriers introduces a weak coupling between the block matrices through small off-diagonal contributions. This alters the spectral footprints of the LCSs by shifting the eigenvalues slightly inside the unit circle yet with retention of their characteristic structure.

The fundamental connection between the mapping matrix and generic flows in networks may facilitate development of control strategies for the accomplishment of specific transport properties and Lagrangian flow structures. This may have particular potential in micro-fluidic applications due to the various promising flow-forcing methods [24, 25, 27]. The impact and scope of flow control on the basis of the Lagrangian flow structure may be augmented by further unravelling its connection with the composition of the mapping matrix. This may benefit from exploring links of the mapping method with Koopman operators [28, 49]. Efforts to this effect are in progress. Extension to essentially 3D flows is, owing to its far more complex Lagrangian flow structure [50, 51, 52, 53, 54], likely to offer many new ways for accomplishing transport capabilities. However, this is a formidable challenge, since insight into truly 3D transport phenomena – and then in particular under unsteady conditions – remains limited to date [55].

The analysis of the case study leans on manual decomposition of the mapping matrix. This is evidently not an option for generic applications. (Mapping grids may e.g. comprise of up to 3000×3000 cells [37].) Transformation of mapping matrices into block-diagonal structure as well as isolating the particular permutation structure (3.21) associated with higher-order periodicity can be achieved by epsilon decomposition. This method is widely employed in decentralized control for disconnecting parts of a system that exhibit only weak coupling (according to a preset criterion) [56]. Important in the present context is that this method is also applicable to mapping matrices suffering from weakly-coupled block matrices due to numerical diffusion (i.e. the typical case). Subsequent association of the block matrices to elliptic islands and chaotic seas can be done on the basis of the characteristic spectral footprints of these entities.

Bibliography

[1] N. Harnby, M.F. Edwards, and A.W. Nienow, Mixing in the process industries, Butterworth-Heinemann, Oxford, 1997.

[2] R.K. Thakur, Ch. Vial, K.D.P. Nigam, E.B. Nauman, and G. Djelveh, Static mixers in the process industries – a review, Trans IChemE 81, 2003, pp. 787.

[3] J.M. Ottino, Mixing, chaotic advection and turbulence, Annu. Rev. Fluid Mech. 22, 1990, pp. 207-253.

[4] S. Wiggins, The dynamical systems approach to Lagrangian transport in oceanic flows, Annu. Rev. Fluid. Mech. 37, 2004, pp. 295-328.

[5] P.E. van Keken, E.H. Hauri, and C.J. Ballentine, Mantle mixing: the generation, preservation, and destruction of chemical heterogeneity, Annu. Rev. Earth Planet Sci. 20, 2002, pp. 493-525.

[6] H. Aref, Stirring by chaotic advection, J. Fluid Mech. 143, 1984, pp. 1-21.

[7] J. M. Ottino, The kinematics of mixing: Stretching, chaos, and transport, Cambridge University Press, 1989.

[8] H. Aref, The development of chaotic advection, Pys. Fluids 14, 2002, pp. 1315-1325.

[9] R. Weinekötter, Compact and efficient continuous mixing processes for production of food and pharmaceutical powders, Trends Food Sci. Tech. 20, 2009, S48.

[10] B. Weigl, G. Domingo, P. Labarre, and J. Gerlach, Towards non- and minimally instrumented, microfluidics-based diagnostic devices, Lab on Chip 8, 2008, pp. 1999.

[11] T.L. LaPorte and C. Wang, Continuous processes for the production of pharmaceutical intermediates and active pharmaceutical ingredients, Curr. Opin. Drug Discov. Devel. 10, 2007, pp. 738.

[12] S. Becht, R. Franke, A. Geißelmann, and H. Hahn, Micro process technology as a means of process intensification, Chem. Eng. Technol. 30, 2007, pp. 295.

[13] H.A. Stone, A.D. Stroock, and A. Ajdari, Engineering flows in small devices: Microfluidics toward a lab-on-a-chip, Annu. Rev. Fluid Mech. 36, 2004, pp. 381-411.

[14] J. M. Ottino and S. Wiggins, Introduction: mixing in microfluidics, Phil. Trans. R. Soc. London A 362, 2004, pp. 923-935.

[15] C. Hansen and S.R. Quake, Microfluidics in structural biology: smaller, faster ... better, Curr. Opin. Struct. Biology 13, 2002, pp. 538.

[16] D.J. Beebe, G.A. Mensing, and G.M. Walker, Physics and applications of microfluidics in biology, Annu. Rev. Biomed. Engng 4, 2002, 261.

[17] S. Wiggins and J. M. Ottino, Foundations of chaotic mixing, Phil. Trans. R. Soc. London A 362, 2004, pp. 937-970.

[18] M. Branicki and S. Wiggins, An adaptive method for computing invariant manifolds in non-autonomous, three-dimensional dynamical systems, Physica D 238, 2009, pp. 1625-1657.

[19] I. Mezić and S. Wiggins, A method for visualization of invariant sets of dynamical systems based on ergodic partition, Chaos 9, 1999, pp. 213-218.

[20] I. Mezić and F. Sotiropoulos, Ergodic theory and experimental visualization of chaos, Phys. Fluids 14, 2002, pp. 2235-2243.

[21] G. Metcalfe, M.F.M. Speetjens, D.R. Lester, and H.J.H. Clercx, Beyond passive: chaotic transport in stirred fluids, Adv. Appl. Mech. 45, 2011, pp. 109-188.

[22] S. Cerbelli, A. Adrover, F. Creta, and M. Giona, Foundations of laminar chaotic mixing and spectral theory of linear operators, Chem. Eng. Sci. 61,2006, pp. 2754-2761.

[23] W. Liu and G. Haller, Strange eigenmodes and decay of variance in the mixing of diffusive tracers, Physica D 188, 2004, pp. 1-39.

[24] T. G. Kang, M. A. Hulsen, P. D. Anderson, J. M. J. den Toonder, and H. E. H. Meijer, Chaotic mixing induced by a magnetic chain in a rotating magnetic field, Phys. Rev. E 76, 2007, 066303.

[25] J. M. J. den Toonder, F. M. Bos, D. J. Broer, L. Filippini, M. Gillies, J. de Goede, T. Mol, M. A. Reijme, W. Talen, H. Wilderbeek, V. Khatavkar, and P. D. Anderson, Artificial cilia for active micro-fluidic mixing, Lab Chip 8, 2008, pp. 533-541.

[26] T.M. Squires, Induced charge electrokinetics: fundamental challenges and opportunities, Lab on Chip 9, 2009, 2477.

[27] M. F. M. Speetjens, H. N. L. de Wispelaere, and A. A. van Steenhoven, Multifunctional Lagrangian flow structures in 3D ACEO micro-flows, Fluid. Dyn. Res. 43, 2011, 035503.

[28] I. Mezić, Spectral properties of dynamical systems, model reduction and decompositions, Nonlin. Dyn. 41, 2005, pp. 309-325.

[29] C.W. Rowley, I. Mezić, S. Bagheri, P. Schlatter, and D.S. Henningson, Spectral analysis of nonlinear flows, J. Fluid Mech. 614, 2009, pp. 115-127.

[30] P.D. Anderson, O.S. Galaktionov, G.W.M. Peters, H.E.H. Meijer, and C.L. Tucker, Material stretching in laminar mixing flows: extended mapping technique applied to the journal bearing flow, Int. J. numer. Methods Fluids 40,2002, pp. 189-196.

[31] M.K. Singh, P.D. Anderson, M.F.M. Speetjens, and H.E.H. Meijer, Optimizing the Rotated Arc Mixer, AIChE J. 54, 2008, pp. 2809-2822.

[32] Y. Le Guer and E. Schall, A mapping tool using anisotropic unstructured meshes to study mixing in periodic flows Chem. Eng. Sci. 59, 2004, pp. 1459-1472.

[33] O.S. Galaktionov, P.D. Anderson, G.W.M. Peters, and H.E.H. Meijer, Mapping approach for 3D laminar mixing simulation: application to industrial flows, Int. J. numer. Methods Fluids 40, 2002, pp. 189-196.

[34] M.K. Singh, M.F.M. Speetjens, and P.D. Anderson, Eigenmode analysis of scalar transport in distributive mixing, Phys. Fluids 21, 2009, 093601.

[35] S. Cerbelli, A. Adrover, and M. Giona, Enhanced diffusion regimes in bounded chaotic flows, Physics Letters A 312, 2003, pp. 355-362.

[36] S. Cerbelli, V. Vitacolonna, A. Adrover, and M. Giona, Eigenvalue-eigenfunction analysis of infinitely fast reactions and micromixing regimes in regular and chaotic bounded flows, Chem. Eng. Sci. 59, 2004, pp. 2125-2144.

[37] O. Gorodetskyi, M. Giona, and P.D. Anderson, Exploiting numerical diffusion to study transport and chaotic mixing for extremely large Péclet values, Europhys. Lett. 97, 2012, 14002.

[38] E. Ott, Chaos in Dynamical Systems, 2002, Cambridge University Press.

[39] R.S. MacKay, J.D. Meiss, and I.C. Percival, Stochasticity and transport in Hamiltonian systems, Phys. Rev. Lett. 52, 1990, 697.

[40] Y.-C. Lai and T. Tél, Transient chaos: Complex Dynamics on Finite Time Scales, 2011, Springer-New York.

[41] V.V. Meleshko and G.W.M. Peters, Periodic points for two-dimensional Stokes flow in a rectangular cavity, Physics Letters A 216, 1996, pp. 87-96.

[42] M.F.M Speetjens, H.J.H. Clercx, and G J F van Heijst, A numerical and experimental study on advection in three-dimensional Stokes flows, J. Fluid Mech. 514, 2004, 77.

[43] R. Spencer and R. Wiley, The mixing of very viscous liquids, J. Colloid Sci. 6, 1951, pp. 133-145.

[44] M.K. Singh, O.S. Galaktionov, H.E.H. Meijer, and P.D. Anderson, A simplified approach to compute distribution matrices for the mapping method, Comput. Chem. Eng. 33, 2009, pp. 1354-1362.

[45] S.H. Friedberg, A.J. Insel, and L.E. Spence, Linear Algebra, 1997, Prentice Hall, New Jersey.

[46] G. Strang, Linear Algebra and its Applications, 1976, Harcourt Brace Jovanovich, San Diego.

[47] C.R. Paul, Fundamentals of Electric Circuit Analysis, 2001, Wiley, Chichester.

[48] F. Gebali, Analysis of Computer and Communication Networks, 2008, Springer, New York.

[49] I. Mezić, Analysis of fluid flows via spectral properties of the Koopman operator, Annu. Rev. Fluid Mech. 45, 2013, pp. 357-378.

[50] I. Mezić and S. Wiggins, On the integrability and perturbation of three-dimensional fluid flows with symmetry, J. Nonlinear Sci. 4, 1994, pp. 157-194.

[51] J.H.E. Cartwright, M. Feingold, and O. Piro, Chaotic advection in three-dimensional unsteady incompressible laminar flow, J. Fluid Mech. 316, 1996, pp. 259-284.

[52] M.F.M. Speetjens, H.J.H. Clercx, and G.J.F. van Heijst, Inertia-induced coherent structures in a time-periodic viscous mixing flow, Phys. Fluids 18, 2006, 083603.

[53] I. Mezić, Break-up of invariant surfaces in action-angle-angle maps and flows, Physica D 154, 2001, 51.

[54] G. Haller, Distinguished material surfaces and coherent structures in three-dimensional fluid flows, Physica D 149, 2001, pp. 248-277.

[55] S. Wiggins, Coherent structures and chaotic advection in three dimensions, J. Fluid Mech. 654, 2010, pp. 1-4.

[56] L. Bakule, Decentralized control: An overview, Annu. Rev. Control 32, 2008, pp. 87-98.

Chapter 4

Mixing from a switching dynamics perspective

M. Lauret, V.S. Dolk, D.J. Antunes, P.D. Anderson, W.P.M.H. Heemels[1]

4.1 Abstract

Chaotic advection can significantly improve mixing speed in Stokes flows. Until now, the study of chaotic advection was mostly restricted to time-periodic and spatial-periodic flows, although some examples show that aperiodic flows can mix more efficiently. In this paper a new and general perspective on mixing is presented based on switching dynamical systems that allows the systematic derivation of aperiodic flows that are theoretically guaranteed to yield better mixing than any available periodic flow. Simulations and real-time feedback experiments for mixing control confirm these findings. The application of closed-loop control for mixing is expected to have significant advantages in micro-fluidic and industrial mixing and could enable the creation of desired nonhomogeneous patterns.

[1]This chapter is to be submitted to Physical Review E.

4.2 Introduction

Transport and mixing in fluid flows is crucial for many problems and applications at a variety of scales. Examples are the transport of plankton or oil in the ocean, industrial mixing of food and polymers and micro-mixing in a lab-on-a-chip. Most of these examples concern laminar Stokes flows. For a long time it was believed that turbulent flows were required to ensure mixing of particles, material or energy.

However, it has been shown that efficient mixing can occur in laminar Stokes flows due to chaotic advection [1, 2], a continual process of stretching and folding that can occur in time-dependent two-dimensional flows and in stationary (and time-dependent) three-dimensional flows.

In most of the traditional academic examples of mixing in flows with chaotic advection (such as the blinking vortex, the cavity flow, the journal bearing flow [2], and the time-periodic sine flow [3]), mixing is achieved by applying periodic flows with fixed period T_p. The resulting systems are studied as time-periodic, two-dimensional flows satisfying $\vec{v}(x,y,t) = \vec{v}(x,y,t+T_p)$. The time period T_p critically determines the mixing behavior. Under specific conditions, optimal periods can be derived [4, 5].

However, some, mostly simulated, examples suggest that aperiodic flows can improve mixing significantly [3, 6, 7, 8], although no general explanation of this phenomenon has been given in the literature. This contribution shows that chaotic mixing systems can be described as switching dynamical systems in which the mixing protocols correspond to switching sequences. A so-called rollout algorithm can be used to determine aperiodic flows that mix as least as fast as the best known (periodic) flows. Novel theoretical, numerical and experimental evidence is presented showing that aperiodic switching sequences can be systematically found that lead to faster homogeneous mixing, compared to both periodic and aperiodic switching sequences constructed by the existing minimum error method [6, 7]. In addition, the derived aperiodic flows are also less sensitive to the initial concentration distribution and other uncertainties. The method can be naturally implemented for real-time feedback control of mixing (for different theoretical approaches to feedback control of mixing, see [7, 9, 10, 11]). For the first time, such a theoretically derived feedback mixing controller with guaranteed performance is demonstrated experimentally.

4.3 Method

The method is explained using a two-dimensional bounded domain Ω with a divergence-free flow $\vec{v}(x,y,t)$ and a concentration distribution $c(x,y,t)$. Note that the results also hold for three-dimensional flows and the distributions of other quantities. The Péclet number Pe is very high, and therefore the diffusive transport is small compared to advection, which is the dominant transport mechanism. In the remainder of the paper, pure advection will be assumed. However, as the flow evolves according to the advection-diffusion equation $\frac{\partial c}{\partial t} = -\vec{v}\cdot\nabla c + \frac{1}{Pe}\triangle c$, the method can be generalised to flows with significant diffusion. A time-varying flow is mixing efficiently if quick convergence to a homogeneous concentration distribution is realized, i.e., to the situation where for all $(x,y) \in \Omega$ $c(x,y,T_F) = \bar{c} := \int_\Omega c dA / A_\Omega$, where $A_\Omega = \int_\Omega dA$, and T_F is a chosen final time.

In most dynamical mixers a limited number M of mechanical motions σ is available, each of which creates a different flow. We consider a fixed time interval of length $\triangle t$ and denote the mixing motion active from $t_k = k\triangle t$ to t_{k+1} as $\sigma_k \in \{1,2,\ldots,M\}$, where $k \in \{0,1,...,k_F-1\}$ and $k_F = T_F/\triangle t$. Consequently, over the time interval from 0 to T_F $\vec{v}(x,y,t)$ can be expressed as a concatenation of flows $\vec{v}_{\sigma_k}(x,y,t-t_k)$ associated with the applied motions, $\sigma_k \in \{1,2,...,M\}$ for $k \in 0,1,...,k_F-1$.

By spatial and temporal discretization and dividing the domain Ω into N cells Ω_i, with $i \in \{1,2,...,N\}$, and by using a small fixed time interval $\triangle t$, the mixing process can be modelled. The discretized concentration distribution $\mathbf{C}(t) = [C_1(t), C_2(t), ..., C_N(t)]^T$ is defined by the averaged concentration per cell, i.e. $C_i(t) = \int_{\Omega_i} c(x,y,t) dA / A_{\Omega_i}$, $A_{\Omega_i} = \int_{\Omega_i} dA$, which is considered at discrete times t_k. Given any admissible flow $\vec{v}_{\sigma_k}(x,y,t-t_k)$ at a time interval $[t_k, t_{k+1}]$, where $\sigma_k \in \{1,2,...,M\}$, the change in the concentration distribution $\mathbf{C}$ is described by the linear map

$$\mathbf{C}(t_{k+1}) = \mathbf{\Phi}_{\sigma_k}\mathbf{C}(t_k). \tag{4.1}$$

Here, $\mathbf{\Phi}_\sigma$, $\sigma \in \{1,2,....,M\}$, is the $N \times N$ mapping matrix [13, 12, 14]. Each entry Φ_{ij} (with $i,j \in \{1,2,...,N\}$ and $0 \leq \Phi_{ij} \leq 1$) describes the transport from cell j to cell i over a time interval $\triangle t$ when flow $\vec{v}_\sigma(x,y,t)$ is active. For each mixing motion σ and corresponding flow $\vec{v}_\sigma(x,y,t)$, the matrix $\mathbf{\Phi}_\sigma$ can be calculated [12, 15, 16]. Note that although the spatial discretization introduces numerical errors, these can be modeled as a diffusive effect. For the typically studied flows, numerical diffusion analysis [17] shows that the error is almost negligible for $N > 10^3$ and

$M > 10^5$. The model in Eq. 4.1 is a *switching dynamical system* [18], as the system switches between different (discrete-time) dynamics dependent on which flow σ_k is activated on the interval $[t_k, t_{k+1}]$. Any sequence of flows over $[0, T_F]$ is now defined by a switching sequence $\boldsymbol{\sigma} = (\sigma_0, \sigma_1, ..., \sigma_{k_F-1})$, with $\sigma_k \in \{1, 2, ..., M\}$ for $k \in \{0, 1, 2, ..., k_F - 1\}$.

Achieving a homogeneous concentration $\bar{c}$ for the whole region Ω within a fixed finite time T_F is identical to achieving a vanishing error, i.e. the difference in the homogeneous reference and achieved concentration defined by $\mathbf{e}_k := \mathbf{C}(t_k) - \bar{c}\mathbf{1}$ (where $\mathbf{1}$ is the unity vector) at the final discrete time $k = k_F$ is equal to zero. Using Eq. 4.1 and the identity $\boldsymbol{\Phi}_\sigma \bar{c}\mathbf{1} = \bar{c}\mathbf{1}$ [19], the concentration error evolution is described by the switching dynamical system

$$\mathbf{e}_{k+1} = \boldsymbol{\Phi}_{\sigma_k} \mathbf{e}_k. \tag{4.2}$$

The difference between $\mathbf{e}_k$ and the zero vector $\mathbf{0}$ at discrete time k can be measured by the intensity of segregation I_k [6], which is often applied as a measure for mixing quality. On a discretized domain it can be written as $I_k = \mathbf{e}_k^T \mathbf{Q} \mathbf{e}_k$. The entries of matrix $\mathbf{Q}$ are $Q_{ii} = A_{\Omega_i}/(A_\Omega \bar{c}(1-\bar{c}))$ and $Q_{ij} = 0$ if $i \neq j$. Note that I_k is zero if and only if $\mathbf{e}_k = \mathbf{0}$.

Under these conditions, efficient mixing is equivalent to finding a sequence $\boldsymbol{\sigma}$ of flows that minimizes the intensity of segregation I_{k_F} at the final time. As this is a non-convex optimization problem with the number of possible sequences being M^{k_F}, finding an optimal sequence is computationally intractable in real-time. As a consequence, a realistic objective is to find a suboptimal sequence that leads to a small I_{k_F}. In previous works on aperiodic mixing [3, 7, 6], the minimum error method has been proposed, which chooses at each time t_k the motion that minimizes the intensity of segregation at the next time instant I_{k+1}, leading to a sequence $\boldsymbol{\sigma}^{\text{min.error}}$. However, due to the perspective of switching dynamics, it is now known that this (greedy) approach does not necessarily lead to good mixing performance, might be far from optimal, and certainly is not guaranteed to outperform a given periodic protocol (as will be shown in the simulations in Fig. 4.3).

The new perspective on mixing problems through the switching dynamical system in Eq. 4.2 enables the application of the rollout optimization methods [20]. Starting with any initial (often periodic) base sequence $\boldsymbol{\sigma}^{\text{base}}$ (of length k_F), the rollout method constructs a sequence $\boldsymbol{\sigma}^{\text{rollout}}$ that achieves a value for

the intensity of segregation I_{k_F} that is guaranteed to be never worse than the intensity of segregation for the sequence $\boldsymbol{\sigma}^{\text{base}}$ but typically is significantly smaller [20]. Moreover, the method is computationally efficient and applicable in real-time.

To explain the rollout method, we consider a given base sequence $\boldsymbol{\sigma}^{\text{base}}$ and a given fixed lookahead horizon H, where $0 < H < k_F - 1$. For time t_k we define the set $\mathcal{I}_k$ consisting of all the sequences $\boldsymbol{\sigma} = (\sigma_k, \sigma_{k+1}, ..., \sigma_{k_F-1})$ of length $k_F - k$ that begin with H free variables $\sigma_k, \sigma_{k+1}, ..., \sigma_{k+H-1}$, followed by the tail of length $k_F - k - H$ dictated by the base sequence $\boldsymbol{\sigma}^{\text{base}}$. The mixing motions σ_k in $\boldsymbol{\sigma}^{\text{rollout}} = (\sigma_0, \sigma_1, ..., \sigma_{k_F-1})$ are found by iteratively minimizing the intensity of segregation I_{k_F} at the final time T_F over all sequences $\boldsymbol{\sigma}^k \in \mathcal{I}_k$ given the predicted value of e_k using the model in Eq. 4.2. Starting with $k = 0$, by using Eq. 4.2 and the given initial concentration $\mathbf{e}_0$, $\mathbf{e}_{k_F}$ is computed for every sequence in $\mathcal{I}_0$. The sequence that leads to the smallest I_{k_F} is denoted by $\boldsymbol{\sigma}^{0,*}$. Now the first variable in $\boldsymbol{\sigma}^{0,*}$ is σ_0 and chosen to be the first variable σ_0 of $\boldsymbol{\sigma}^{\text{rollout}}$. The other variables σ_k in $\boldsymbol{\sigma}^{\text{rollout}}$ are iteratively found for each time step k by computing $\mathbf{e}_k$ based on the already known variables of $\boldsymbol{\sigma}^{\text{rollout}}$: $(\sigma_0, \sigma_1, ..., \sigma_{k-1})$ and the model in Eq. 4.2. Next $\mathbf{e}_{k_F}$ and I_{k_F} are computed for each sequence in $\mathcal{I}_k$ giving the sequence $\boldsymbol{\sigma}^{k,*}$ that minimizes I_{k_F} and thereby the next variable σ_k of $\boldsymbol{\sigma}^{\text{rollout}}$.

This algorithm can be summarized as

Algorithm 4.3.1 *Given is H, $k_F - 1$, $\mathbf{e}_0$, and $\boldsymbol{\sigma}^{base}$.*
1. Initialize $k = 0$.
2. Compute the set $\mathcal{I}_k$ with all sequences $\boldsymbol{\sigma}^k = (\sigma_k, \sigma_{k+1}, ..., \sigma_{k_F-1})$.
Each sequence $\boldsymbol{\sigma}$ begins with H free variables $\sigma_k, \sigma_{k+1}, ..., \sigma_{k+H-1}$, followed by a tail of length $k_F - k - H$ which is the first part of the base sequence $\boldsymbol{\sigma}^{base}$.
3. Compute cost I_{k_F} at T_F for each $\boldsymbol{\sigma}^k \in \mathcal{I}_k$.
4. Find $\boldsymbol{\sigma}^k_{min} \in \mathcal{I}_k$ for which I_{k_F} is minimal.
5. Choose the first entry $\sigma_k^{rollout}$ of $\boldsymbol{\sigma}^k_{min}$ to be k-th entry of $\boldsymbol{\sigma}^{rollout}$
6. Stop if $k = k_F - 1$, otherwise $k = k + 1$ and go to step 2.

The obtained *open-loop* rollout sequence $\boldsymbol{\sigma}^{\text{rollout}} = (\sigma_0^{\text{rollout}}, \sigma_1^{\text{rollout}}, \ldots, \sigma_{k_F-1}^{\text{rollout}})$ depends on the initial concentration distribution $\mathbf{e}_0$ and the mapping matrices. The sequence $\boldsymbol{\sigma}^{\text{rollout}}$ is computed a priori. However, model uncertainty, initial conditions, and noise may lead to differences between the computed $(\mathbf{e}_0, \mathbf{e}_1, \ldots, \mathbf{e}_{k_F})$ and the real $(\overline{\mathbf{e}}_0, \overline{\mathbf{e}}_1, \ldots, \overline{\mathbf{e}}_{k_F})$ evolution, and hence higher than expected I_{k_F}. This can be compensated for if the concentration distribution is measured in real-time.

In that case the *closed-loop* rollout method can be used to calculate every motion σ_{k+1} as a function of the measured concentration error $\overline{\mathbf{e}}_k$. This can be done online during the time interval $[t_k, t_{k+1}]$. Feedback of the measured concentration errors can enhance mixing significantly.

4.4 Journal bearing flow experiments

To validate the proposed methodology, experiments and simulations have been carried out on a journal bearing flow (JBF) setup [12], shown in Fig. 6.2, consisting of two rotating eccentric cylinders, with radii r_{in} and $r_{\text{out}} = 37.5 \cdot 10^{-3}$ m and $r_{\text{in}} = 12.5 \cdot 10^{-3}$ m. In between the cylinders is a Newtonian fluid (Polydimethylsiloxane, hydroxy terminated) with a viscosity of $\nu \approx 20 \cdot 10^{-3}$ m/s^2. The two cylinders can rotate in both directions at a fixed angular velocity $V_{\text{out}} = \pi/20$ rad/s and $V_{\text{in}} = 3\pi/20$ rad/s. Each time interval $\triangle t$ only one of these four actions is performed, giving four different flows/mixing motions $\sigma_k \in \{1, 2, 3, 4\}$. The resulting Reynolds number is $Re \approx 0.0175$ and hence the flow is a Stokes flow. We select $\triangle t = 20$ s and discretize the domain in $N = 6 \cdot 10^4$ cells. The four (sparse) mapping matrices describing the redistribution effect of the four flows are computed according to [12].

In the experiments the objective is to redistribute a droplet of dye by choosing a mixing sequence $(\sigma_0, \sigma_1, \ldots, \sigma_{k_F-1})$, with $\sigma_k \in \{1, 2, 3, 4\}$, $k \in \{0, 1, \ldots, k_F - 1\}$, over a finite time $T_F = 600$ s. As $k_F = T_F/\triangle t = 30$, this results in a sequence $\sigma = (\sigma_0, \sigma_1, ..., \sigma_{29})$. A camera underneath the setup measures the concentration evolution $\overline{\mathbf{C}}_k$ by correlating the light intensity in each pixel to concentration. This leads to the corresponding measured concentration error $\overline{\mathbf{e}}_k := \overline{\mathbf{C}}_k - \bar{c}\mathbf{1}$ and the corresponding measured intensity of segregation $\overline{I}_k = \overline{\mathbf{e}}_k^T \mathbf{Q} \overline{\mathbf{e}}_k$. Starting from an identical initial distribution, the simulated and measured concentration distributions evolutions show a comparable spatial distribution, see Fig. 4.2. In a small number of cells reflections cause a difference between the measured and actual concentration, and hence a difference between I_k and $\overline{I}_k$. In addition, material diffusion, which is neglected in the mapping matrix, smoothes concentration gradients in the experiments (as can be seen in Fig. 4.2).

To show the relevance of the rollout approach compared to existing works, in Fig. 4.3 the evolution of the intensity of segregation I_k is computed for one initial condition $\mathbf{e}_0$ and three different mixing strategies: a periodic sequence $\boldsymbol{\sigma}^{\text{periodic}}$, a sequence $\boldsymbol{\sigma}^{\text{min.error}}$ computed by the minimum error method [6], and the rollout

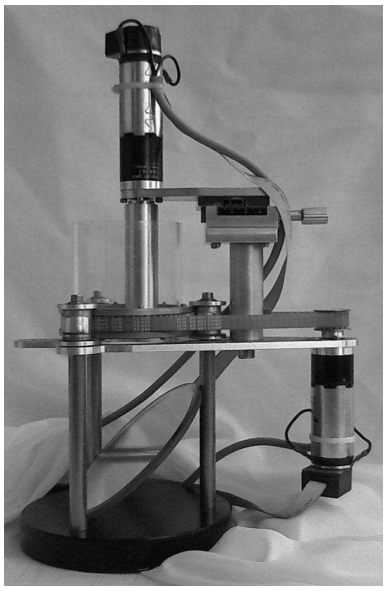

Figure 4.1: The journal bearing flow (JBF) setup. A highly viscous fluid is transported in between two rotating eccentric cylinders. The concentration of the colored dye in the fluid is derived from camera images recorded via the diagonal mirror.

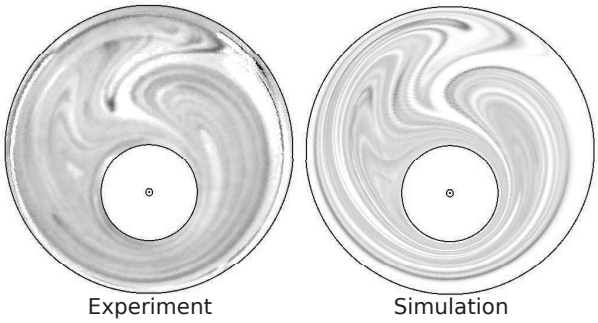

Figure 4.2: A 2D view of the concentration in the JBF. Starting from the same initial concentration, the experimental concentration distribution $\overline{\mathbf{e}}_k$ (left) and the computed concentration $\mathbf{e}_k$ (right) spatially coincide at $k = 22$, showing that the mapping matrices are predicting correctly.

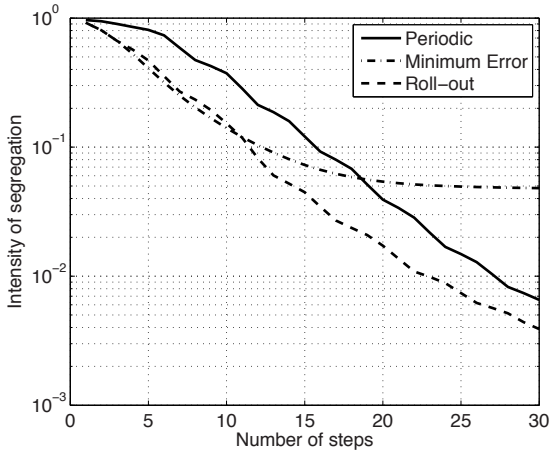

Figure 4.3: Simulations of a periodic (full line), a minimum error (dashed), and a rollout (dash dotted) sequence and the resulting I_k. The rollout sequence is performing best (achieving the lowest I_{k_F}) and the minimum error sequence performs worse than the periodic sequence. The periodic sequence consists of alternatingly a clockwise rotation of 2π rad of the outer cylinder and a clockwise rotation of 6π rad of the inner cylinder.

sequence $\boldsymbol{\sigma}^{\text{rollout}}$, which uses $\boldsymbol{\sigma}^{\text{periodic}}$ as base sequence. Not only does Fig. 4.3 show that the rollout sequence indeed leads to a lower I_k than $\boldsymbol{\sigma}^{\text{periodic}}$, it also significantly outperforms $\boldsymbol{\sigma}^{\text{min.error}}$. In addition, $\boldsymbol{\sigma}^{\text{periodic}}$ is significantly outperforming $\boldsymbol{\sigma}^{\text{min.error}}$, providing evidence to the earlier statement that minimum error might be far from optimal.

To study the sensitivity of several methods to initial condition uncertainty, for 25 slightly different initial conditions $\mathbf{e}_0$ we computed the evolution $\mathbf{e}_k$ for three different kind of sequences: a fixed periodic base sequence $\boldsymbol{\sigma}^{\text{periodic}}$, a sequence $\boldsymbol{\sigma}^{\text{rollout}}$ computed by the rollout algorithm as a function of one $\mathbf{e}_0$, and a closed-loop rollout sequence $\boldsymbol{\sigma}^{\text{rt}}$ where knowledge of the simulated $\mathbf{e}_k$ is used to compute σ_{k+1}. The mean intensity of segregation (averaged over all 25 simulations) are for $\boldsymbol{\sigma}^{\text{periodic}}$ $9.7 \cdot 10^{-3}$, for $\boldsymbol{\sigma}^{\text{rollout}}$ $5.1 \cdot 10^{-3}$, and for $\boldsymbol{\sigma}^{\text{rt}}$ $3.9 \cdot 10^{-3}$ with a standard deviation of $3.2 \cdot 10^{-3}$, $1.5 \cdot 10^{-3}$, and $1.8 \cdot 10^{-4}$, respectively. These simulations show that the rollout method (especially when applied in feedback) does not only lead to a lower I_{k_F} and thus better mixing, but also to a reduced sensitivity for uncertainties in the initial condition.

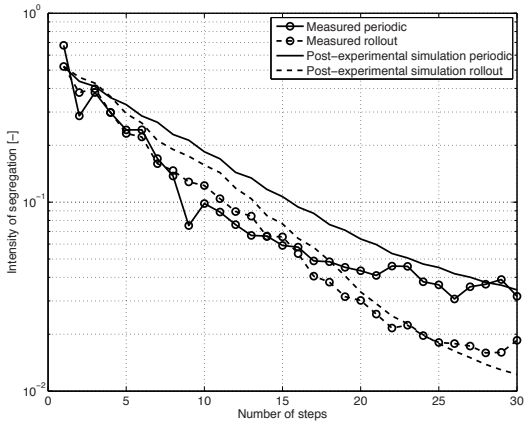

Figure 4.4: A comparison between experiments (lines with circles) with a periodic sequence $\boldsymbol{\sigma}^{\text{periodic}}$ (where alternatingly the outer cylinder is rotated clockwise π rad and the inner cylinder 3π rad) and a real-time closed-loop rollout sequence $\boldsymbol{\sigma}^{\text{rt}}$. Rollout is clearly performing better than the periodic sequence. To show that this is not due to the possible measurement errors, post-experimental simulations using the experimental sequences have been carried out (line and dashed line). These simulations confirm that rollout indeed results in a significantly lower I_{k_F} than the periodic sequence.

Experiments on the JBF setup have been carried out in which a periodic base sequence $\boldsymbol{\sigma}^{\text{periodic}}$ has been compared to an a priori computed open-loop rollout sequence $\boldsymbol{\sigma}^{\text{rollout}}$ and a real-time computed closed-loop rollout sequence $\boldsymbol{\sigma}^{\text{rt}}$, see Fig. 4.4. Although the observed and simulated concentration distributions are comparable just as in Fig. 4.2, there the measured $\overline{\mathbf{e}}_k$ and especially $\overline{I}_k$ are disturbed by measurement noise due to reflection. Therefore, also post-experimental simulations have been done, starting from the measured $\overline{\mathbf{e}}_0$. These simulations are based on $\boldsymbol{\sigma}^{\text{periodic}}$ and on the experimentally determined sequence $\boldsymbol{\sigma}^{\text{rt}}$. Based on both experimental and post-experimental simulations we can conclude that the rollout sequence $\boldsymbol{\sigma}^{\text{rt}}$ significantly outperforms the periodic base policy.

4.5 Discussion and conclusions

Typically, the flows studied in chaotic mixing are time-periodic. In this paper we advocate a new and general perspective on mixing using switching dynamical

systems. Using this novel perspective, the rollout method from switching dynamical systems is proposed to create aperiodic flow sequences that are analytically guaranteed to outperform any given periodic flow. Moreover, this approach can also be used for (real-time) feedback control of mixing. Simulations and experiments (in fact being the first experiments where theoretically derived feedback controllers for chaotic mixing have been validated) show that aperiodic switching sequences based on rollout, and especially state-dependent switching, obtained via the closed-loop rollout algorithm, lead to better mixing over a fixed finite time compared to periodic flows and flows found by the well-known minimum error method. In fact, we would like to emphasize that our analysis shows that the minimum error method can result in mixing sequences far from optimal. The closed-loop rollout is significantly less sensitive to differences in initial concentration distribution and disturbances than the periodic strategy. As shown in this contribution, this novel method can significantly decrease mixing times in laminar flows and seems especially suited for micro-mixing devices in which the flow can be actuated. The presented method could be used to open up new avenues such as the consideration of creating desired heterogeneous distributions, but also for control of other transport problems.

Bibliography

[1] H. Aref, J. Fluid Mech. **143**, 1 (1984).

[2] J.M. Ottino *The kinematics of mixing: Stretching, Chaos, and Transport* (Cambridge Univ. Press, 1989).

[3] M. Liu, F.J. Muzzio, and R.L Peskin, Chaos Soliton Fract. **4**, 869 (1994).

[4] S. Balasuriya, Phys. Rev. Letters **105**, 064501 (2010).

[5] S. Balasuriya and M.D. Finn, Phys. Rev. Letters **108**, 2444503 (2012).

[6] T.G. Kang, M.K. Singh, T.H. Kwon, and P.D. Anderson, Microfluid Nanofluid. **4**, 589 (2008).

[7] L. Cortelezzi, A. Adrover, and M. Giona, J. Fluid Mech. **597**, 199 (2008).

[8] B.A. Mosovsky, M.F.M. Speetjens, and J.D. Meiss , Phys. Rev. Letters **110**, 214101 (2013).

[9] O.M. Aamo, M. Krstic, and T.R. Bewley, Automatica **39**, 1597 (2003).

[10] G. Mathew, I. Mezic, S. Grivopoulos, U. Vaidya, and L. Petzold, J. Fluid Mech. **580**, 261 (2007).

[11] I.J. Couchman and E.C. Kerrigan, J. Process Contr. **20**, 1103 (2010).

[12] P.D. Anderson, O.S. Galaktionov, G.W.M. Peters, H.E.H. Meijer, and C.L. Tucker III, Int. J. Numer. Methods Fluids **40**, 189 (2002).

[13] R. Spencer and R. Wiley, J. Colloid Sci. **6**, 133 (1951).

[14] E.A.L.J. Limpens, Master Thesis, Eindhoven University of Technology, DCT 2007.017 (2007).

[15] M.K. Singh, O.S. Galaktionov, H.E.H. Meijer, and P.D. Anderson, Comput. Chem. Eng. **33**, 1354 (2009).

[16] O. Gorodetskyi, M. Giona, and P.D. Anderson, Phys. Fluids **24**, 073603 (2012).

[17] O. Gorodetskyi, PhD Thesis, Eindhoven University of Technology (2014).

[18] D. Liberzon *Switching in Systems and Control* (Birkhäuser, Boston, 2003).

[19] M.F.M. Speetjens, M. Lauret, H. Nijmeijer, and P.D. Anderson, Physica D **250**, 20 (2013).

[20] D.P. Bertsekas *Dynamic programming and optimal control* (Athena Scientific, Belmont, 2005).

Chapter 5

Sawtooth period locking with power modulation

M. Lauret, F. Felici, G. Witvoet, T.P. Goodman, G. Vandersteen, O. Sauter, M.R. de Baar, TCV team [1]

5.1 Abstract

Corroborating evidence is presented that the sawtooth period can follow the modulation frequency of an externally applied high power Electron Cyclotron wave source. Precise, fast and robust open loop control of the sawtooth period with a continuously changing reference period has been achieved. This period locking is not associated with the crash, but with the phase evolution of the inter-crash dynamics. This opens new possibilities of open loop control for physics studies and maybe for reactor performance control.

[1] Based on 'Demonstration of sawtooth period locking with power modulation in TCV plasmas', as has been published in Nuclear Fusion 52 (6), 062002, 2012.

5.2 Introduction

In tokamaks, plasmas with major radius R and the minor radius a are confined by toroidal and poloidal magnetic fields B_ϕ and B_θ. The safety factor $q(r)$ is defined as the number of toroidal turns a field line makes to complete one poloidal turn. Tokamak plasmas with $q < 1$ feature a periodic crash-like reorganisation of the plasma core known as the sawtooth instability [10]. The crashes form seed islands in the plasma. Neoclassical Tearing Modes (NTMs) can be driven unstable, as a consequence of which magnetic islands can grow [2]. These deteriorate the energy confinement [3] or lead to disruptions [2, 3]. The sawtooth period correlates with the effect of the sawtooth on the ambient plasma.

In plasmas without dominant fast particles, the sawtooth instability is triggered when the magnetic shear $s(r) = (r/q)\partial q/\partial r$ at $r(q = 1)$ exceeds a critical value [4, 2]. Control of the sawtooth period has been achieved using various high power actuators to either directly actuate the magnetic shear or the energetic ion distribution [2, 5, 15, 16, 8, 9]. A common method to influence the shear near $q = 1$ is to drive current with Electron Cyclotron Current drive (ECCD) near $q = 1$. Closed loop control of the sawtooth period, using steerable mirrors as launcher, has been shown experimentally on TCV [18] and Tore Supra [15]. A methodological controller design for these applications based on a control-relevant sawtooth model has been presented in [11]. In addition, actuation using Ion Cyclotron Resonant Heating (ICRH) and Neutral Beam Injection (NBI) of the ion distribution has been shown to effectively shorten or lengthen the sawtooth period [16, 8].

Ref. [9] demonstrated that on TCV the sawtooth period can be paced by gyrotron power modulation of the ECCD. Sudden removal of the stabilizing gyrotron power causes a crash shortly thereafter. Real-time measurement of the sawtooth crash is required for determining the start and stop of each following gyrotron pulse. The sawtooth was not 'simply locking' to the external modulation frequency. Simulations however show that for a range of power modulation periods and duty cycles (ratio between on time and total period), the sawtooth period can lock to the gyrotron power modulation period [12] i.e. the sawtooth period converges towards the modulation period. The locking experiments in [9] were shown to be outside the locking range [12]. This period locking is not due to the immediate forcing of a crash by the gyrotron pulse, but due to a nonlinear dynamical phenomenon, and therefore associated with the evolution of the q profile between crashes. A phase difference between the power switch-off and the

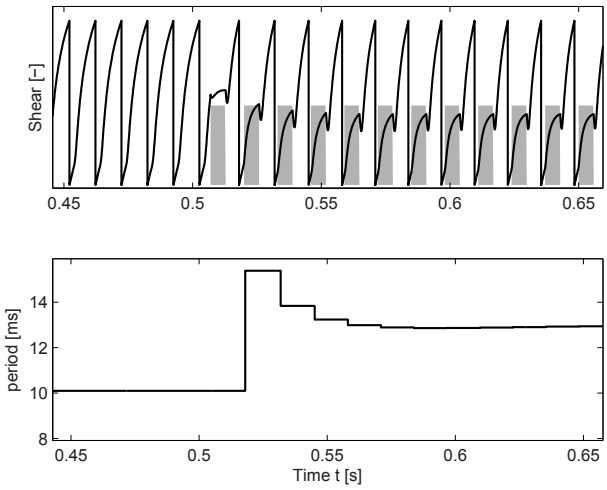

Figure 5.1: Simulation ([12]) of sawtooth locking with a power modulation duty cycle of 45%. The phase and period of the magnetic shear evolution (line in top box) adapt to the power modulation (grey). A phase difference between the power modulation and the crash remains. Consequently, the sawtooth period (bottom box) dynamically evolves towards the forcing period of 13 ms.

sawtooth crash exists, which evolves dynamically until a fixed value after which the sawtooth period is locked to the modulation period, see figure 5.1.

This Letter addresses the experimental demonstration of sawtooth period locking at TCV (with $R = 0.88$ m, $a = 0.234$ m, $\tau_E = 2$ ms, $\tau_{\text{current}} = 150$ ms), and answers the following questions: 1) Can locking be experimentally obtained? 2) Can this be used for sawtooth control?

5.3 Experimental results

The TCV tokamak has a real-time sawtooth crash detector which gives the sawtooth period. The optimal location of electron cyclotron wave deposition for maximizing the sawtooth period (just outside $q = 1$ [13]) in a limiter L-mode plasma with fixed EC mirror position and plasma shape (elongation $\kappa = 1.48$, triangularity $\delta = 0.326$) was determined by performing a scan of B_ϕ at constant q. The same mirror position and plasma shape are kept for the experiments reported

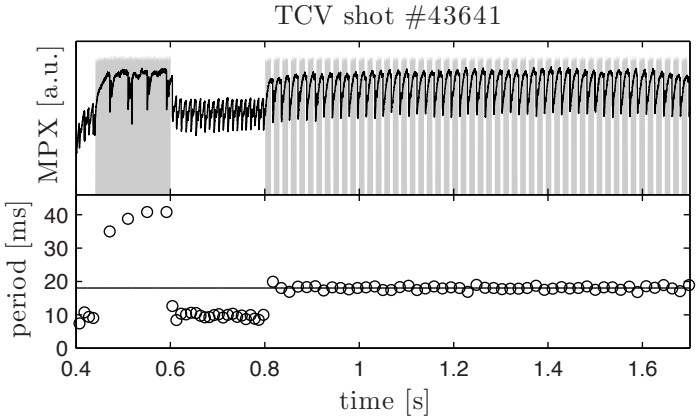

Figure 5.2: Sawtooth cycle as measured with central soft-X-ray channel (black line) and ECRH power of cluster A in grey (top-box). Measured sawtooth period (open circles) and power modulation period (solid line) in bottom box. At $t = 0.8$ s, the modulated gyrotron is enabled. Instantaneous locking is observed, which is maintained throughout the discharge

herein, thereby the absorption location is held constant, with $B_\phi = -1.22$ T and $I_\mathrm{p} = -0.288$ MA, giving $q(a) = 3.2$. The typical energy confinement time is a few ms and the typical current diffusion time is a few 100 ms. In all experiments, a constant gyrotron power of 500 kW is continuously deposited just outside of the $q = 1$ surface (but still within the radius for which EC deposition would yield the maximum sawtooth period) to increase the sawtooth period from the Ohmic period (2 ms) to 10 ms. Additional EC power is added at the same location to increase the sawtooth period beyond this baseline. At the beginning of each shot, the baseline sawtooth period, as well as the extent to which the period can be lengthened, is assessed by an initial phase of unmodulated injection followed by a phase during which the additional power is removed (cf. figures 5.2, 5.3, 5.4, 5.5, 5.7, 5.8 from $t = 0.4$ s to $t = 0.7$ s). Subsequently, the sawtooth locking experiment is commenced by injecting modulated power. The modulation period is always maintained constant long enough in order to investigate the locking of the sawtooth period. The power level, duty cycle (ratio of power 'on' to modulation period) and period of the modulating gyrotron can be varied independently during an experiment and are expected to affect whether locking can occur according to the model used in [12].

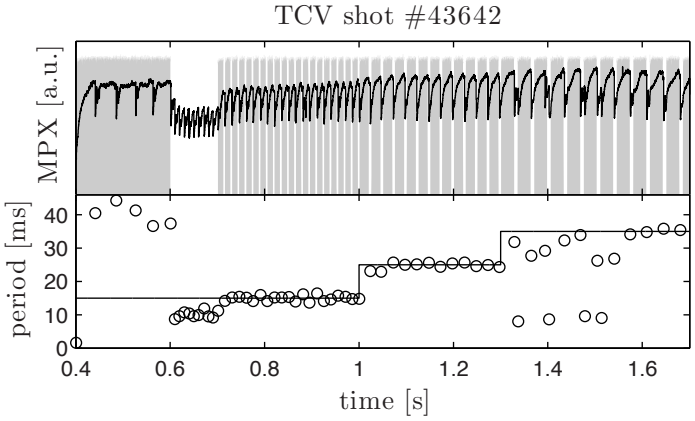

Figure 5.3: At $t = 0.7$ s, the modulated gyrotron is enabled. A variable modulation period is applied to which the sawtooth period eventually always locks successfully.

During the experiment shown in Fig. 5.2, the modulating gyrotron is started at 0.8 s and the power modulation period is 18 ms while its duty cycle is 70%. The sawtooth period, shown in the top-box of Fig. 5.2, immediately changes from its natural period of 10 ms to 18 ms and remains at that period for the rest of the experiment. In Fig. 5.3, the modulation frequency is varied in three steps from 15 ms, 25 ms and 35 ms at a duty cycle of 80%. The sawtooth period is locking within one sawtooth period to the modulation of 15 ms and 25 ms while it locks to 35 ms after transient behavior. Both figures demonstrate sawtooth locking at various periods and duty cycles. The counter-example of non-locking given in [9] is not a general result, and these measurements are in line with the modeling in [12].

The effect of the peak power of the wave form of the modulating gyrotron is shown in Fig. 5.4 (grey in top panel [a.u.]). This gyrotron has a fixed modulation period of 23 ms and a duty cycle of 70%. Power step-downs are preprogrammed from 450 kW to 325 kW to 200 kW. The sawtooth period locks almost immediately to the 23 ms modulation period at the moment the modulating gyrotron starts at 0.7 s. When the power steps down to 325 kW the sawtooth period unlocks and it takes 0.15 s to lock again. If the power is eventually stepped down to 200 kW, locking is completely lost. However, the sawtooth period does not become constant and attains values between 10 ms and 23 ms. This shows that whether locking occurs or not does indeed depend on the gyrotron power at fixed period and duty

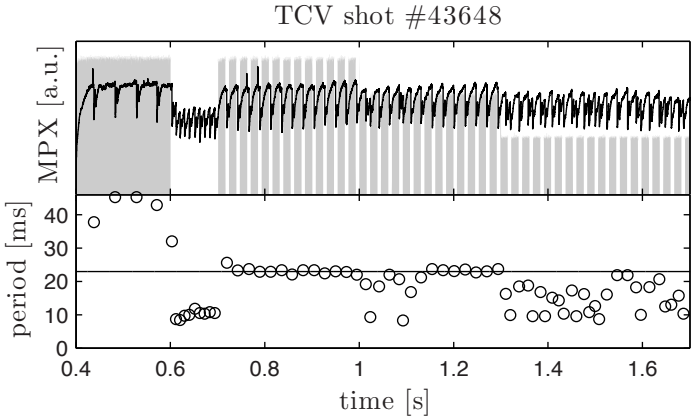

Figure 5.4: At $t = 0.7$ s, the modulated gyrotron is enabled. During the modulation phase, the power is stepped down from 450 kW (from 0.7 s to 1.0 s) 325 kW (from 1.0 s to 1.3 s) and 200 kW (from 1.3 s to 1.7 s). Note that this is reflected in quality and speed of locking. At 450, robust and instantaneous locking is observed. At 325 kW a transient is observed before locking is achieved. At 200 kW no locking is observed.

cycle.

Next, the duty cycle of the modulating gyrotron is changed during a shot. In the bottom-box of Fig. 5.5 the duty cycle can be seen to increase from 10% to 40%, to 60% and to 90%. The sawtooth period does not lock to the power modulation period of 20 ms for a duty cycle of 10% or 40%, but it does lock, after some time, for 60% and remains locked for 90% duty cycle. This demonstrates that locking depends on the duty cycle. The results of a number of locking experiments are summarized in Fig. 5.6 where squares indicate combinations of modulation period and duty cycle for which locking occurs and crosses indicate combinations for which locking does not occur. The line will be discussed later. The squares lie in a sizable, connected area in the bottom-right of the figure (the locking range) indicating that (a) locking is a robust phenomenon and (b) occurs more readily at higher duty cycles and relatively low modulation periods (although higher periods can also lock if the duty cycle is high enough). If the duty cycle is too small, EC cannot stabilize the period of the limit cycle. On the other hand, a very high duty cycle leads to longer sawtooth periods. This explains the crosses at the top left and bottom right of the figure.

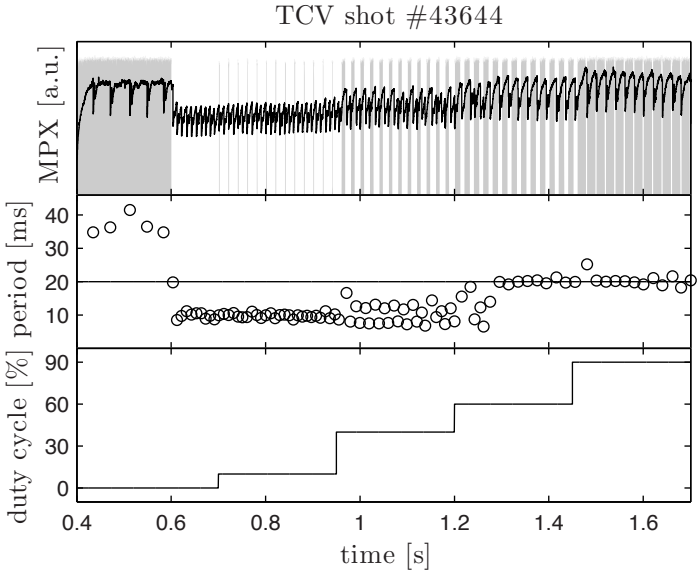

Figure 5.5: At $t = 0.7$ s, the modulated gyrotron is enabled. During the modulation phase, the duty-cycle is stepped up from 10% to 40%, to 60% and to 90%. Note that this is reflected in the quality and speed of locking. For 10% and 40% duty cycle, no locking is observed. For 60% and 90% locking occurs after a transient.

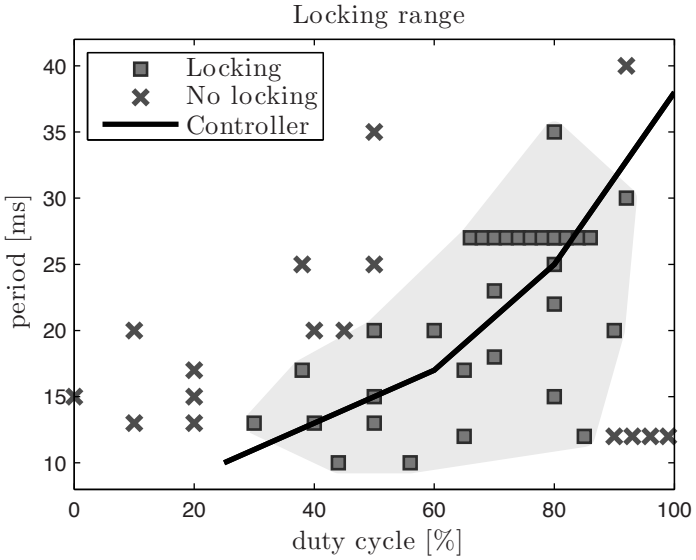

Figure 5.6: Locking of sawtooth period as function of duty cycle and power modulation period. Crosses indicate no locking, squares indicate successful locking. The open loop controller (results in Fig. 5.8) is based on the solid line.

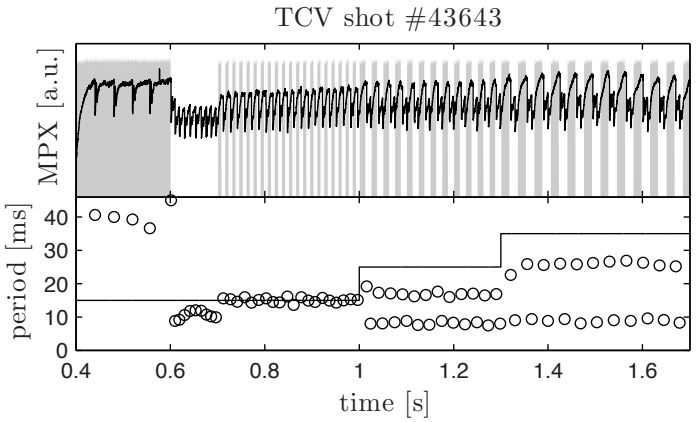

Figure 5.7: Note that at $t = 0.7$ s, the modulated gyrotron is enabled. During the modulation phase, the modulation period is stepped up from 15 ms (from 0.7 s to 1.0 s), 25 ms (from 1.0 s to 1.3 s) and 35 ms (from 1.3 s to 1.7 s). This is reflected in quality and speed of locking. At 15 ms, instantaneous locking is observed. At 25 and 35 ms no locking is observed. An alternating period is observed for which the sum of the two successive period matches the modulation period.

For example, Fig. 5.7 shows an experiment performed at constant 50% duty cycle along a vertical line in Fig. 5.6: the modulation period is set in steps to 15, 25 and 35 ms. The bottom box in Fig. 5.7 shows that locking occurs only for the smallest period (15 ms). However, for the other two modulation periods, the sawtooth period alternates between two values of which the smallest is the baseline value 10 ms and the sum of the values is equal to the modulation period: the power modulation can make the sawtooth period behavior regular, even when it is not locked. By drawing piecewise affine lines through the locking range (see black line in Fig. 5.6), combinations of duty cycle and period have been established for application in a open loop sawtooth period controller. These combinations of duty cycle and power modulation periods are preprogrammed to change together such that the whole trajectory (indicated by the black line in Fig. 5.6) lies within the locking range. The results, Fig. 5.8, show that the sawtooth period locks to the modulation period and follows the changing modulation period very well, even for the step in modulation period by a factor of 2 at 1.45 s. Therefore precise, fast and robust sawtooth period control can be achieved using the locking phenomenon. This control method has the advantage (compared with pacing [9] or aiming control [18, 12, 15]) that it does not need any real-time measurements of the sawtooth period, so it is immune to missing or noisy diagnostic measurements and signals derived from them (i.e. sawtooth detection). On the other hand, the locking region must first be known in order to design a successful controller. However, simulations can provide a very good estimate of the region as demonstrated by our results and the comparison with ref. [12].

5.4 Conclusions

Sawtooth locking experiments have been carried out successfully on TCV in which the sawtooth period follows the modulation period of an externally applied high power Electron Cyclotron wave source. The effects on the sawtooth period of power, modulation period and modulation duty cycle have been identified. A systematic comparison between simulations (as in [12]) and the experiment remains to be carried out, notably on the evolution of the current density profile.

The experimental dependence of locking on modulation frequency and duty cycle show a simple relation, that has been successfully used in an open loop sawtooth period controller. Open loop control of the sawtooth period with a continuously changing sawtooth period reference has been achieved. The sawtooth

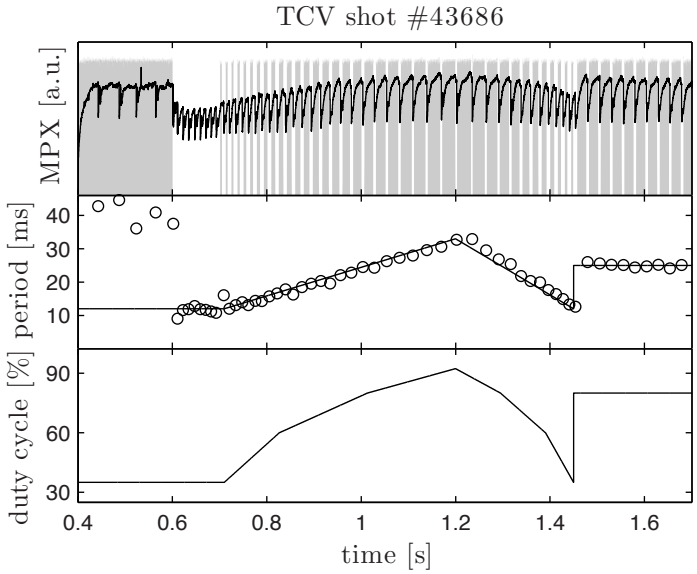

Figure 5.8: Power modulation period (solid line) and sawtooth period (circles) in middle box. Note that at $t = 0.7$ s, the modulated gyrotron is enabled. During the modulation phase, the modulation period and duty cycle are preprogrammed to achieve locking as in the solid line in Fig. 5.6. Consistent sawtooth period tracking is observed.

period shows little or no delay with respect to the changing requested modulation period. High precision, fast and robust sawtooth period control has been demonstrated between 10 and 35 ms, nearly the full range of achievable sawtooth periods for the chosen experimental conditions. This opens the possibility of open loop control for physics studies and maybe for performance control.

The locking range can be identified using modeling or exploratory experiments. For these experiments simulations were used. Real time diagnostics were not needed. Future work however will use the locking phenomenon in a feed-back loop. The modulation period and duty cycle can then be automatically modified to achieve locking. Of course, in such schemes prior knowledge of the locking range would not be needed, at the expense of requiring real time diagnostics.

Bibliography

[1] S. von Goeler *et al.*, Phys. Rev. Lett. **33**, 1201 (1974).

[2] I.T. Chapman, Plasma Phys. Controlled Fusion **53**, 013001 (2011).

[3] O. Sauter *et al.*, Phys. Rev. Lett. **88**, 105001 (2002).

[4] F. Porcelli *et al.*, Plasma Phys. Controlled Fusion **38**, 2163 (1996).

[5] T.C. Hender *et al.*, Nucl, Fusion **47**, S128 (2007).

[6] M. Lennholm *et al.*, Phys. Rev. Lett. **102**, 115004 (2009).

[7] J.P. Graves *et al.*, Phys. Rev. Lett. **102**, 065005 (2009).

[8] I.T. Chapman *et al.*, Phys. Plasmas **16**, 072506 (2009).

[9] T.P. Goodman *et al.*, Phys. Rev. Lett. **106**, 245002 (2011).

[10] J.I. Paley *et al.*, Plasma Phys. Controlled Fusion **51**,055010 (2009).

[11] G. Witvoet *et al.*, Nucl. Fusion **51**, 073024 (2011).

[12] G. Witvoet *et al.*, Nucl. Fusion **51**, 103043 (2011).

[13] C. Angioni *et al.*, Nucl. Fusion **43**, 455 (2003).

Chapter 6

Pacing control of sawtooth oscillations

M. Lauret, M. Lennholm, M.R. de Baar, and W.P.M.H. Heemels[1]

6.1 Abstract

In tokamak plasmas, the sawtooth oscillation (ST) and the edge-localized-mode (ELM) are characterized by a phase of a slow evolution of the plasma conditions to an instability criterion, followed by a crash-like instability that resets the plasma conditions. Typically, the crashes induce losses of heat and energetic particles and may also trigger secondary instabilities (NTMs). As the amplitude of the crash-like perturbation scales with the period between two crashes, period control of these oscillations is important for operations of large fusion facilities such as ITER and DEMO. In several present-day experimental facilities, a 'pacing control algorithm' has been successfully applied for controlling the sawtooth period and the ELM period. However, a formal analysis has been lacking so far, which therefore forms the objective of the present paper. For this purpose, a reset model for the sawtooth period is introduced and, after a proper transformation a nonlinear discrete-time system is obtained, which is used for the formal analysis of pacing control. By representing the model in a Lur'e (or Lurie) form, we can derive conditions under which global asymptotic stability of the closed-loop (pacing) period control system is guaranteed. Moreover, we will show that the system exhibits inherent robustness for model uncertainties. We envision that the analytical results in the area of pacing control of the sawtooth are also applicable to pacing period control of the ELM oscillation period.

[1]This chapter is to be submitted to Nuclear Fusion.

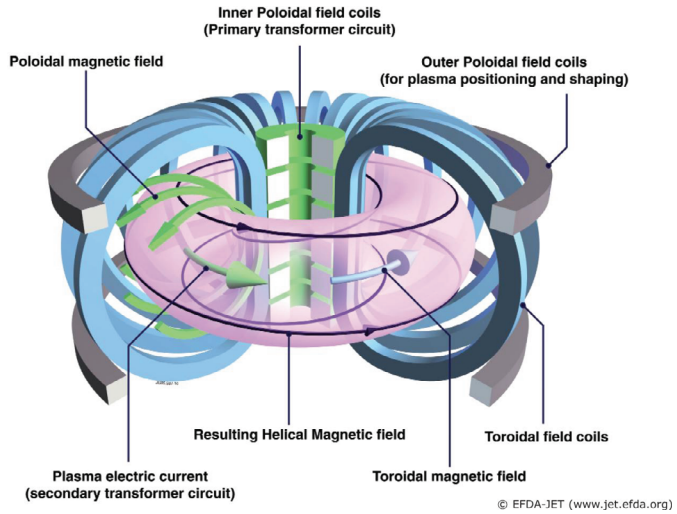

Figure 6.1: A typical plasma in a tokamak. The toroidal and poloidal magnetic field are indicated. Courtesy of EFDA-JET.

6.2 Introduction

Over the last decades nuclear fusion has been extensively studied in view of its potential as a clean and virtually limitless source of power. The purpose of the research is to find methods that facilitate the creation of conditions in the nuclear fusion fuel, the plasma, in which the hydrogen isotopes deuterium (D) and tritium (T) can fuse. In the DT reaction, significantly more energy is released per nucleus than in the typical fission reaction. At present, the tokamak is the most promising nuclear fusion reactor concept. A tokamak consists of a toroidal vacuum chamber in which the hot, electrically conductive, plasma is confined with magnetic fields. The magnetic field consists of a toroidal B_ϕ and a poloidal component B_θ, as is shown in Figure. 6.1. The existing tokamaks are too small to produce net fusion power. ITER, the tokamak that is presently constructed in the South of France, is designed to produce net energy. For successful ITER operation, feedback control of several processes within the plasma and the magnetic field need to be effectively implemented. The evolution of the magnetic field and its coupling to the plasma on the macro-scale is well described by the magnetohydrodynamic (MHD) equations, a system of nonlinear partial differential equations that follow from the combination of the Lorentz force balance, the Maxwell equations and the Navier-Stokes

equations. The control problems associated with the diffusive evolution of the distributions of pressure and current density (a.k.a. profile control) can be reduced to a simpler diffusion partial differential equation. Distributed controllers for this system have been derived and rigorously analysed from different control theoretical perspectives [1, 2, 3, 4]. Some profile control methods have been implemented and experimentally tested. In addition, a family of nonlinear oscillations exists in the plasma in which the profile evolution is limited by a crash-like reset event which is typically the consequence of nonlinear, resistive MHD activity. The sawtooth oscillation [10] and the edge-localized-mode (ELM) oscillation are the most relevant examples. The sawtooth oscillation is a periodic relaxation oscillation of all the relevant plasma variables (e.g. temperature, density, and pressure) in the center of the plasma. When a criterion for instability is met, the magnetic field in the centre reconnects in a crash-like event, causing a variation in a number of the core plasma parameters. The rapid variation of the magnetic field potentially drives losses of energetic particles and can cause secondary instabilities (NTMs) that lead to magnetic islands that may even disrupt the plasma. As the sawtooth period τ_{per} on ITER is predicted to be several orders of magnitude larger than on the current tokamaks (around 50 seconds), reliable control of this sawtooth period τ_{per} is considered critical for successful operation of ITER. The control of NTMs has been successful, both theoretically [5, 6] and experimentally [7, 8] and also [9] and references therein. The ELM oscillation is that occurs at the edge of the plasma. As with the sawtooth, the ELM cycle is characterised by a slow evolution of the plasmas conditions until an instability criterion is met, after which a crash-like reset of the plasma conditions occurs. Subject to the experimental conditions, the ELM crashes are periodic or chaotic. The crashes are associated with high dynamic heat fluxes to the reactor wall. Notably long ELM crash periods are expected to cause severe damage, and ELM period control [11, 12] is considered important for ITER operations. Systematic sawtooth period controller design was done, but to our knowledge, no purely theoretical analyses have been carried out on ST period control or for ELMs. However, for sawtooth period control, several control approaches have been studied by a combination of theory and simulations: PID (proportional-integral-derivative) control [13] and extremum seeking control [14]. Earlier, also other experiments, with feedback control of the sawtooth period, have been performed [15, 16, 17, 18, 19]. All these experiments controlled the sawtooth period by controlling the precise location where power was deposited by means of electron/ion cyclotron resonance heating/current drive. Recently, an-

other perspective on sawtooth period control has emerged. Instead of changing the power deposition location, the location is fixed and the power itself is modulated in time. This approach has been successfully tested in experiments on TCV [20, 21] and FTU [22] and has also been simulated for TEXTOR and TCV conditions [24]. Recent simulations [23] show that power modulation can also be feasible for sawtooth control on ITER. The power modulation approach can be divided in two types: 1.) in [21, 23, 24] the period of the power modulation is chosen reasonably close to the natural sawtooth period. This results in period locking of sawtooth period, i.e. the sawtooth period τ_{per} adapts to the modulation period. The mode locking phenomenon is very common in nonlinear oscillations and can be used as an open-loop controller. Although open-loop control is not adaptable to changing circumstances, the absence of real-time measurements can be advantageous, especially in future DEMO tokamaks where making real-time measurements will be extremely difficult. 2.) Contrary to the former type, the second method, pacing control, uses a feedback loop. Immediately after each sawtooth crash the power is decreased to zero for a finite time τ_{set}, where $\tau_{set} \leq \tau_{per}$. For $t > \tau_{set}$, with time $t = 0$ set to zero at the moment of the sawtooth crash, the power is instantaneously increased to a constant value, for the time remaining until the next sawtooth crash. The power modulation is adapted according to the following linear feedback law [25]

$$\tau_{set,k} = \tau_{set,k-1} + K(\tau_{ref} - \tau_{per,k-1}), \tag{6.1}$$

where τ_{ref} is a (constant) desired reference period and $K \in \mathbb{R}$ a control parameter. The discrete time $k \in \mathbb{N}$ counts the number of sawtooth crashes, which corresponds to crash or reset times t_k, $k \in \mathbb{N}$. Note that in [25] there is also a feedforward term in the pacing control law to achieve faster convergence to τ_{ref}. Here, the feedforward term is neglected.

The contribution of this paper is twofold. First we show that the sawtooth period dynamics can be modeled by a simple reduced model. This model is a first order reset equation, which resembles an *integrate-and-fire* model (which is used as the simplest dynamical model of a neuron). Then the period dynamics is explicitly modeled as a nonlinear discrete-time map. When the pacing controller (a discrete-time control law) is applied to this map, a Lur'e system [26] appears. This implies that the system can be decomposed into a linear system with a static nonlinearity in negative feedback. The nonlinearity can be bounded by a sector and this leads to conditions for which the controlled system is globally exponentially

stable. Because of the robustness in this approach, the results hold even if the reduced model is just a coarse approximation of the real dynamics.

The structure of the remaining paper is as follows. In section 2, the sawtooth model is introduced. In section 3 that model is reduced to a reset model and in section 4 we will analyse pacing control. Finally, conclusions are drawn.

6.3 The sawtooth model

Before a model for the sawtooth period can be introduced, some characteristics of the magnetic field $\vec{B}(x,y,z,t)$ have to be explained. This field is defined on a torus (the vacuum chamber of the tokamak) and can be decomposed into a field in toroidal direction B_ϕ and a field in the poloidal plane B_θ, see Figure 6.1. The analysis of the magnetic field evolution becomes much simpler by making several assumptions: the field is axisymmetric and all the magnetic field lines are on the surface of a torus and all these torii (i.e. the *flux surfaces*, seen in Figure 6.2) are nested into each other, the torus has a large aspect ratio (the radius r_{pol} of the poloidal plane is much smaller than the distance R from the center of the tokamak to the plasma), and the poloidal plane is circular. Now, the evolution of the 3D magnetic vector field can be reduced to the evolution of a 1D axisymmetric scalar field: the q-profile. Under the mentioned assumptions the q-profile can be approximated by

$$q(r,t) = \frac{rB_\phi}{RB_\theta}, \tag{6.2}$$

where B_ϕ is assumed to be constant for simplicity. The q-profile $q(r,t)$ at radius r can be interpreted as the inverse winding number of the field lines that lie on the flux surface with radius r, as can be seen in Figure 6.3. Many instabilities in the magnetic field, and associated reconnection, occur at places where q is a strong rational number $m:n$, with $m,n \in \mathbb{N}$. For example, the NTMs typically occur at places where $q = 2:1$ or $3:2$, while the sawtooth crash originates at the $q = 1:1 = 1$ surface.

In the time between two sawtooth crashes, the q-profile evolves diffusively. According to the model of Porcelli et al. [27, 13], the exact moment that the sawtooth crash occurs depends on the shear

$$s(r,t) = \frac{r_{pol}dq}{qdr} = 1 - \frac{rdB_\theta}{B_\theta dr} \tag{6.3}$$

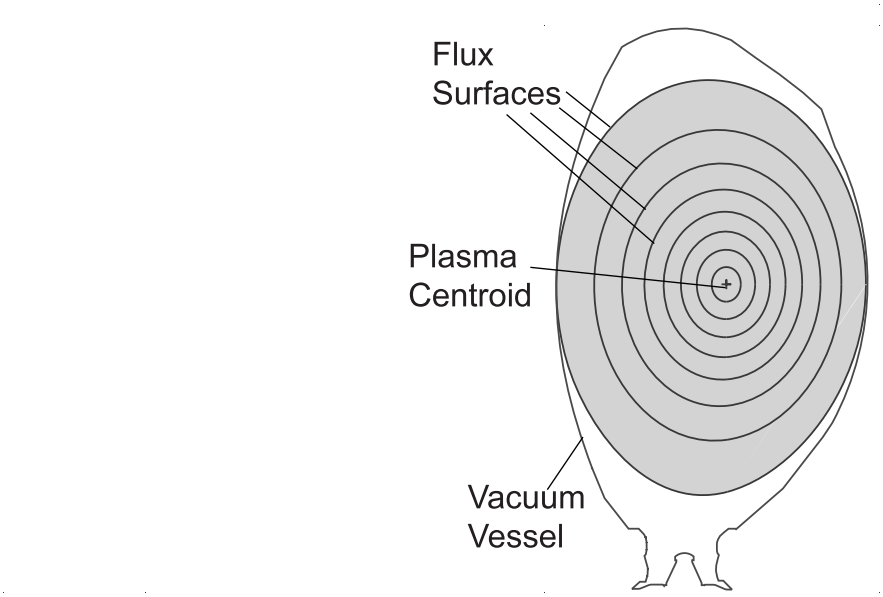

Figure 6.2: A schematic view on the flux surfaces in the poloidal plane.

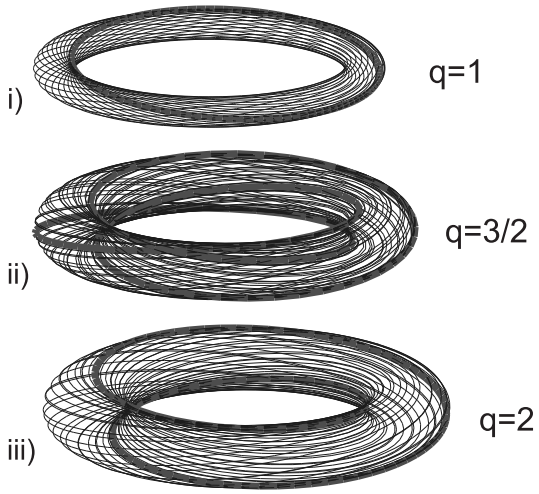

Figure 6.3: Three examples of flux surfaces. The q number indicates that, for any magnetic field line on the flux surface, the field line rotates around once in poloidal direction for every q toroidal rotations. The sawtooth oscillation is related to the behavior in the neighborhood of the $q = 1$ flux surface.

at the flux surface where $q = 1$. Therefore,

$$s_1(r(q=1),t) = \frac{rdq}{dr}. \tag{6.4}$$

As $q(r,t)$ evolves according to a diffusion equation of B_θ [13], also the shear $s_1(r(q=1),t)$ evolves diffusively. It is important to note that the q-profile, and hence $s(r,t)$, does not evolve diffusively towards a constant $q(r,t)$ profile, as would be expected for a diffusion equation, but towards a stationary profile like in Figure 6.4. This is due to the fact that it is the electric field that diffuses and this determines, by a complex relation, the q-profile. Moreover, the q-profile never reaches this stationary profile, because at the moment that the shear at $q = 1$ is equal to a critical value, $s_1(t) = c_3$, the magnetic field inside $r(q = 1)$ reconnects and most plasma variables suddenly drop, as can be seen in Figure 6.5. The critical shear c_3 actually is a function of time, but can often be assumed constant. This assumption is also applied here. In Figure 6.4 the q-profile is shown just before the crash (red) and just after the crash (blue). The stationary solution (dotted) of the diffusive process is clearly much lower than these, but is never reached, as the q-profile resets long before this solution is achieved.

6.4 A control-oriented model

In the former section the physics behind the sawtooth oscillation has been explained. Note that although the physics-based model of the sawtooth oscillation, as given in [13], is a complex partial differential equation, in Figure 6.5 the shear at $q = 1$ appears to evolve exponentially and in a repeatable way. Here, we will motivate a simplified model based on a simplification of the exposed physics.

Observe that Figure 6.4 and Figure 6.5 show that the shear at $q = 1$ increases towards a stationary but nonzero value. This evolution is modeled by a diffusion equation [13] with time and space dependent parameters and a reset, and in one cylindrical coordinate. As an approximation, we assume that the parameters are constant and one Cartesian coordinate z instead of a cylindrical coordinate r. We postulate that diffusion will eventually lead to a steady-state shear profile $s(z)_{ss} = c_0/c_1$, on a length scale l smaller than the minor radius r_{per}. This locally approximates the critical shear value c_3. Now, a simplified 1D diffusion equation can be introduced:

$$\frac{\partial s}{\partial t} = \frac{\eta}{\mu_0}\frac{\partial^2 s}{\partial z^2}, \tag{6.5}$$

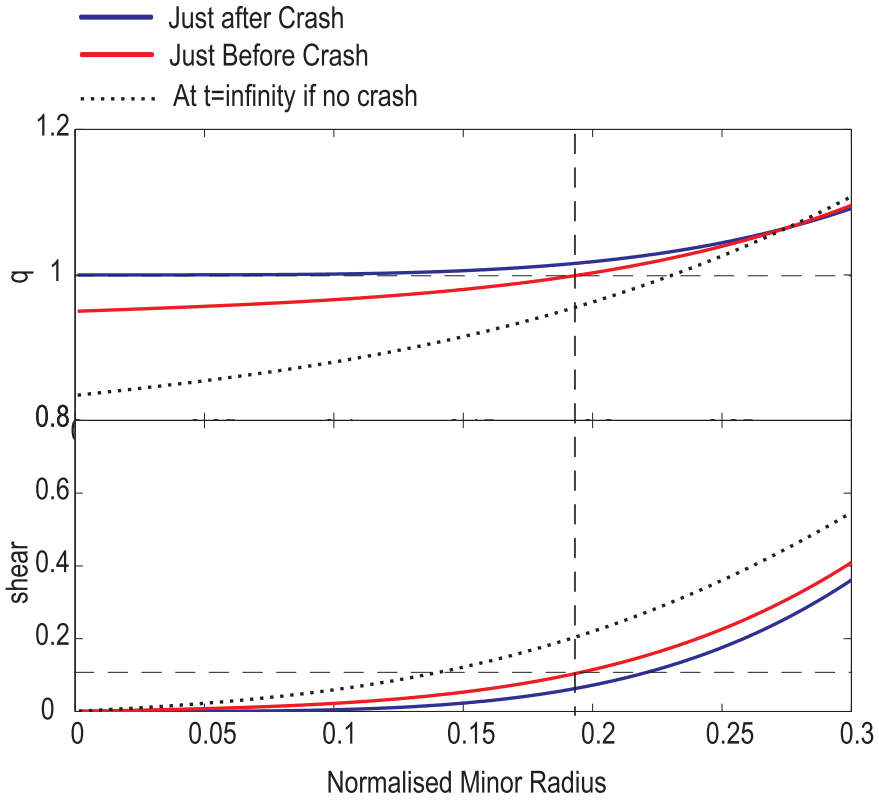

Figure 6.4: The evolution of the q-profile. Just before the crash, $r(q = 1) = 0.19$ and the shear at that location is equal to the critical shear c_3. Observe that the q-profile just before the crash is still far removed from the stationary state (at $t \to \infty$), which is never reached because of the sawtooth crash.

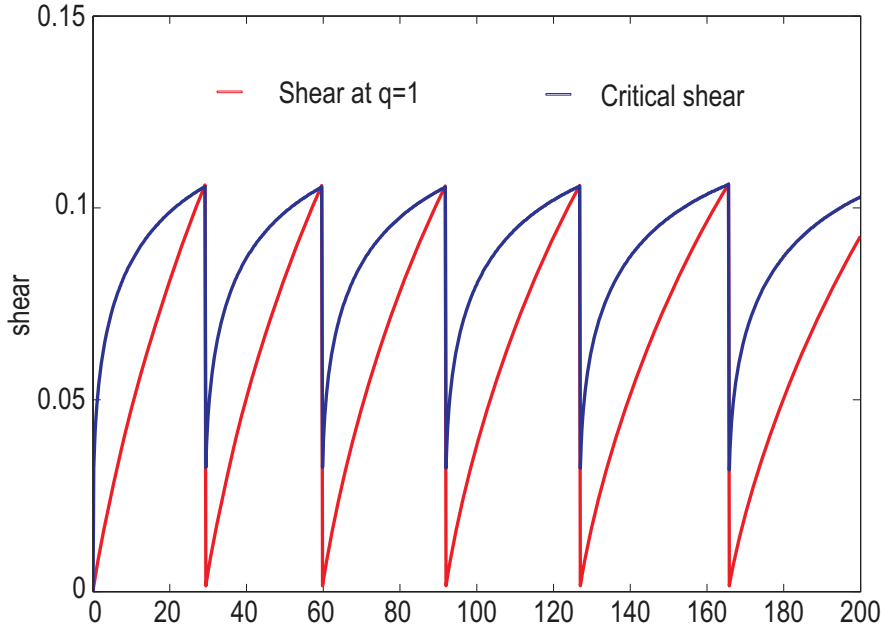

Figure 6.5: Simulations of the shear evolution at $r(q=1)$ and the critical shear c_3 as a function of time. Observe that the maximal and minimal value are approximately the same for every period. In this work, c_3 and c_2 are therefore assumed constant. To reproduce the shown sawtooth period the values have to be $c_3 = 0.105$ and $c_2 = 0.001$.

which mimics the diffusive shear evolution (caused by the diffusion of the q-profile) on the spatial domain $[0,l]$. With a constant resistivity η [13], the vacuum permeability $\mu_0 = 4\pi \cdot 10^{-7}$, and Dirichlet boundary conditions $s(0,t) = s(l,t) = c_0/c_1$. Hereby, the shear at $q = 1$ is modeled to evolve towards a nonzero value in steady-state. Therefore, the diffusion of $s(z,t)$ is relevant for computing the time (i.e. the sawtooth period τ_{per}) it takes the shear at $q = 1$ to reach the critical shear $c_3 < c_0/c_1$. Now, $s(z,t)$ can be approximated by using Fourier modes

$$s(z,t) = \sum_{i=1}^{N} \alpha_i(t) \sin(\frac{i\pi z}{l}) + \frac{c_0}{c_1}, \tag{6.6}$$

where $N \in \mathbb{N}$ is the truncation order. Moreover, note that for any given Fourier mode $s(z,t)_i = \alpha_i(t)\sin(\frac{i\pi z}{l})$ it holds that

$$\frac{\partial^2 s(z,t)}{\partial z^2} = -\alpha_i(t)\frac{i^2\pi^2}{l^2}\sin(\frac{i\pi z}{l}). \tag{6.7}$$

Thereby, substitution of the Fourier mode approximation into the diffusion equation leads to the time evolution of the shear:

$$s(z,t) = \sum_{i=1}^{N} \alpha_i(0) \exp\frac{-\eta\pi^2 i^2 t}{\mu_0 l^2} \sin(\frac{i\pi z}{l}) + \frac{c_0}{c_1}. \tag{6.8}$$

This shows that the coefficients of higher Fourier modes vanish very quickly because of the i^2 term. Therefore, we assume that the evolution of $s(z,t)$ is dominated by the evolution of the first Fourier mode $i = 1$. This is the slowest mode with the longest length scale. The amplitude of this mode evolves as a first-order system

$$\alpha_1(t) = \alpha_1(0)\exp(-\frac{\eta\pi^2}{l^2\mu_0}t). \tag{6.9}$$

This approximation is physically sensible, as it implies evolution on the diffusive time scale $l^2\mu_0/\pi^2\eta$, for the length scale l.

Assuming nonzero steady-state shear and truncating the associated diffusion equation to the slowest mode, the previous model reduction motivates that evolution of the shear at $q = 1$ is evolving as a first order system towards a nonzero value c_0/c_1. This can be written as

$$\dot{x} = c_0 - c_1 x + v, \tag{6.10}$$

where state x is the shear at $q = 1$ and where v is the first spatial Fourier mode of the input (by ECCD), $c_1 = \eta\pi^2/l^2\mu_0$, and c_0/c_1 is related to the steady state

of the shear (approximately $c_0/c_1 = 0.3$ in Figure 6.4). The error made by this truncated model for predicting the right crash time depends on which modes the crash introduces (the Fourier coefficients $\alpha_i(0)$ at the crash time) and on the ratio between the sawtooth period and the diffusive time scale. As the sawtooth period can be somewhat smaller than the diffusion time in experiments, it is possible that a few more Fourier modes are relevant for the shear evolution, but note that this quantitative error does not influence the qualitative dynamics and the truncation error can be partly compensated for by the choice of the 'effective diffusion coeffient' c_1.

Using these observations, the sawtooth crash can now be modeled as a reset condition. Once the shear-related state x equals the critical shear c_3, the profile and thereby x is reset to a smaller value c_2. Observe that under the circumstances of the simulation in Figure 6.5, the values are $c_2 = 0.001$ and $c_3 = 0.105$. Hence, assembly of these model components leads to the reset model

$$\begin{aligned} \dot{x} &= c_0 - c_1 x + v \\ x^+ &= c_2 \text{ when } x = c_3, \end{aligned} \tag{6.11}$$

with positive constants $c_1, c_2, c_3, c_4 > 0$ and an input variable v. The model (6.11), with $v = 0$, predicts an exponentially converging evolution of the shear towards a constant nonzero value c_0/c_1. The shear is reset before this steady-state value is reached, because $c_2 < c_3 < c_0/c_1$, leading to a periodic fast-slow oscillation. Observe that this is consistent with the evolution according to the simulation presented in Figure 6.5.

Remark 6.4.1 *The occurrence of fast particles can influence the MHD stability of the internal kink mode and thereby influence the sawtooth crash [27]. This contribution of fast particles could also be modeled by making the reset condition c_3 time-dependent, and in experiments [28, 29] $c_3(t)$ can be influenced by using another input, namely the ion cyclotron resonance heating (ICRH). Here, this effect will not be taken into account, but a similar analysis can in principle be carried out.*

The reduced reset model in (6.11) is suited for (pacing) control analysis. The pacing control setup, as discussed in the introduction, see (6.1), simplifies the admissible profile for the input v, as it assumes only two possible values for the

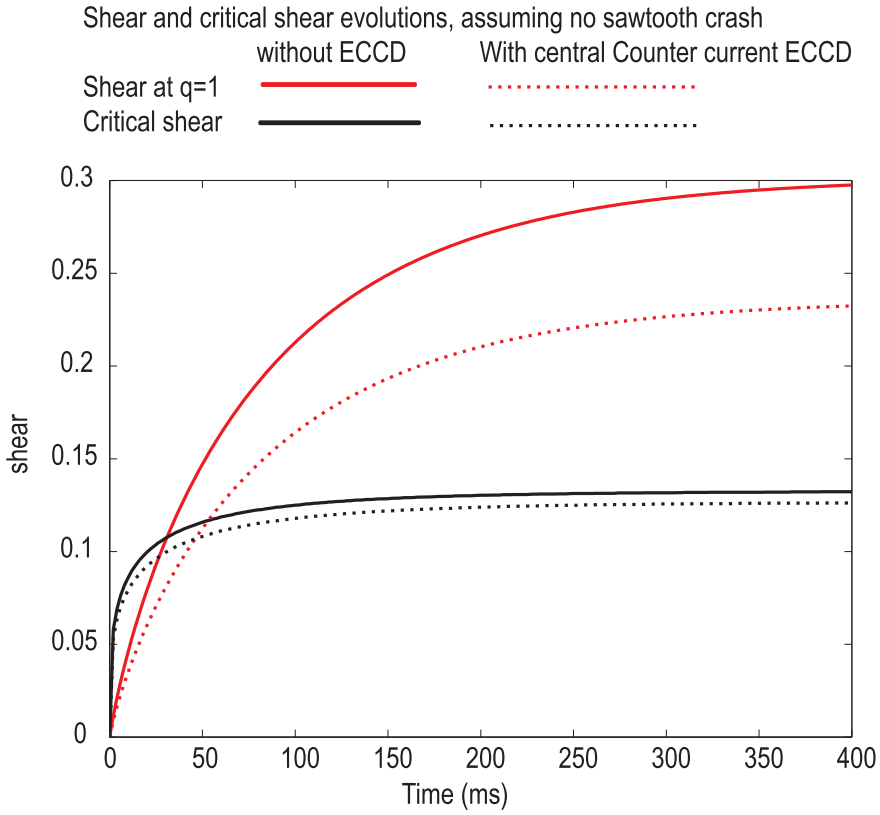

Figure 6.6: Evolution of the shear at $r(q = 1)$ and the critical shear, with (dotted line) and without (line) counter current ECCD. The current decreases the shear evolution, implying that $v(t)$ has a negative sign for these simulations.

input

$$v(\tau) = \begin{cases} 0, & \text{if} \quad 0 \leq \tau \leq \tau_{set} \\ v_{max}, & \text{if} \quad \tau_{set} < \tau, \end{cases} \tag{6.12}$$

with v_{max} the applied gyrotron power of the ECCD and τ a timer that starts at zero at the beginning of every sawtooth period. Hence, the only variable in the choice of the input signal v is τ_{set}. For the control analysis, the notation is changed to be conform with the control literature; the input is now denoted as $u = \tau_{set}$ and the output (i.e. the sawtooth period τ_{per}) is denoted as $y = \tau_{per}$. In fact, we are going to consider u and y on discrete times, labeled by $k \in \mathbb{N}$, and corresponding to the crash/reset times t_k, $k \in \mathbb{N}$. Hence, we are going to write u_k and y_k as the k-th control input and the k-th ouput (sawtooth period). The reference period in (6.1) becomes $r = \tau_{ref}$.

Remark 6.4.2 *Assuming pacing control (6.1) and (6.12), the model (6.11) can be rewritten formally in the hybrid system framework advocated in [30]. The flow dynamics are given by*

$$\dot{x} = \begin{cases} c_0 - c_1 x, & \textit{if} \quad 0 \leq \tau \leq u, \\ c_0 + v_{max} - c_1 x & \textit{if} \quad u < \tau \leq \tau_{per}, \end{cases} \tag{6.13}$$

$$\dot{\tau} = 1, \ \dot{u} = 0, \ \dot{s} = 0, \tag{6.14}$$

when $0 < x \leq c_3$. The variable s is redefined here to store the previous sawtooth period and the timer τ is tracking the time elapsed since the last reset. The jump dynamics is given by

$$\begin{aligned} x^+ &= c_2, \\ \tau^+ &= 0, \\ u^+ &= u + K(r - s), \\ s^+ &= \tau, \end{aligned} \tag{6.15}$$

when $x = c_3$. Here, u is assumed to adapt according to (6.1), and we assume for ease of exposition that $v_{max} > 0$. An interesting feature of the control problem for this hybrid system is that we are interested in the control of the time between resets, which is not often considered in the hybrid literature, see, e.g. [30].

To solve the problem of controlling the duration between two resets, we are going to compute the influence of the pacing time u_k on the sawtooth period y_k

in two steps. In particular, we are going to consecutively solve the two equations in (6.13) over the time interval $[0, u_k]$ and $(u_k, y_k]$, respectively. Solving (6.13) for $\tau \in [0, u_k]$ (and thus $t \in [t_k, t_k + u_k]$) leads to

$$x(\tau) = (c_2 - c_0/c_1)e^{-c_1\tau} + c_0/c_1. \tag{6.16}$$

At $\tau = u_k$ the state x is

$$x(u_k) = (c_2 - c_0/c_1)e^{-c_1 u_k} + c_0/c_1. \tag{6.17}$$

For $\tau \in [u_k, y_k]$ (and thus $t \in [t_k + u_k, t_{k+1}]$) the solution of (6.13) is

$$x(\tau) = e^{-c_1(\tau - u_k)}\left(x(u_k) - \frac{c_0 + v_{max}}{c_1}\right) \tag{6.18}$$

$$+\frac{c_0 + v_{max}}{c_1}. \tag{6.19}$$

Because $x(y_k) = c_3$ (note that $t_k + y_k = t_{k+1}$) by definition of the reset, it follows that

$$c_3 = e^{-c_1(y_k - u_k)}((c_2 - c_4)e^{-c_1 u_k} + c_6) + c_5 \tag{6.20}$$

with $c_4 := c_0/c_1$, $c_5 := (c_0 + v_{max})/c_1$ and $c_6 := c_4 - c_5$. Therefore, the sawtooth period y_k can be expressed explicitly as a stationary nonlinear map, see Figure 6.7, of u_k, i.e.

$$\begin{aligned} y_k &= \tilde{g}(u_k), \text{ with} \\ \tilde{g}(u_k) &= u_k - \frac{1}{c_1}\ln\left(\frac{c_3 - c_5}{(c_2 - c_4)e^{-c_1 u_k} + c_4 - c_5}\right). \end{aligned} \tag{6.21}$$

Note that the above derivation only makes sense when $u_k \geq 0$. In fact, we denote $\tilde{g}(0)$ as y_{min} as this is the smallest value of the period that can be realized (corresponding to maximal power $v(t) = v_{max}$ for all the time). Moreover, if we use $v(t) = 0$ all the time, then the system will experience a reset period denoted by y_{max}, the maximal period that can be realized. Hence, values of u_k outside the domain $[0, y_{max}]$ are meaningless and the corresponding reset periods y_k can also be realized for values of $u_k \in [0, y_{max}]$, $k \in \mathbb{N}$. Therefore, we use saturation of u_k when it is outside the domain $[0, y_{max}]$ and we modify the function $\tilde{g}$ to g given for $u_k \in \mathbb{R}$ by

$$g(u) = \begin{cases} y_{min}, & \text{if} \quad u < 0 \\ \tilde{g}(u), & \text{if} \quad 0 \leq u \leq y_{max} \\ y_{max}, & \text{if} \quad u > y_{max}. \end{cases} \tag{6.22}$$

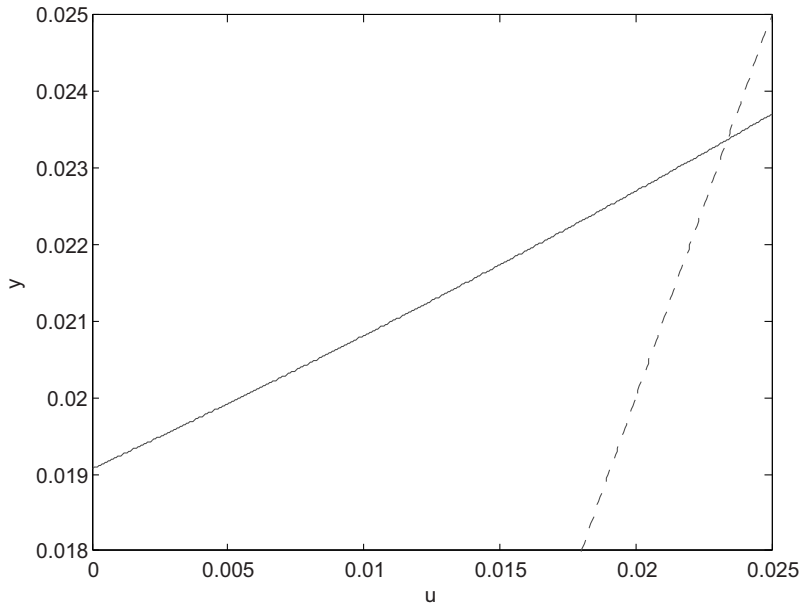

Figure 6.7: The almost linear input-output map from u_k to y_k (solid) and the diagional $u = y$ (dotted). For the parameters $v_{max} = 1, c_0 = 5, c_1 = 10, c_2 = 0.001, c_3 = 0.105$ the autonomous sawtooth period (with $u = 0$) is approximately $\tau_{per} = 20$ **ms**.

Hence, we obtain

$$y_k = g(u_k). \tag{6.23}$$

6.5 Pacing control analysis

Pacing control can now be analysed by substituting the pacing control law

$$u_{k+1} = u_k + K(r - y_k), \tag{6.24}$$

which results in the nonlinear discrete-time dynamics

$$u_{k+1} = u_k + K(r - g(u_k)). \tag{6.25}$$

Remark 6.5.1 *A few remarks are in order here. First, the measured sawtooth period y_k is needed in the pacing control law (6.24). In experiments, because of the high amount of measurement noise, the computation of the sawtooth period is not trivial and takes significant time [31]. Typically, one or two sawtooth periods are needed for TCV or TEXTOR circumstances. This time-delay effect is neglected here, but can be taken into account by using y_{k-n}, with a small $n \in \mathbb{N}$, in the pacing control law (6.1) instead of y_k. Second, the period dynamics in (6.25) is based on the simplified model (6.11), but the following approach remains valid when the period dynamics would be given by a different map g, as long as it satisfies certain properties. In fact, this robustness, that we will show below analytically in theorem 6.5.1, makes the pacing control a successful strategy as we will see.*

For the function g, for which an example was depicted in Figure 6.7 we adopt the following assumption.

Assumption 6.5.1 *The map $g : \mathbb{R} \to \mathbb{R}$ is monotonically increasing and in the region (y_{min}, y_{max}) it is strictly increasing. Moreover, g is continuously differentiable on (y_{min}, y_{max}) and there are constraints $d_{max} > d_{min} > 0$ such that for all $u \in (y_{min}, y_{max})$ it holds that the derivative $d_{max} > g'(u) > d_{min}$.*

We are now studying the (arbitrary) desired sawtooth period as a set-point of the controlled system. We restrict ourselves to the references periods within the physically reasonable interval

$$r \in \Omega_r := (y_{min} + \delta, y_{max} - \delta), \tag{6.26}$$

with a small $\delta > 0$ and $0 < y_{min} < y_{max}$. Clearly under the Assumption 6.5.1 the dynamics (6.25) have a unique equilibrium u_r^* (depending on r) for each $r \in \Omega_r$ satisfying $g(u_r^*) = r$.

To study the stability of the equilibrium u_r^* (for the input corresponding to the equilibrium r for the output y being the sawtooth period in view of (6.23)), we will study the error dynamics for the error defined as $e_k := u_k - u_r^*$, for $k \in \mathbb{N}$. This error dynamics is given by

$$e_{k+1} = e_k - K(g(u_r^* + e_k) - r). \tag{6.27}$$

As $g(u_r^*) - r = 0$, $e_k = 0$ is the equilibrium of (6.27). To study the stability, we assume that the initial value for the input is within the physically reasonable domain $[0, y_{max}]$, i.e.

$$u_0 \in [0, y_{max}] \tag{6.28}$$

and therefore

$$|e_0| = |u_0 - u_r^*| \leq y_{max}. \tag{6.29}$$

The domains on which e and u are considered are denoted by

$$\Omega_e = \{e \in \mathbb{R}|\ |e| \leq y_{max}\}, \tag{6.30}$$

$$\Omega_u = \{u \in \mathbb{R} | u \in (-y_{max}, 2y_{max})\}. \tag{6.31}$$

The system (6.27) can now actually be conceived as a Lur'e system [26, 32], i.e. the interconnection of a linear system in feedback with a nonlinearity (for each fixed r) in negative feedback. Due to the Assumption 6.5.1 and the use of the mean value theorem, we can show that there exist bounds $\underline{\gamma}$ and $\overline{\gamma}$ with $0 < \underline{\gamma} < \overline{\gamma}$ such that for all $e \in \Omega_e$ and $r \in \Omega_r$

$$\underline{\gamma} e \leq g(u_r^* + e) - r \leq \overline{\gamma} e. \tag{6.32}$$

In fact, the bounds $\underline{\gamma}$, $\overline{\gamma}$ can be related to d_{min} and d_{max} in Assumption 6.5.1. Hence, we have a Lur'e system with a sector bounded nonlinearity in the feedback path and the sector is given by $[\underline{\gamma}, \overline{\gamma}]$. As a consequence, we can rewrite the error dynamics (6.27) as the the error evolution

$$e_{k+1} = (1 - K\gamma_k)e_k \tag{6.33}$$

with $\gamma_k \in [\underline{\gamma}, \overline{\gamma}]$ for each $k \in \mathbb{N}$. Clearly, this system can be analysed by considering the Lyapunov function $V(e) = |e|$ and from this we obtain that if $|1 - K\gamma_k| < 1$ for

all $k \in \mathbb{N}$, then we have global exponential stability (GES) of the equilibrium $e = 0$ (corresponding to $u = u_r^*$ and $y = r$) and positive invariance of Ω_e and Ω_r for the respective variables, i.e. $e_k \in \Omega_e$ and $u_k \in \Omega_u$ for all $k \in \mathbb{N}$. Hence, this puts a condition on the gain K given by

$$0 < K < \frac{2}{\overline{\gamma}}. \tag{6.34}$$

If $g(u)$ satisfies (6.23) we have established the following result.

Theorem 6.5.1 *Consider the dynamics given by (6.25) and assume that the function g satisfies Assumption 6.5.1 and $r \in \Omega_r$. Then there exist $0 < \underline{\gamma} < \overline{\gamma}$ such that (6.32) holds for all $e \in \Omega_e$ and all $r \in \Omega_r$. If, in addition, K satisfies (6.34), then for any fixed value of $r \in \Omega_r$ the corresponding u_r^* is a GES equilibrium for the dynamics (6.25) for any $u_0 \in [0, y_{max}]$.*

Three remarks are in order. First of all recall that if u_k converges to u_r^*, then y_k converges to r, as desired. Second, interestingly, the result in Theorem 6.5.1 is independent of the actual value or r. So, if another value of $r \in \Omega_r$ and u_r^* is taken the system (6.25) will converge to this value as well and even slowly-varying time-dependent trajectories of r can be tracked. Third, even if g differs from the one that we computed in (6.21), but g still satisfies the conditions of the theorem, then the same conclusions regarding stability can be drawn. Hence, the theorem holds for any g satisfying Assumption 6.5.1, indicating the robustness of the pacing control strategy.

Remark 6.5.2 *If $0 < K < 1/\overline{\gamma}$, then it holds that e_k does not change sign over time and smaller positive invariant sets for e and u can be derived.*

Remark 6.5.3 *Note that we can even provide guarantees on the speed that $|u_k - u_r^*|$ converges to zero when k goes to ∞. The convergence factor is given by max $(|1 - K\overline{\gamma}|, |1 - K\underline{\gamma}|)$.*

6.6 Conclusions

The efficiency and safety of fusion plasmas in tokamaks often deteriorates by the occurrence of certain relaxation oscillations in the relevant fields. The period of the two most important oscillations, the sawtooth and the ELM oscillation, have

been successfully controlled in experiments by application of the so-called pacing control law. This controller depends only on one control parameter K. For the sawtooth oscillation a complex theoretical model exists, which consists of a linear parameter-varying partial differential equation and a state-dependent reset.

In this contribution we first motivated that the dynamics of this model can be reduced to a first order differential equation with reset. Secondly, the dynamics of the sawtooth period with pacing control is written as a nonlinear discrete-time system. This system can be perceived as a Lur'e system, i.e. a linear system with a static nonlinearity in the negative feedback path. By deriving the sector bounds to the nonlinearity (which is always possible for the nonlinearities at hand), as we showed we can prove that the complete system is globally asymptotically stable for a finite range of K. To the best knowledge of the authors, this is the first completely theoretical analysis resulting in conditions that guarantee that the control law will indeed guarantee global exponential stability of the desired reference sawtooth period.

This result not only implies that pacing control leads to a desired sawtooth period when the control parameter K is chosen appropriately. In addition , this result is independent of the chosen setpoint (desired period) and in fact, will also work for slowly varying setpoints. Moreover, the result is extremely robust for model perturbations and uncertainties. As long as the perturbed model satisfies the sector conditions and the monotonicity requirements, the methodology and results apply. This is essential, as the physical mechanisms that are responsible for the sawtooth oscillation are time-varying and can be more complex than the reduced model as used here.

As the ELM oscillation has recently been described by an ad hoc model (in a specific ELM regime) that has the same properties as our reduced sawtooth period model [25], we envision that the results for pacing control of the sawtooth period also apply for pacing control of the ELM period in the specific regime. Moreover, both the sawtooth and ELM model resemble the *integrate-and-fire* model, used in neuroscience as the most simple model for neurons. This suggests that our analysis of pacing control might also be applicable to period control of neurons. Several theoretical methods have been suggested in that field, but the simplicity and robustness of pacing might be beneficial for application in experiments.

For future work, the analysis of pacing control with a time-dependent reset condition $c_3(t)$, instead of constant c_3, is relevant for experiments. This is espe-

cially true when a second actuator (ICRH) is used that influences the evolution of $c_3(t)$. Furthermore, the analysis here depends on a reset model that incorporates only one Fourier mode of the original diffusion equation. Therefore, a more detailed analysis including a larger but finite number of Fourier modes in the reset model would certainly be of interest. As this model will still have a Lur'e form, the same type of stability analysis as reported here could be performed to study whether the addition of these (faster) modes is needed or not.

Bibliography

[1] F.B. Argomedo, E. Witrant, C. Prieur, S. Brémond, R. Nouailletas, J.-F. Artaud, "Lyapunov-based distributed control of the safety-factor profile in a tokamak plasma", *Nucl. Fusion*, vol. 53, 2013. 033005.

[2] M.D. Boyer, J. Barton, E. Schuster, T.C. Luce, J.R. Ferron, M.L. Walker, D.A. Humphreys, B.G. Penaflor, R.D. Johnson, "First-principles-driven model-based current profile control for the DIII-D tokamak via LQI optimal control", *Plasma Phys. Control. Fusion*, vol. 55, 2013, 105007.

[3] F. Felici, O. Sauter, "Non-linear model-based optimization of actuator trajectories for tokamak plasma profile control", *Plasma Phys. Control. Fusion*, vol. 54, 2012, 025002.

[4] E. Maljaars, F. Felici, M.R. de Baar, J. van Dongen, G.M.D. Hogeweij, P.J.M. Geelen, M. Steinbuch, "Control of the tokamak safety factor profile with time-varying constraints using MPC", submitted to *Nucl. Fusion*, 2014.

[5] B.A. Hennen, M. Lauret, G. Hommen, W.P.M.H. Heemels, M.R. de Baar, E. Westerhof, "Nonlinear control for stabilization of small neoclassical tearing modes in ITER", *Nucl. Fusion*, vol. 52, 2012, 063007

[6] W. Wehner, E, Schuster, "Control-oriented modelling for neoclassical tearing mode stabilization via minimum-seeking techniques", *Nucl. Fusion*, Vol. 52, 2012, 074003.

[7] B.A. Hennen, E. Westerhof, P.W.J.M. Nuij, J.W. Oosterbeek, M.R. de Baar, W.A. Bongers, A. Bürger, D.J. Thoen, M. Steinbuch, "Real-time control of tearing modes using a line-of-sight electron cyclotron emission diagnostic", *Plasma Phys. Control. Fusion*, vol. 52, 2010, 104006.

[8] F. Felici, T.P. Goodman, O. Sauter, G. Canal, S. Coda, B.P. Duval, J.X. Rossel and the TCV Team, "Integrated real-time control of MHD instabilities using multi-beam ECRH/ECCD systems on TCV", *Nuclear Fusion*, vol. 52, 2012, 074001.

[9] M. Marashek, "Control of neoclassical tearing modes", *Nucl. Fusion*, vol. 52, 2012, 074007.

[10] S. von Goeler, W. Stodiek, and N. Sauthoff, "Studies of Internal Disruptions and $m = 1$ Oscillations in Tokamak Discharges with Soft-X-Ray Techniques", *Phys. Rev. Lett.*, vol. 33, 1974, pp 1201.

[11] P.T. Lang, D. Frigione, A. Géraud, T. Alarcon, P. Bennett, G. Cseh, D. Garnier, L. Garzotti, F. Köchl, G. Kocsis, M. Lennholm, R. Neu, R. Mooney, S. Saarelma, B. Sieglin and JET-EFDA Contributors, "ELM pacing and trigger investigations at JET with the new ITER-like wall", *Nucl. Fusion*, vol. 53, 2013, 073010.

[12] L.D. Horton, G.D. Conway, A.W. Degeling, T. Eich, A. Kallenbach, P.T. Lang, J.B. Lister, A. Loarte, Y.R. Martin, P.J. McCarthy, H. Meister, J. Neuhauser, J. Schirmer., A.C.C. Sips, W. Suttrop and the ASDEX Upgrade Team, ITER-relevant H-mode physics at ASDEX Upgrade, *Plasma Phys. Control. Fusion*, vol. 46, 2004.

[13] G. Witvoet, M. Steinbuch, M.R. de Baar, N.J. Doelman, E. Westerhof, "Sawtooth period control strategies and designs for improved performance", *Nucl. Fusion*, vol. 52, 2012, 074005.

[14] J.J. Bolder, G. Witvoet, M.R. de Baar, N. Van De Wouw, M.A.M. Haring, E. Westerhof, N.J. Doelman, M. Steinbuch, "Robust adaptive control of the sawtooth instability in nuclear fusion", *Proc. of the American Control Conference*, 2012, pp. 5023-5028.

[15] M. Lennholm, L-G. Eriksson, F. Turco, F. Bouquey, C. Darbos, R. Dumont, G. Giruzzi, M. Jung, R. Lambert, R. Magne, D. Molina, P. Moreau, F. Rimini, J-L. Segui, S. Song, E. Traisnel, "Closed loop sawtooth period control using variable ECCD injection angles on Tore Supra", *Fusion Sci. Technol.*, vol. 55, 2009, pp. 45-55.

[16] J.P. Graves, I.T. Chapman, S. Coda, T. Johnson, M. Lennholm, J.I. Paley, O. Sauter, "Recent advances in sawtooth control", *Fusion Sci. Technol.*, vol. 59, 2011, pp. 539-548.

[17] I.T. Chapman, "Controlling sawtooth oscillations in tokamak plasmas", *Plasma Phys. Controlled Fusion* , vol. 53, 2011, 013001.

[18] J.I. Paley, F. Felici, S. Coda, T.P. Goodman, F. Piras and the TCV Team, "Real time control of the sawtooth period using EC launchers", *Plasma Phys. Control. Fusion*, vol. 51, 2009 , 055010.

[19] M. Lennholm, T. Blackman, I.T. Chapman, L.-G. Eriksson, J.P. Graves, D.F. Howell, M. de Baar, G. Calabro, R. Dumont, M. Graham, S. Jachmich, M.L. Mayoral, C. Sozzi, M. Stamp, M. Tsalas, P. de Vries and JET EFDA Contributors, "Feedback control of the sawtooth period through real time control of the ion cyclotron resonance frequency", *Nucl. Fusion*, vol. 51, 2011, 073032.

[20] T.P. Goodman, F. Felici, O. Sauter, J.P. Graves, "Sawtooth pacing by real-time auxiliary power control in a tokamak plasma", *Phys. Rev. Lett.*, vol. 106, 2011, 245002.

[21] M. Lauret, F. Felici, G. Witvoet, T.P. Goodman, G. Vandersteen, O. Sauter, M.R. de Baar, and the TCV team, "Demonstration of sawtooth period locking with power modulation in TCV plasmas", *Nucl. Fusion*, vol. 52, 2012, 062002.

[22] S. Nowak, P. Buratti, S. Cirant, B. Esposito, G Granucci, E. Lazzaro, D. Marocco, C. Sozzi, A.A. Tuccillo, E. Alessi, D. Frigione, G. Pucella, A. Romano, O. Tudisco and FTU Team, "Control of sawtooth periods by pulsed ECH/ECCD in the FTU tokamak", *Nucl. Fusion*, vol. 54, 2014, 033003.

[23] D. Kim T.P. Goodman, and O. Sauter, "Feedback control of the sawtooth period through real time control of the ion cyclotron resonance frequency", *Phys. Plasmas*, 2014, accepted for publication.

[24] G. Witvoet, M. Lauret, M.R. de Baar, E. Westerhof, and M. Steinbuch, "Numerical demonstration of injection locking of the sawtooth period by means of modulated EC current drive", *Nucl. Fusion*, vol. 51, 2011, 073024.

[25] F. Felici, J.X. Rossel, B.P. Duval, S. Coda, T.P. Goodman, Y. Martin, J-M. Moret, O. Sauter and the TCV Team, "Real-time control of the period of individual ELMs by EC power on TCV", *Nucl. Fusion*, vol. 53, 2013, 113018.

[26] A.I. Lur'e, "Some nonlinear problems in the theory of automatic control", *H.M. Stationery Off., London*, 1957.

[27] F. Porcelli, D. Boucher, M.N. Rosenbluth, "Model for the sawtooth period and amplitude", *Plasma Phys. Controlled Fusion*, vol. 38, 1996, 2163.

[28] M. Lennholm, L.-G. Eriksson, F. Turco, F. Bouquey, C. Darbos, R. Dumont, G. Giruzzi, M. Jung, R. Lambert, R. Magne, D. Molina, P. Moreau, F. Rimini, J.-L. Segui, S. Song, E. Traisnel, "Demonstration of effective control of fast-ion-stabilized Sawteeth by electron-cyclotron current drive", *Phys. Rev. Lett.*, vol. 102, 2009, 115004.

[29] J.P. Graves, I. Chapman, S. Coda, L.-G. Eriksson, and T. Johnson, "Sawtooth-Control Mechanism using Toroidally Propagating Ion-Cyclotron-Resonance Waves in Tokamaks", *Phys. Rev. Lett.* vol. 102, 2009, 065005.

[30] R. Goebel, R.G. Sanfelice, A.R. Teel, "Hybrid Dynamical Systems", *Princeton University Press*, 2012.

[31] M. van Berkel, G. Witvoet, M.R. de Baar, P.W.J.M. Nuij, H.G. Ter Morsche, M. Steinbuch, "Real-time wavelet detection of crashes in limit cycles of non-stationary fusion plasmas", *Fusion Eng. Des.*, vol. 86, 2001, pp. 2908 - 2919

[32] M.R. Liberzon, "Essays on the absolute stability theory", *Autom. Remote Control*, vol. 67, 2006, pp. 1610-1644.

Chapter 7

Conclusions, discussions, and outlook

7.1 Conclusions

This thesis is concerned with modelling, analysis, and control of three different strongly nonlinear processes in fluid dynamics and plasma physics. More concretely, these problems are:

1. Stabilization of vortex patterns in shallow-water-layers,
2. The influence of the time-variance on the efficiency of mixing in a time-periodic flow,
3. Control of the sawtooth period in a tokamak plasma.

In the introduction, several nonlinear dynamical phenomena have been presented that show that periodic inputs can be used to significantly change the qualitative behavior of nonlinear systems and the question was posed whether these phenomena are relevant and useful to three plasma and fluid problems.

The first phenomenon is the practical stabilization of an unstable equilibrium by periodic forcing. In Chapter 2 it has been shown experimentally that a certain unstable equilibrium of the two-dimensional Navier-Stokes equations can be practically stabilized by a periodic forcing. This can only occur because the (nonlinear) advection term is not negligible, which complies with other examples of vibrational control in which it turns out that the presence of a nonlinearity is essential. This experiment is consistent with existing theory about Taylor-Green vortex patterns. However, there is not yet a complete understanding of the stabilization due to the time-periodic forcing. Moreover, there is also a lack of understanding

for the experiments we conducted with a specific *aperiodic* (chirp) forcing showing self-organization and temporal stabilization of a vortex pattern that is not a Taylor-Green vortex pattern.

The second phenomenon is the occurrence of chaotic particle trajectories in two-dimensional time-periodic flows. This leads to improved mixing compared to time-invariant 2D flows, as the latter flows have only periodic trajectories. For a given time-periodic flow, the mixing process can be modeled by applying the mapping matrix formalism (normally used for simulations). In Chapter 3 it has been shown analytically that the block-diagonal structure of a given mapping matrix directly relates to the existence of transport barriers and to the size of the periodic islands. These periodic islands form an obstruction for efficient mixing. Previously, based on mapping matrix simulations, five conjectures had been posed. In this chapter these conjectures are demonstrated to be correct by applying tools from graph theory.

However, the mapping matrix formalism is not only suitable for modeling and analysing mixing in time-periodic flows but also for more general time-varying flows that are a concatenation of different flows. In Chapter 4 it has been shown that this type of flows can in general be modeled as a linear switching system. By taking this perspective, one can naturally solve the question how flows have to be concatenated to achieve fast mixing. By applying the rollout method one can always achieve a mixing rate that is analytically guaranteed to be at least as good as any chosen time-periodic strategy. Moreover, this method can also be applied for feedback control of mixing, leading to state-dependent instead of time-dependent switching. Both experiments and simulations confirm that the rollout method leads to faster mixing than a chosen (open-loop) time-periodic flow or the previously proposed minimum error algorithm.

The third nonlinear phenomenon discussed in the introduction is period locking, i.e. the adaptation of the period of a limit-cycle to the period of the modulated input. The sawtooth oscillation in fusion plasmas was previously always controlled by changing the location of the constant input power. In Chapter 5, it has been experimentally shown (in the TCV tokamak) that if the input location is kept fixed but the input power is periodically modulated, then this results in period locking that is rather robust. Not only is this (open-loop) locking approach easier to implement than the (feedback-based) change of input location approach and less sensitive to the input location, the sawtooth period also converges significantly

faster to the desired value using the locking approach compared to the current location approach. This result indicates that power modulation-based period control is a good alternative for the more conventional location-based control approaches.

Other recent experiments on the TCV tokamak (by Goodman et al. [1]) used the same philosophy of power-based control, only in these experiments the power level was feedback controlled (so-called pacing control). These experiments also showed that power-based period control seems to work better than location-based control. The use of feedback has the advantage that it is likely to be more robust for the time-varying plasma parameters but the disadvantage is that it is not always possible to obtain the necessary measurements for sawtooth feedback control, especially in future planned DEMO tokamaks. In Chapter 6 the pacing method has been analysed, for the first time, from a control theoretical perspective. Assuming a reduced model of the sawtooth oscillation, similar to an integrate-and-fire model, the analysis results in conditions that guarantee global exponential stability of a pacing controlled sawtooth oscillation. Moreover, the analysis shows that pacing control is guaranteed to realize stabilization for a rather general class of the input (power period) to output (sawtooth period) map. This explains why pacing control of the sawtooth period (and of the ELM oscillation) has been observed to be surprisingly successful and robust in experiments.

On a more abstract level, these results confirm the idea, proposed in the introduction, that the discussed nonlinear phenomena do appear in these considered problems in fluid dynamics and plasma physics. Moreover, it turns out that the presence of these phenomena can be exploited for open-loop control. In the cases of mixing and sawtooth period control, the understanding of the nonlinear dynamics even lead in a natural and analytical way to new feedback control approaches and these have been experimentally shown to be effective.

7.2 Discussions and outlook

Although a complete analytical explanation of the stabilization of the Taylor-vortex pattern could not be given in Chapter 2, the successful stabilization of one of these patterns by a periodic forcing has implications for the perspective on quasi-two-dimensional flows studies. Together with the experiments with an aperiodic chirp forcing, it is the first example in this field showing how a time-varying input can drastically change a vortex pattern. The experiments also demonstrate that feedback control of vortex patterns should be possible, as it can already be achieved

in an open-loop fashion. However, typical experiments with quasi-two-dimensional flows and most theory of Navier-Stokes equations typically study only the influence of stationary forcing. The experiments show that time-varying forcing might lead to different patterns and self-organization. This is also expected to appear in different settings, e.g. in experiments where the form of the forcing is different than adopted here (but still rather structured). Moreover, they confirm that the pattern formation theory based on the enstrophy-energy ratio arguments gives correct predictions with regard to the equilibria. This theory is more general - similar arguments exist for waves and plasma/MHD self-organization [2], notably Taylor relaxation in fusion reactors - and therefore the experiments suggest that also for these wave and plasma systems the influence of a time-varying input on self-organization should be studied within this theoretical perspective (i.e. as an open system instead of a closed system and studying the influence of time-varying forcing on the relevant energy-like functions and thereby on self-organization).

We emphasize that the failure to completely explain the experimental stabilization by periodic forcing is due to several fundamental reasons. First of all, study of the stability of time-periodic solutions of Navier-Stokes is even harder than the stability study of the stationary case, which is already nontrivial, especially when caused by a periodic input signal (as the non-autonomous time-periodic solution is not a limit-cycle). Secondly, note also that there is no analytical solution around for which a stability analysis could be done for the observed time-periodic flow. It is expected that these obstacles will appear generally in possible future studies and therefore stability might not be a suitable concept for studying this kind of problems and other concepts from system theory, e.g. passivity, are probably needed.

The study of mixing in Chapter 3 leads to the insight that the mapping matrix, normally used for simulations, can also be exploited for systematic analysis and, in fact, a straightforward inspection of the zero-nonzero structure of this matrix directly leads to insights on the existence of transport barriers in the underlying flow. However, how the form of a certain (time-periodic) flow determines the zero-nonzero structure of the mapping matrix is still an open question. Any significant progress on answering this question would be relevant for understanding the influence of the flow geometry on mixing but it is not evident how to tackle this problem. It has been noted that the mapping matrix shares certain characteristics with the Koopman operator approach to mixing and nonlinear dynamics [3] and

a better understanding of this relation might lead to new insights on the mapping approach.

In Chapter 4 the focus was on design of efficient mixing protocols instead of mixing analysis. Although the analytical results on mixing control in Chapter 4 are consistent with simulations and experiments, only a limited number of experiments were performed and more experiments are needed to validate whether the approach indeed always results in improved mixing performance. Especially the measurement of the concentration with a digital camera needs to be improved to make the results definite. Nevertheless, even with poor concentration measurements, the post experimental simulations (needed for a better estimation of the concentration distribution) affirmed that the rollout controlled flow mixed significantly better than the baseline periodic flow, demonstrating the potential of the approach. It appears that in the used experimental setup (journal bearing flow) periodic flows can already achieve fair mixing performance and therefore it would be useful to find an industrially relevant mixing problem in which the proposed control methodology makes a more significant difference, e.g. in a micro-mixer with a limited number of possible flows and with bad mixing performance.

Besides these practical issues, the mixing control perspective also leads to two open questions. Firstly, the question arises if the same approach is suited to create desired nonhomogeneous concentration distributions (instead of a homogeneous distribution) and for which combination of mapping matrices and initial conditions this is possible. To answer this question, we foresee that a reachability analysis of the relevant switching system has to be performed. Secondly, as it appears that the Koopman operator can be applied to more general dynamical systems besides mixing problems (note that also the mapping matrix approach is a method to discretize a second order nonlinear dynamical system), the question rises whether the suggested switching systems modeling and rollout control approach can be extended to other problems apart from chaotic advection. Note that the principles of the switching control approach essentially do not depend on the mapping matrix formalism. The switching control approach only requires the availability of a discrete-time dynamics in which each time step a mapping (from a limited number of mappings) needs to be chosen.

Another possible application of the mapping and switching approach, besides mixing, is envisioned in fusion. The magnetic field in a tokamak is divergence free and this leads to a Hamiltonian mapping from the poloidal magnetic field,

the map describing the change of the location of a magnetic field line starting in a poloidal plane for one toroidal rotation. An analytical example of such a mapping is the tokamap [4] and study of this map is relevant for understanding the topology of the magnetic field lines, for particle transport and for the sawtooth crash. Mathematically, this problem is almost identical to mixing in periodic flows, only here the periodicity is spatial (a period is one toroidal rotation) instead of time-periodic. Contrary to mixing, where one tries to maximize the amount of chaotic trajectories and minimize the periodic islands, in tokamaks magnetic field lines are desired to be non-chaotic because otherwise unwanted transport and MHD instabilities can be caused. Nevertheless, we suggest to investigate whether the same mapping and switching ideas can be applied for analysing and controlling the magnetic field line topology or transport in tokamaks.

Consistent with simulations, the experimental results in the TCV tokamak in Chapter 5 confirm that period locking of the sawtooth oscillation can appear in tokamak plasmas and that it can be used for sawtooth period control. The idea that the sawtooth period can be controlled by power modulation instead of changing the power deposition location is currently being validated by both simulations and experiments in other research groups. However, a rigorous analysis and design guidelines for sawtooth period locking are still lacking. To provide a rigorous analysis, it is important to validate and possibly improve the reduced model that is used in Chapter 6. If such an integrate-and-fire like model can be shown to be accurately describing the sawtooth period as a function of input power, then a rather standard period locking analysis can be performed. This should lead to design guidelines for the optimal shape, power amplitude, and duty cycle of the input. Moreover, one could also design feedback-based power modulation other than pacing that might be more efficient or more robust. A significant amount of articles on period locking and feedback period control of integrate-and-fire models already exists in neuroscience and this work can immediately be applied for sawtooth period control. As a side-note, we observed that the ELM oscillation is expected to behave according to a similar model and both the ELM period control and the interaction between sawtooth oscillation and ELM oscillation can be analyzed using the mentioned period locking tools.

The analysis of pacing, in Chapter 6, is entirely theoretical. To validate its relevance, it would be appropriate to experimentally or numerically verify whether the input-output map (of ECCD power period to sawtooth period) satisfies the conditions assumed in Chapter 6. If plasma conditions can be found for which

these conditions do not hold, then it is possible that pacing control fails, or, at least, needs further investigation. The same should be done for the input-output map in the case of the ELM period (given a certain actuation).

We end this chapter with some more general observations. All the work in this thesis is concerned with nonlinear distributed-parameter systems (either in fluids or plasmas) and all the discussed problems (vortex patterns, mixing, sawtooth oscillation) can be rather accurately modeled by partial differential equations (respectively by the 2D Navier-Stokes equations, the advection-diffusion equation, and a diffusion-reset model). Nevertheless, all the problems have been effectively modeled by finite dimensional (and often low-dimensional) models (the 2D flows in Chapter 2 can be described by a combination of a few Laplacian eigenmodes, the mapping matrix is a discretization of both time and space, and the sawtooth oscillation is assumed to be modeled by a first order reset model). Control theoretical analysis based on these reduced models results in performance guarantees for feedback control of mixing and of the sawtooth period. As both these controllers have been successfully tested in experiments, it appears that (for practical control purposes, and at least for these specific problems) it is more important for the control oriented model to describe the typical nonlinear behavior than to capture the infinite dimensional dynamics associated with partial differential equations. To finish, we observe further that, although none of the discussed problems is typically thought of as being discontinuous or non-differentiable, modeling techniques from linear hybrid systems (switching and reset models) have been - surprisingly - effective to model the relevant dynamics (relaxation oscillation and chaotic transport) of these nonlinear distributed-parameter systems. Although these observations are not expected to hold in general, if it is possible to model a complex nonlinear distributed-parameter systems in an efficient way (e.g. with a linear hybrid model) this can greatly reduce the complexity of control design.

Bibliography

[1] T.P. Goodman, F. Felici, O. Sauter, J.P. Graves, and the TCV Team, Sawtooth Pacing by Real-Time Auxiliary Power Control in a Tokamak Plasma, Physical Review Letters 106, 2011, 245002.

[2] A. Hasegawa, Self-organization processes in continuous media, Advances in Physics 34, 1985, pp. l-42.

[3] M. Budisic, R. Mohr, and I. Mezić, Applied Koopmanism, Chaos 22, 2012, 047510.

[4] R. Balescu, M. Vlad, F. Spineanu, Tokamap: A Hamiltonian twist map for magnetic field lines in a toroidal geometry, Physical Review E 58, 1998, pp. 951-964.

Summary

Control of Mixing and Oscillations in Plasmas and Fluids.

Many problems in fluids and plasmas are described by systems of highly nonlinear vector-valued partial differential equations and are therefore hard to analyse. In the last two decades, a lot of work has been done on controlling certain phenomena in fluids and plasmas. Most of this work deals with feedback control (i.e. it depends on real-time measurements) and is often theoretical.

In this thesis we show three different cases in which we are experimentally able to control relevant fluid and thermonuclear plasma problems. Vortex pattern stabilization, improved mixing, and period control have been achieved. The nonlinear nature of these problems makes them hard to analyse, but it is essentially due to this nonlinear nature of the problems that control without real-time measurements is possible (open-loop control). In the case of mixing and period control, the approach suggested by open-loop control has been used to design and analyse new feedback control laws (closed-loop) that perform better and are more robust for model uncertainties and disturbances.

Experiments of electromagnetically forced flows in shallow-water-layers, at a moderate Reynolds number, show that a time-dependent forcing results in stable or self-organizing vortex patterns that do not occur for stationary forcing. A theoretical analysis shows that the observed patterns are unstable equilibria of the autonomous Navier-Stokes partial differential equations and, based on variational arguments, are less likely to be stabilized by a forcing than the patterns that appear when the flow if stationary forced. A complete understanding of the stabilization mechanism is still missing, but it is clear that the nonlinear advection term in the Navier-Stokes equations is necessary for creating this stable pattern.

In similar flows as mentioned above, but at a lower Reynolds number (Stokes flows), efficient transport and mixing of particles (or scalar fields like temperature) is difficult to achieve. However, due to the nonlinear nature of the velocity vector field chaotic particles trajectories can be created and thereby efficient mixing can be achieved. The mixing process can be modelled using mapping matrices. In this thesis several open conjectures about the mapping matrices are answered. Furthermore, it is shown that this class of (nonlinear) mixing problems can in general be modelled as (linear) switched systems. In this framework, an optimization method (roll-out) is proposed to create efficient mixing sequences. This method can also be used for feedback control of mixing. Simulations and experiments show the efficiency of this approach and the viability of feedback controlled mixing.

In plasmas in nuclear fusion experiments (like tokamaks) several nonlinear oscillations (like the sawtooth oscillation) occur that significantly influence the total plasma. Our experiments in the TCV tokamak show that the sawtooth period can be efficiently controlled in open-loop fashion by stimulating the plasma with a periodic power pulse. The sawtooth period becomes similar to the pulse period for a significant range of the pulse period. This so-called period locking phenomenon is modelled and analysed theoretically.

Summarizing, in this thesis three different nonlinear (magneto)hydrodynamic problems have been experimentally controlled (often without feedback) using common nonlinear phenomena like vibrational stabilization, chaos and period locking. Although the mathematical models of these problems are complex, theoretical analysis can still lead to results that are consistent with experiments.

Samenvatting

Control of Mixing and Oscillations in Plasmas and Fluids.

Veel problemen in vloeistoffen en plasmas worden beschreven door systemen van sterk niet-lineaire partiële differentiaal vergelijkingen en zijn daarom moeilijk te analyseren. In de laatste twee decenia is er veel onderzoek gedaan naar het regelen van bepaalde fenomenen in vloeistof stromingen en plasmas. Het meeste van dit werk is theoretisch en gebaseerd op feedback control (d.w.z. het hangt af van real-time metingen).

In deze thesis tonen we experimenten in welke we drie verschillende vloeistof en plasma fenomenen regelen. Meer concreet: in de experimenten stabilizeren we wervelingen, verbeteren we menging en regelen we periodes. De niet-lineaire aard van deze problemen maakt ze moeilijk te analyseren, maar het is juist vanwege deze niet-lineaire aard dat we deze drie problemen in eerste instantie kunnen regelen zonder real-time metingen te gebruiken (zogenaamd open-loop control). In het geval van mengen en periode regelen kunnen we de aanpak voor open-loop control gebruiken om feedback regelwetten (closed-loop) te ontwerpen en analyseren. Deze regelwetten leiden tot betere prestaties en zijn robuuster voor model onzekerheden en verstoringen.

Experimenten met electromagnetisch geforceerde stromingen in ondiepe water lagen (bij een gematigd Reynolds nummer) laten zien dat tijdsafhankelijke stromingen resulteren in stabiele of zelf-organizerende wervel patronen die niet ontstaan in stationair gedreven stromingen. Een theoretische analyse toont dat de waargenomen patronen onstabiele evenwichten van de autonome Navier-Stokes partiële differentiaal vergelijkingen zijn en deze patronen zijn moelijker te stabilizeren dan patronen die waargenomen worden in stromingen met een stationaire

forcering. Een compleet begrip van dit stabilizatie mechanisme ontbreekt nog, maar het is duidelijk dat de niet-lineaire advectie term in de Navier-Stokes vergelijkingen noodzakelijk is voor het stabilizeren van dit patroon.

In soortgelijke stromingen als hierboven beschreven, maar bij een lager Reynolds number (zogenaamde Stokes stromingen), is het lastig om effectief transport en menging van deeltjes (of scalaire velden zoals temperatuur) te bereiken. Toch kunnen de deeltjes zich juist door de niet-lineaire aard van de snelheidsvelden chaotisch gaan gedragen en hierdoor kan effectieve menging bereikt worden. Het meng proces kan gemodelleerd worden met behulp van mapping matrices. In deze thesis beantwoorden we positief verschillende theoretische vermoedens uit de bestaande literatuur. Daarnaast laten we zien dat dit soort niet-lineaire meng problemen in het algemeen gemodelleerd kunnen worden als (lineaire) schakelende systemen ('switched systems'). In dit theoretische raamwerk stellen we een optimalizatie methode (roll-out) voor om effectieve meng acties te ontwerpen. Deze methode kan ook gebruikt worden als feedback control wet voor menging. Numerieke simulaties en experimenten tonen dat deze aanpak effectief is en dat feedback control van menging leidt tot betere menging.

In plasmas in kern fusie experimenten (in zogenaamde tokamaks) treden een aantal oscillaties op (zoals de zaagtand oscillatie) die het hele plasma significant beïnvloeden. Onze experimten op de TCV tokamak tonen dat de zaagtand periode effectief in open-loop geregeld kan worden door het plasma met een periodieke vermogenspuls te stimuleren. Voor een redelijk groot bereik van de puls periode past de zaagtand periode zich aan de vermogenspuls periode aan. Dit zogenaamde 'period locking' fenomeen is theoretisch gemodelleerd en geanalyseerd.

Samenvattend, in deze thesis zijn drie verschillende niet-lineaire (magneto) hydrodynamische problemen experimenteel geregeld. Juist door gebruik te maken van niet-lineaire fenomenen zoals 'vibrational stabilization', chaos en 'period locking' kan dit in principe zonder gebruik te maken van feedback control. Ondanks de wiskundige complexiteit van de modellen zijn er toch theoretische resultaten bereikt die consistent zijn met de experimenten.

Acknowledgements

Aangezien het dankwoord het meest gelezen onderdeel van een thesis schijnt te zijn, had ik graag met een epische openingszin willen beginnen. Desondanks wil ik hier toch even stil staan bij de mensen die me de afgelopen vier jaar en daarvoor hebben bijgestaan bij het maken van het werk wat hier nu ligt. Ten eerste wil ik Marco de Baar bedanken voor de kans om aan interessante problemen te werken. Altijd enthousiast en postief stimuleerde je ook werk wat buiten je eigen expertise lag zolang het maar relevant en interessant was. Ook heb je het voor elkaar gekregen dat ik de bijbehorende artikelen afgeschreven heb. Dat is op zichzelf al geen kleine prestatie. Ook Maurice Heemels wil ik erg bedanken voor de prettige samenwerking. In het bijzonder voor het snel oppikken van de ideëen over hybride systemen in de natuurkunde en voor de gedetailleerde kritiek waarmee je de wiskundige kant van de thesis ongetwijfeld een stuk verbeterd hebt.

I would like to thank all the members of the committee (Emmanuel Witrant, GertJan van Heijst, Henk Nijmeijer, Igor Mezić, Rony Keppens and Tony Donné) for taking the time to critically read the thesis and for interesting suggestions and questions. Henk and GertJan are without a doubt responsible for my ongoing interest in nonlinear fluid dynamics in the broadest sense. Thanks to all my co-authors (Vandersteen, Witvoet, Hennen, Felici, Sauter, Goodman, Kamp, Speetjens, Anderson, Nijmeijer, de Baar, Hommen, Borgers, Heemels, Antunes, Dolk, Lennholm, Westerhof, Steinbuch, Belykh, Hasler, and the TCV team) for the pleasant collaboration and Leon for saving that never-ending paper. For help and important discussions related to some of the chapters I thank Juan Pérez Munoz, Hans Zwart, Benjamin Biemond, Kolumbán Sándor, Brock Mosovsky, and Chris Criens. Tore Supra at CEA, TCV/CRPP at EPFL, and the ELEC group at the Vrije Universiteit Brussel I thank for their support and hospitality. Also

several workshops at the Lorentz center in Leiden were pivotal for some of the work in this thesis. I have been extremely lucky with my three Master students Victor Dolk, Niek Borgers, and Bart Ripperda, as all three came up with very good results. Victor's work has been essential in the experimental realization of the mixing control ideas in chapter 4. I also like to thank my Batchelor students Daniel, Eric, Jelmer, Taco, Marc, and Seva for their nice work.

One of the most fulfilling parts of doing PhD research is having serious scientific discussions. For that I thank apart from several of my co-authors also Hans Zwart, Benjamin Biemond, Erik Steur, Federico Felici (for explaining flux diffusion after 3 years of doubt), Morten Lennholm, Gerardo Giruzzi, Mark Peletier, Hans Goedbloed, Jan-Willem Blokland, Ziv Kizner and my fellow (con)fusion researchers Bart, Pieter, Gert, Gillis, Hugo, Bert, Federico, Wolf Weymiens, and Jonathan Citrin. The amazing cover (though I say it myself) is due to the creative genius of Nick Bauer.

Besides the scientific work I had a really good time doing my PhD thanks to many people, but I explicitly want to mention my great office mates: Behnam, Nick, Chris, Emanuel, Bart, and Xi. For the amazing good times and cool trips I thank the hairy biker gang: Sinan Öncü [ons'joe], Tom Gommans, and, 'Slick' Nick Bauer and of course also the one-and-only Matthijs (for his surprise visits), Bas, Duarte, Robbert 'smoesjes' and everybody else that I forget. For the many stress relieving squash games I thank Michael Boot and Alejandro 'el Maestro' Rodriguez Angeles for the free master classes. To my squash nemesis César Lopez I only repeat Gargamel's words "I'll get you, if that's the last thing I ever do!". Natuurlijk wil ik mijn familie Paula, Wilfried, Caroline, Christophe en Marie Inghels heel erg bedanken voor alle steun en liefde over de jaren heen. Ook de wijdere familie wil ik daarvoor bedanken, in het bijzonder Rosita, Dorthy en Marga voor hun gastvrijheid om bij hen te schrijven. Arnold zal zijn dappere pogingen om een echte werktuigbouwer van me te maken wel definitief opgeven na het lezen van dit boek. Ellen Goudsmits, dank je voor je onvoorwaardelijke liefde en onstuitbare energie waarmee je me gestimuleerd hebt om dit werk snel af te krijgen. Voor de menselijke kant van het leven zijn Toon en Jo Schout altijd grote voorbeelden voor me geweest en daarom wil ik deze thesis aan hen opdragen.

Curriculum Vitae

Menno Lauret was born on January 12th, 1979 in Hulst, The Netherlands. He finished his VWO education at the Reynaert College (formerly Jansenius Lyceum) in Hulst in 1998 and started his Mechanical Engineering education at the Eindhoven University of Technology. He received his Master's degree in 2010. During his Master's education he did a traineeship at EPFL (Lausanne) on synchronization of chaotic oscillators coupled in arbitrary networks. His Master's project dealt with stabilization of vortex patterns in flows in the Dynamics and Control group, in cooperation with the Fluid Dynamics Laboratory at the Physics department of the Eindhoven University of Technology.

In August 2010, his PhD research started at FOM-DIFFER within the FOM-120 program and in cooperation with the Control Systems Technology group of the Eindhoven University of Technology. The subject of his research was sawtooth period control in Tokamaks but also work on NTM control, hydrodynamics and controlled mixing has been performed. Parts of the work were done in collaboration with the Tore Supra Tokamak (Cadarache), TCV Tokamak (CRPP at EPFL in Lausanne), and the Vrije Universiteit Brussel. The main results are published in this thesis.